

270  
6-978

14. 151

DOE/JPL/954373-4

## HEAT EXCHANGER-INGOT CASTING/SLICING PROCESS

Silicon Sheet Growth Development for the Large Area Silicon Sheet Task of  
the Low Cost Silicon Solar Array Project

Final Report—Phase I, November 20, 1975—November 20, 1977

By  
Frederick Schmid  
Chandra P. Khattak

December 1, 1977

Work Performed Under Contract No. NAS-7-100-954373

Crystal Systems, Incorporated  
Salem, Massachusetts

MASTER

U.S. Department of Energy



Solar Energy

DISTRIBUTION OF THIS DOCUMENT IS UNLIMITED

## **DISCLAIMER**

**This report was prepared as an account of work sponsored by an agency of the United States Government. Neither the United States Government nor any agency Thereof, nor any of their employees, makes any warranty, express or implied, or assumes any legal liability or responsibility for the accuracy, completeness, or usefulness of any information, apparatus, product, or process disclosed, or represents that its use would not infringe privately owned rights. Reference herein to any specific commercial product, process, or service by trade name, trademark, manufacturer, or otherwise does not necessarily constitute or imply its endorsement, recommendation, or favoring by the United States Government or any agency thereof. The views and opinions of authors expressed herein do not necessarily state or reflect those of the United States Government or any agency thereof.**

## **DISCLAIMER**

**Portions of this document may be illegible in electronic image products. Images are produced from the best available original document.**

## NOTICE

This report was prepared as an account of work sponsored by the United States Government. Neither the United States nor the United States Department of Energy, nor any of their employees, nor any of their contractors, subcontractors, or their employees, makes any warranty, express or implied, or assumes any legal liability or responsibility for the accuracy, completeness or usefulness of any information, apparatus, product or process disclosed, or represents that its use would not infringe privately owned rights.

This report has been reproduced directly from the best available copy.

Available from the National Technical Information Service, U. S. Department of Commerce, Springfield, Virginia 22161.

Price: Paper Copy \$9.25  
Microfiche \$3.00

**NOTICE****PORTIONS OF THIS REPORT ARE ILLEGIBLE. IT**

has been reproduced from the best available  
copy to permit the broadest possible avail-  
ability.

**HEAT EXCHANGER-INGOT CASTING/SLICING PROCESS****Silicon Sheet Growth Development for the  
Large Area Silicon Sheet Task of the Low Cost  
Silicon Solar Array Project****NOTICE**

This report was prepared as an account of work sponsored by the United States Government. Neither the United States nor the United States Department of Energy, nor any of their employees, nor any of their contractors, subcontractors, or their employees, makes any warranty, express or implied, or assumes any legal liability or responsibility for the accuracy, completeness or usefulness of any information, apparatus, product or process disclosed, or represents that its use would not infringe privately owned rights.

Final Report  
by  
Frederick Schmid and Chandra P. Khattak

Covering Period from November 20, 1975 to November 20, 1977  
Date of Report: December 1, 1977

JPL Contract No. 954373

CRYSTAL SYSTEMS, INC.  
35 Congress Street  
P. O. Box 1057  
Salem, MA 01970

This work was performed for the Jet Propulsion Laboratory, California Institute of Technology, under NASA Contract NAS7-100 for the U. S. Energy Research and Development Administration, Division of Solar Energy.

The JPL Low-Cost Silicon Solar Array Project is funded by ERDA and forms part of the ERDA Photovoltaic Conversion Program to initiate a major effort toward the development of low-cost solar arrays.

## TABLE OF CONTENTS

LIST OF TABLES . . . . .	vi
LIST OF FIGURES . . . . .	vii
SUMMARY . . . . .	xii
1. CRYSTAL CASTING . . . . .	1
1.1 ABSTRACT . . . . .	1
1.2 CRYSTAL GROWTH. . . . .	3
1.2.1 Heat Exchanger Method (HEM) . . . . .	3
1.2.2 Experimental Crystal Growth. . . . .	5
1.2.3 Improvement of Heat Extraction . . . . .	11
1.3 MATERIAL CHARACTERIZATION . . . . .	15
1.3.1 Crystal Structure . . . . .	15
1.3.2 Dislocation Density Measurements . . . . .	17
1.3.3 Lifetime Measurements . . . . .	19
1.3.4 Solar-Cell Performance . . . . .	20
1.4 CRUCIBLE DEVELOPMENT. . . . .	24
1.4.1 Clear Silica Crucibles . . . . .	27
1.4.2 Coated Crucibles . . . . .	30
1.4.3 Hot Pressed Crucible . . . . .	30
1.4.4 Pressure Cast Crucibles. . . . .	32
1.4.5 Slip Cast Crucibles . . . . .	35
1.4.6 Graded Crucibles . . . . .	35

1.5 HEAT FLOW . . . . .	41
1.5.1 Theoretical Model . . . . .	41
1.5.2 Theoretical Growth Rate . . . . .	44
1.6 SOURCE OF FORMATION OF SILICON CARBIDE - EXPERIMENTAL . . . . .	51
2. SILICON CRYSTAL SLICING. . . . .	53
2.1 ABSTRACT. . . . .	53
2.2 INTRODUCTION. . . . .	56
2.3 MACHINE DEVELOPMENT . . . . .	58
2.4 BLADE DEVELOPMENT . . . . .	60
2.4.1 Introduction . . . . .	60
2.4.2 Mechanical Properties of Core Wire . .	61
2.4.3 Impregnated Wire . . . . .	66
2.4.4 Electroplated Wire . . . . .	73
2.5 SLICING TEST. . . . .	78
2.5.1 Introduction . . . . .	78
2.5.2 Slicing with Impregnated Blades. . . .	78
2.5.3 Effect of Workpiece Motion . . . . .	82
2.5.4 Slicing with Diamond Plated Wire	83
2.5.5 Slicing a 7.6 cm Diameter Workpiece. .	91
2.6 WAFER CHARACTERIZATION. . . . .	93
2.6.1 Evaluation of Work Damage in Silicon Wafers . . . . .	93
2.6.2 Examination of Silicon Swarf . . . . .	99

3. ECONOMIC ANALYSIS . . . . .	101
3.1 INGOT CASTING . . . . .	102
3.2 INGOT SECTIONING. . . . .	107
3.3 INGOT SLICING . . . . .	108
3.3.1 Cost of Expendable Material. . . . .	108
3.3.2 Cost Analysis for Slicing. . . . .	109
4. CONCLUSIONS . . . . .	112
5. REFERENCES . . . . .	114
APPENDIX A: Tabulation of Heat-Exchanger and Furnace Temperatures . . . . .	118
APPENDIX B: SOURCE OF FORMATION OF SILICON CARBIDE - THEORETICAL . . . . .	137
B.1 SOURCE OF FORMATION OF SILICON CARBIDE - THEORETICAL . . . . .	137
B.1.1 Introduction . . . . .	137
B.1.2 Sources of Thermochemical Data Employed in the Analysis. . . . .	137
B.1.3 Consideration of the Reaction between Liquid Silicon and Silica Crucible I . .	139
B.1.4 Consideration of the Reaction between Liquid Silicon and Silica Crucible II. .	139
B.1.5 Examination of the CO/CO <sub>2</sub> Equilibrium in the Working Range . . . . .	141
B.1.6 Evaluation of the Reaction between Oxygen Dissolved in Silicon with Silicon to Form Gaseous SiO . . . . .	143
B.1.7 Consideration of the Simultaneous Reaction of Carbon and Oxygen in Liquid Silicon. . . . .	145
B.1.8 Detailed Calculation of the Rate of Evaporation of Silicon Monoxide. . . .	146

B.1.9	Comparison of the Calculated Rate with the Rate Observed During a Crystal Growth Experiment . . . . .	147
B.1.10	Consideration of Reactions between Graphite and Silica Crucible. . . . .	148
B.1.11	Consideration of Reaction between CO and C with SiO . . . . .	152
B.1.12	Consideration of Reaction between CO or CO <sub>2</sub> with Silicon . . . . .	154
B.2	Efforts to Eliminate Silicon Carbide Impurities . . . . .	159
B.3	Conclusions . . . . .	168
APPENDIX C:	The Effects of Wire Tension and Modulus of Elasticity on Deflection. . . . .	169
APPENDIX D:	Mechanical Property Test Data for Tungsten, Stainless Steel, and Steel Wire . . . . .	172
APPENDIX E:	Silicon Slicing Summary . . . . .	176

## LIST OF TABLES

TABLE I	Dislocation Density Data on HEM Grown Boules . . . . .	19
TABLE II	Minority Carrier Lifetime Measurement Data . . . . .	20
TABLE III	I-V Parameters (AMO) for Solar Cells Made from HEM Grown Silicon (DVM Readings), . . . . .	23
TABLE IV	EDAX Counts in Three Areas of Figure 15. .	24
TABLE V	Identification of Symbols. . . . .	50
TABLE VI	Hardness of Various Components of Wires Measured on a Leitz Microhardness Tester with a Knoop Diamond Point and Using a 50 gram Load . . . . .	65
TABLE VII	Details of Plating of Impregnated Wire . .	73
TABLE B	Summary of Thermochemical Data . . . . .	138

## LIST OF FIGURES

Figure Number	Figure Title	Page
1	Schematic of Crystal Casting Furnace . . . . .	4
2	Photomicrograph at 125X Showing the Seed on Bottom and Two Interfaces for Run 16 . . . . .	7
3	Polished and Etched Cross-section of Boule 47-C	9
4	Polished and Etched Cross-section of Boule 72-C	10
5	Polished and Etched Cross-section of Boule 83-C	10
6	Polished and Etched Cross-section of Boule 95-C	12
7	Polished and Etched Section of Boule 109-C Showing Melt-back and Growth on the Sides of Seed . . . . .	12
8	Polished and Etched Cross-section of Boule 110-C. Efficient Heat Transfer through Graphite Plug Prevented Seed Melt-back . . . . .	14
9	Polished and Etched Cross-section of Boule 75-C	14
10	Polished and Etched Section of Boule 95-C . . .	16
11	Orientation of Grains Perpendicular to the Cut Surface as Indicated by Spots on Figure 10, Plotted on a Stereographic Triangle . . . . .	16
12	Polished and Etched Cross-section of Boule 103-C	18
13	Typical $V_{oc}$ Decay Curves for HEM and Control Samples . . . . .	21
14	SEM Examination of Silica/Silicon Interface . .	25
15	A Higher Magnification of Figure 14 Showing Areas where EDAX Counts Were Taken . . . . .	25

Figure Number	Figure Title	Page
16	Polished and Etched Cross-section of Boule 74-C Showing Lateral Growth . . . . .	26
17	"As Removed" Fractured Section of Silicon Cast in a Clear Silica Crucible. . . . .	26
18	Crack-free Silicon Boule Obtained in Run 93-C . .	29
19	Crack-free Silicon Cast in a Coated Crucible. . .	29
20	A Section of the Crack-free Silicon Cast in a Hot-pressed Crucible. . . . .	31
21	Optical Micrograph (100X) under Polarized Light for Hot-pressed Crucible. . . . .	31
22	Crack-free Silicon Cast in Pressure Cast Crucible (Run 90-C) . . . . .	33
23	Optical Micrograph (100X) Showing the Silicon/Silica Interface for 8 $\mu\text{m}$ (above) and 25 $\mu\text{m}$ (below) . . . . .	34
24	Crack-free Silicon Cast in High Purity (above) and Technical Grade (below) Slip Cast Crucibles .	36
25	Crack-free Silicon Cast in a Glazed Crucible. . .	37
26	Crack-free 3.3 Kg Silicon Boule Cast in Run 109-C	37
27	Optical Micrograph (250X) of a Section of Graded, Opaque Silica Crucible before Casting Silicon .	39
28	Optical Micrograph (250X) of a Top Section of Graded, Opaque Silica Crucible after Casting Silicon . . . . .	39
29	Crack-free Silicon Boule Cast in Run 103-C Using a Graded, Translucent Silica Crucible . . . . .	40
30	Optical Micrograph (750X) of the Silicon/Graded Translucent Crucible Interface. . . . .	40

Figure Number	Figure Title	Page
31	Nodal Arrangement in the Melt for the Finite Difference Model of Heat Flow . . . . .	43
32	Steady State Solution Showing the Various Isotherms for Different Regions in the Melt. . . . .	43
33	Effect of Rate of Decrease of Heat Exchanger Temperature on Solidification Time. . . . .	45
34	Shape of Solidification Front as a Function of Time. . . . .	45
35	Effect of Size of Heat Exchanger on Growth Time	46
36	Helium Flow Rate - Liters/Minute. . . . .	47
37	Engineering Stress Strain Curve for Plain Tungsten Wire . . . . .	64
38	SEM of 8 mil Copper Sheathed Stainless Steel Wire Impregnated with 45 $\mu\text{m}$ Diamond . . . . .	68
39	SEM of 8 mil, Copper Sheathed Stainless Steel Wire Double Impregnated with 45 $\mu\text{m}$ Diamonds . .	69
40	SEM of Diamond Impregnated Wire Used in Run 42-S Showing Diamond Pull-out . . . . .	70
41	SEM of 8 mil Copper Sheathed Stainless Steel Wire Impregnated with 45 $\mu\text{m}$ Diamonds and Electroless Plated with 0.3 mil nickel. . . . .	72
42	SEM of Tungsten Wire 5 mil (0.127 mm) Nickel Plated with 400 Mesh 37 $\mu\text{m}$ Diamonds (Unused) . .	74
43	SEM of Tungsten Wire 5 mil (0.127 mm) Nickel Plated with 400-mesh 37 $\mu\text{m}$ Diamonds Used in Runs 18, 19, 20 . . . . .	76
44	Feed Force vs. Cutting Rate (Surface Speed 140 ft/min) . . . . .	79
45	Cutting Rate vs. Depth of Cut . . . . .	81
46	Average Cutting Rates, Runs 18-36, Using Electroplated Wires . . . . .	85

Figure Number	Figure Title	Page
47	Cutting Rate vs. Distance Cut . . . . .	86
48	Profiliometer Tracing of 0.0055 Silicon Wafer 41-S.	90
49	SEM Photograph at 1500X Magnification of Two Wafers Showing Microfissures . . . . .	95
50	SEM Photograph at 5000X of the Edge of Wafer 58-S .	95
51	Photomicrograph at 1000X Magnification of Polished Tapered Section of Wafer (Run 59) Showing Surface Roughness . . . . .	96
52	Profiliometer Tracing of Wafer (Run 59-S) Sliced with 45 $\mu\text{m}$ Diamond and 32 gm Feed Force . . . . .	97
53	Photomicrograph at 1000X Magnification of Etched Tapered Section of Wafer (Run 59) Showing Dislocation Pile-up on Surface . . . . .	98
54	SEM of Silicon Swarf: . . . . .	100
55	Impact of Crucible Cost and Solidification Time on Add-on Cost/kg. . . . .	105
56	Effect of Ingot Size, Materials Cost and Growth Rate on Growth Costs. . . . .	106
B-1	Equilibrium Vapor Pressure of Gaseous $\text{SiO}$ as a Function of Temperature for the Reaction $\text{Si}$ (CONDENSED) + $\text{SiO}_2$ (CONDENSED) $\rightarrow$ 2 $\text{SiO}$ (gas) . . . . .	140
B-2	Total Equilibrium Vapor Pressure of $\text{SiO}$ and $\text{O}_2$ for the Reaction $\text{Si}$ (CONDENSED) + 3 $\text{SiO}_2$ (CONDENSED) $\rightarrow$ $\text{O}_2$ + 4 $\text{SiO}$ (GAS) . . . . .	142
B-3	Equilibrium Boundary for the Reaction $\text{O}$ (Dissolved Oxygen) + $\text{Si}$ (CONDENSED) $\rightarrow$ $\text{SiO}$ (GAS) as a Function of Oxygen Concentration (in Atomic Fraction and Atoms/cm <sup>3</sup> ) . . . . .	144

Figure Number	Figure Title	Page
B-4	Free Energy of Various Reactions as a Function of Temperature. . . . .	149
B-5	Calculated Pressure-Temperature Relations for Reaction of Graphite and Silica to Form Silicon Carbide, Silicon Monoxide and Carbon Monoxide . . .	151
B-6	Equilibrium Total Pressure of CO and SiO as a Function of Temperature for the Reaction $CO + 3SiO \rightarrow SiC + 2SiO_2$ . . . . .	153
B-7	Equilibrium Pressure of CO as a Function of Temperature for the Reaction $2CO + 3Si \rightarrow 2SiC + SiO_2$ . . . . .	157
B-8	Equilibrium Pressure of $CO_2$ as a Function of Temperature for Reaction I <sup>2</sup> - $SiC + SiO_2 \rightarrow 2Si + CO_2$	160
B-9	Equilibrium Pressure of CO as a Function of Temperature for Reaction II - $2SiC + SiO_2 \rightarrow 3Si + 2 CO$ . . . . .	161
B-10	Total Pressure of SiO and CO as a Function of Temperature for Reaction III - $SiC + SiO_2 \rightarrow SiO + CO + Si$ . . . . .	162
B-11	Total Pressure of SiO and CO as a Function of Temperature for Reaction IV - $SiC + 2SiO_2 \rightarrow 3SiO + CO$ . . . . .	163
B-12	Equilibrium Pressure of SiO as a Function of Temperature for Reaction V - $SiC + SiO_2 \rightarrow C + 2SiO$ .	164

## SUMMARY

The proof of concept for silicon casting by the Heat Exchanger Method has been established. One of the major hurdles of ingot cracking has been eliminated with the development of graded crucibles. Such crucibles are compatible with the casting process in that the integrity of the container is maintained at high temperature; however, during the cool-down cycle the crucible fails, thereby leaving a crack-free boule. Ingots as large as 3.3 kg have been cast using this approach.

The controlled growth, heat-flow and cool-down has yielded silicon with a high degree of single crystallinity. Even when the seed melted out, very large grains formed. Solar cell samples made from cast material have yielded conversion efficiency of over 9% (AM1). (Standard Czochralski material processed simultaneously yielded only 11% {AM0} efficiency cells.) Representative characterizations of silicon grown has demonstrated a dislocation density of less than  $100/\text{cm}^2$  and a minority carrier diffusion length of 31  $\mu\text{m}$ .

The source of silicon carbide in silicon ingots has been identified to be from graphite retainers in contact with silica crucibles. Higher growth rates have been achieved with the use of a graphite plug at the bottom of the silica crucible.

Excellent surface quality, i.e., surface smoothness and 3-5  $\mu\text{m}$  surface damage, was achieved by multiple wire slicing with fixed diamond abrasive. To achieve this, the silicon workpiece was non-synchronously rocked to produce a radial cut profile and minimize wire contact length. Wire wander was reduced an order of magnitude over the original results by supporting and guiding the wires with grooved rollers.

Commercially available impregnated wires that were used failed due to diamond pull-out. Plating after impregnation or electroplating diamonds directly on the core minimized diamond pull-out and corresponding loss in cutting effectiveness. Wires plated after impregnation hold the most promise, since the diamond size concentration and distribution can be best controlled.

Tungsten wire was the best core material tested because of its high strength, high Young's modulus, and resistance to hydrogen embrittlement. Diamond costs were reduced by impregnating diamonds only on the cutting areas of the wire.

A lighter and longer blade carriage can be used for slicing with wire. This will allow the blade carriage to be reciprocated more rapidly to increase the surface speed.

A projected add-on cost calculation shows that these methods will yield silicon for solar cell applications within ERDA/JPL cost goals.

## 1. CRYSTAL CASTING

### 1.1 ABSTRACT

A program on silicon crystal casting by the Heat Exchanger Method (HEM) has been underway since November 1975, under this contract. The object of the program has been to establish proof of concept of this method of silicon crystal growth compatible with ERDA/JPL goals for terrestrial photovoltaic applications.

Large ingots weighing up to 3.3 kg have been cast. Solar cells made from the HEM cast materials have shown conversion efficiencies greater than 9% (AM1). (Standard Czochralski material processed simultaneously yielded only 11% {AMO} efficiency cells.) A high degree of single crystallinity has been achieved, and even in areas where growth instabilities occurred, very large grains were formed. Such structures should be acceptable for processing into solar cells. The single crystal material grown has shown high quality with a dislocation density of less than 100 per  $\text{cm}^2$  and a minority carrier diffusion length of  $31 \mu\text{m}$ .<sup>1</sup>

The major problems associated with casting silicon in silica crucibles are crucible decomposition and cracking of the ingot. The former is because of reaction of silicon and silica<sup>2</sup> while the latter is due to mismatch of thermal expansion

coefficients.<sup>3,4</sup> Theoretically the crucible decomposition is compounded by operating in vacuum. However, experimentally it has been found that the erosion rate of the crucible is not enough to cause crucible decomposition. The cracking of the ingot has been resolved with the development of graded silica crucibles which relieve the stresses by sacrificially failing and thereby permitting casting of a sound silicon ingot.

Another serious problem associated with silicon growth is the formation of silicon carbide which lowers the solar cell conversion efficiency in the device.<sup>5</sup> Thermodynamic studies<sup>6</sup> have indicated that this is associated with the use of graphite retainers to hold the crucible.

In conclusion, a proof of concept of silicon growth by the HEM has been established and large crack-free ingots have been cast. This process shows a potential for use in making silicon for solar cell applications. A number of problems have been encountered, the solution to some has been attained, while the cause of others has been established. This information will be used in expanding the program for scale up to prototype production.

## 1.2 CRYSTAL GROWTH

### 1.2.1 Heat Exchanger Method (HEM)

The HEM, in principle, is a directional solidification process. A schematic of the furnace is shown in Figure 1. In this crystal growth method, the polycrystalline charge is placed on top of the seed which is centered on the bottom of the crucible. After evacuation to 0.1 Torr, heat is provided by the graphite resistance furnace. The seed is cooled and prevented from melting by forcing gaseous helium through the heat exchanger. The distinguishing feature of this method is the ability to independently control the solidification interface without moving the crucible, heat zone or crystal.

The crystal by this process grows from the bottom to the top; hence, convection currents and thereby associated concentration fluctuations at the solid-liquid interface are suppressed.<sup>8</sup> The solid-liquid interface is surrounded by the melt, thereby preventing the incorporation of impurities which are lighter than silicon, such as SiO and SiO<sub>2</sub>, which float to the surface of the melt. These factors contribute to the growth of crystals which have a high degree of perfection.<sup>9,10</sup> A major potential of the process lies in the fact that even inclusions at the solid-liquid interface appear not to cause any growth instabilities to occur.<sup>11</sup> This is contradistinct to Czochralski growth where such interface breakdown would result in twin/polycrystalline growth.

The vacuum operation eliminates the need to flow expensive

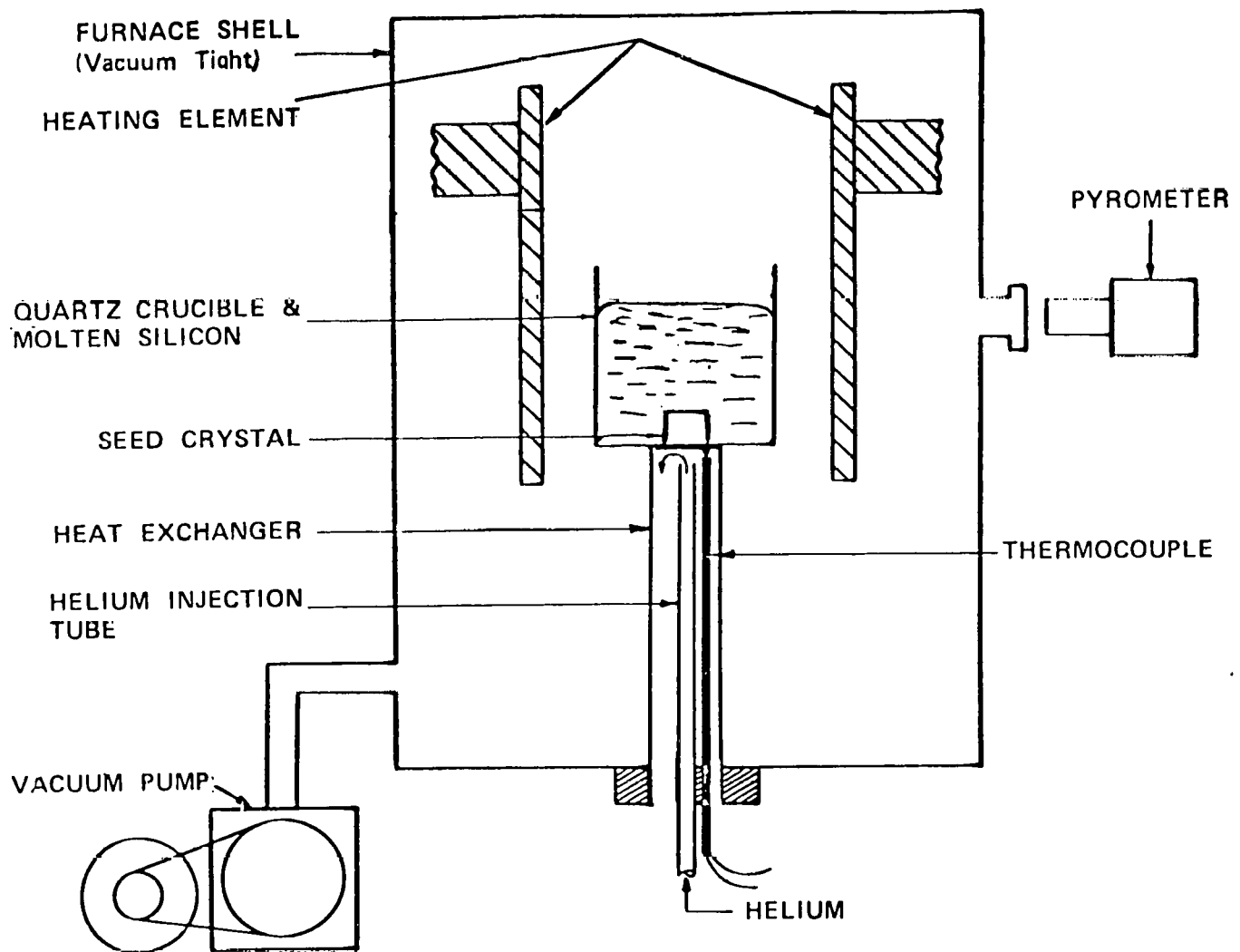


Figure 1. Schematic of Crystal Casting Furnace

high-purity Argon. Vibration effects such as standing waves are damped out beneath the surface making the HEM much less sensitive to vibration. The directional solidification could result in rejection of the impurities to the last material to freeze; hence, an overall purification of the cast crystal is possible. Since the crystal is still in the heat zone after solidification, in-situ annealing is carried out. Annealing reduces residual stresses and dislocation generation<sup>12</sup> and improves chemical uniformity throughout the crystal.

The process lends itself easily to scale up for the growth of large single crystals.<sup>13,14</sup> It has potential for economically growing silicon crystals to shape.

### 1.2.2 Experimental Crystal Growth

One of the experimental difficulties of the HEM is that the solid-liquid interface is submerged below the melt and cannot be observed during growth. Therefore, early experiments were carried out to characterize the seeding conditions necessary for the growth of single crystal silicon. The variables that influence seeding are the seed size, heat exchanger, and melt temperature, i.e., changes in liquid and solid gradients. To nucleate at the seed and maintain crystallinity during the growth cycle, the temperature gradients in the liquid and solid cannot be either too steep or too shallow.

Using the experience with sapphire growth by the HEM, the silicon melt was initially maintained at greater than  $10^{\circ}\text{C}$  superheat. The variables of the experiments are listed in Appendix A.

Examination of the initially solidified ingots revealed two distinct interfaces on the seed as illustrated in Figure 2. In this figure epitaxial growth appears to have initially grown followed by a polycrystalline growth due to interface breakdown. This instability was attributed to steep gradients in the liquid and/or solid. It appears, therefore, that the liquid and solid gradients are critical for silicon solidification.

In an effort to reduce the possibility of multi-nucleation and thereby polycrystalline growth, experiments were carried out to increase the superheat of the melt. It was found<sup>15</sup> that an increase of  $5^{\circ}\text{C}$  superheat--from  $10^{\circ}\text{C}$  to  $15^{\circ}\text{C}$  above melt point--required  $40^{\circ}\text{C}$  decrease in heat exchanger temperature to prevent seed melt-out. This shows that a temperature control of the furnace is more critical than that of the heat exchanger. Further, an increase of superheat in the melt causes steep liquid gradients as well as solid gradients.

In early experiments the heat exchanger was below the heat zone; hence, the temperature profile at the bottom of the **crucible** was not flat. To achieve consistency from run to run, the heat exchanger was raised in the furnace. This new configuration reduced the steep temperature gradients in the solid. After run 22 the furnace temperature was kept so that a superheat of less than  $10^{\circ}\text{C}$  was

## INTERFACES BETWEEN SEED AND INGOT

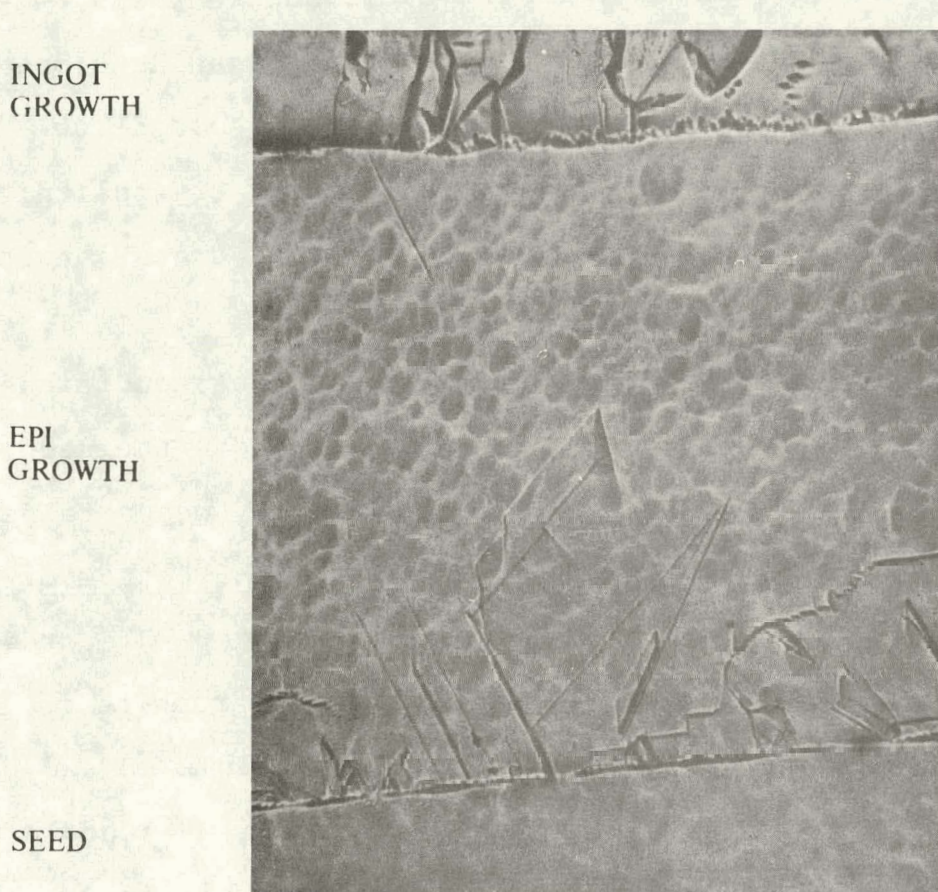


FIGURE 2. Photomicrograph at 125 X showing the seed on bottom and two interfaces for Run 16.

maintained, thereby reducing gradients in the liquid. Under these circumstances, good seeding and growth was achieved as evidenced by Figure 3 showing polished and etched cross-sections of run 47-C.

In an effort to achieve fast growth rates, experiments were carried out to study the growth periods as a function of the melt superheat. It was found that an extra degree of superheat could elongate the growth cycle substantially.<sup>16</sup> Therefore, the furnace temperature was maintained as close to the melt temperature as the instrumentation would allow--3°C. Even with such low superheats a high degree of crystallinity was achieved as seen by a polished and etched cross-section of run 72-C in Figure 4.

Having established the proper seeding conditions, growth of new material was generally achieved above the seed; however, in the lateral direction polycrystallinity was obtained.<sup>17</sup> It was felt that heat was radiating from the bottom of the melt directly to the coldspot--the heat exchanger. In order to reduce these radiation losses, insulation (graphite felt) was put around the exposed heat exchanger tube. This caused the extraction of heat from the sides to be via the seed to the heat exchanger resulting in lateral growth as well as at the top of the seed. Figure 5 shows a polished and etched section of the boule from run 83-C, where essentially all the material solidified as a single crystal.

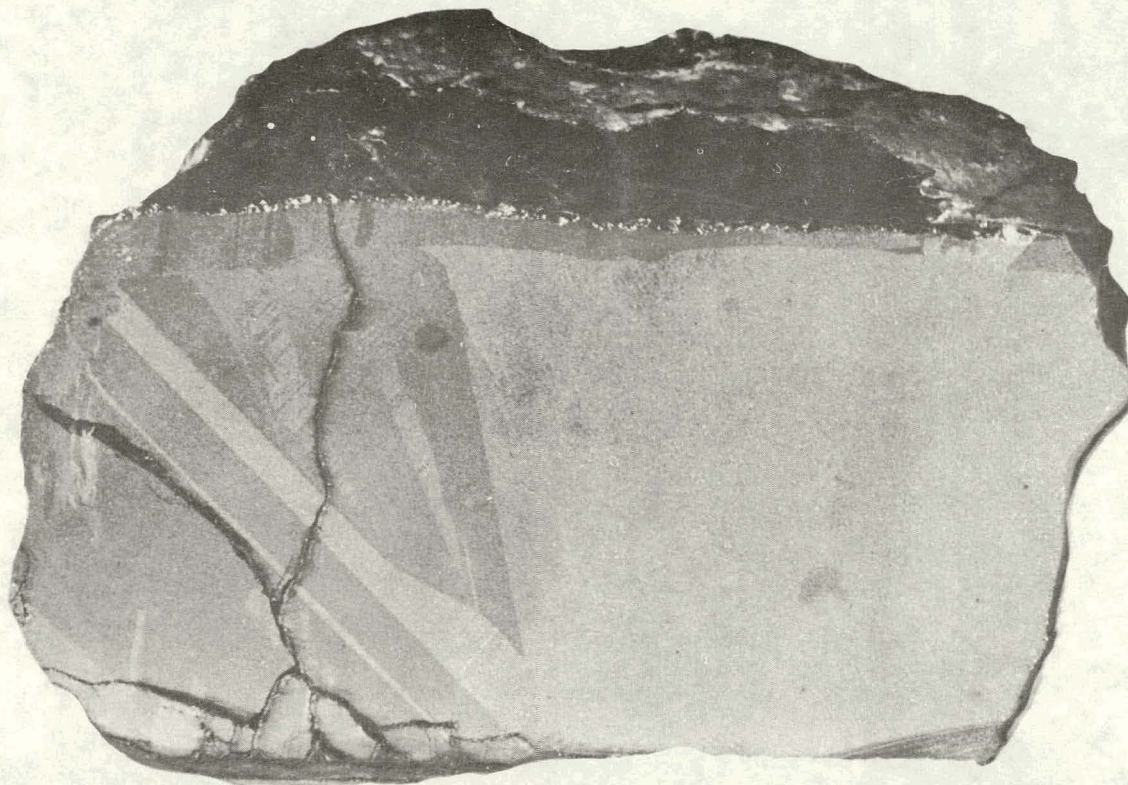


Figure 3. Polished and Etched Cross-section  
of Boule 47-C

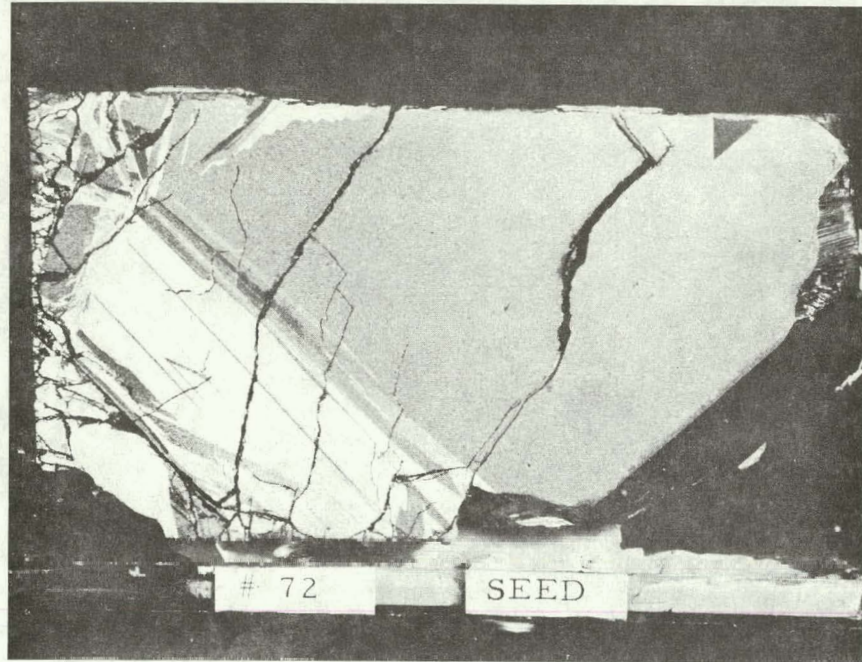


Figure 4. Polished and Etched Cross-section of  
Boule 72-C

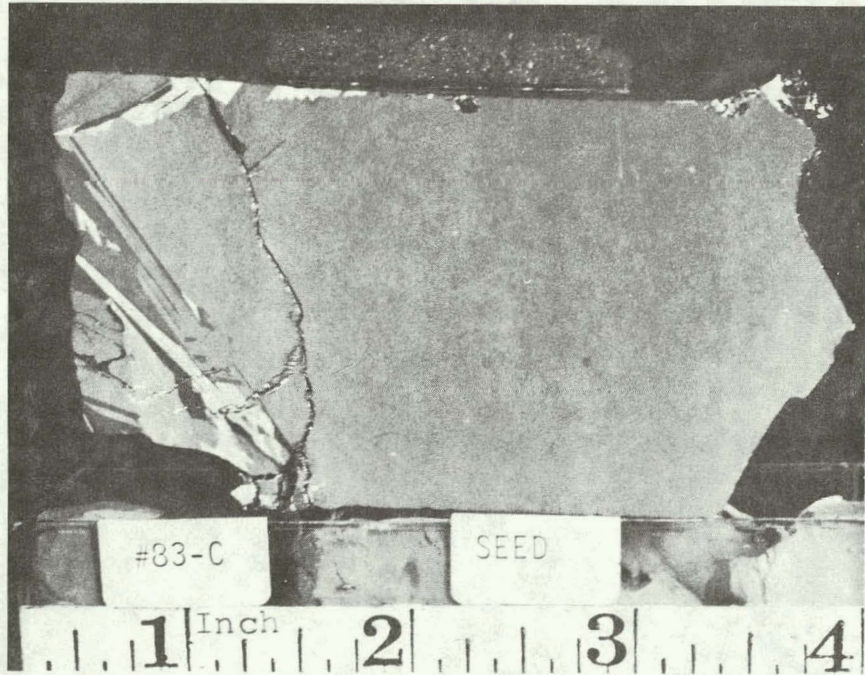


Figure 5. Polished and Etched Cross-section of  
Boule 83-C

One of the problems encountered in casting silicon in silica crucibles was that of cracking of the ingot during the cool-down cycle. This aspect will be dealt with in detail in Section 1.4. One solution was the use of thin-walled clear silica crucibles. Under these conditions the cracking was limited to the surface of the ingot. The structure of one such ingot is shown in the polished and etched cross-section of run 95-C in Figure 6. A high degree of single crystallinity along with some twinning was achieved.

The heat transfer characteristics are changed when using sintered crucibles rather than clear silica crucibles. The sintered crucibles are quite thick and therefore introduce considerable insulation between the furnace and the melt. In run 109-C extra silica powder insulation was added between the crucible and the retainer up to about three-fourths of the melt level to study its effect on heat flow. A polished and etched cross-section of this boule (Figure 7) shows that melt-back of the seed was achieved only on the sides and growth was promoted along the crucible wall. A clear demarcation at the top can be seen which coincides with the differences in insulation.

### 1.2.3 Improvement of Heat Extraction

The thermal conductivity of silicon in the molten state is more than twice that in the solid state.<sup>18</sup> This means that the extraction of heat by the heat exchanger is progressively

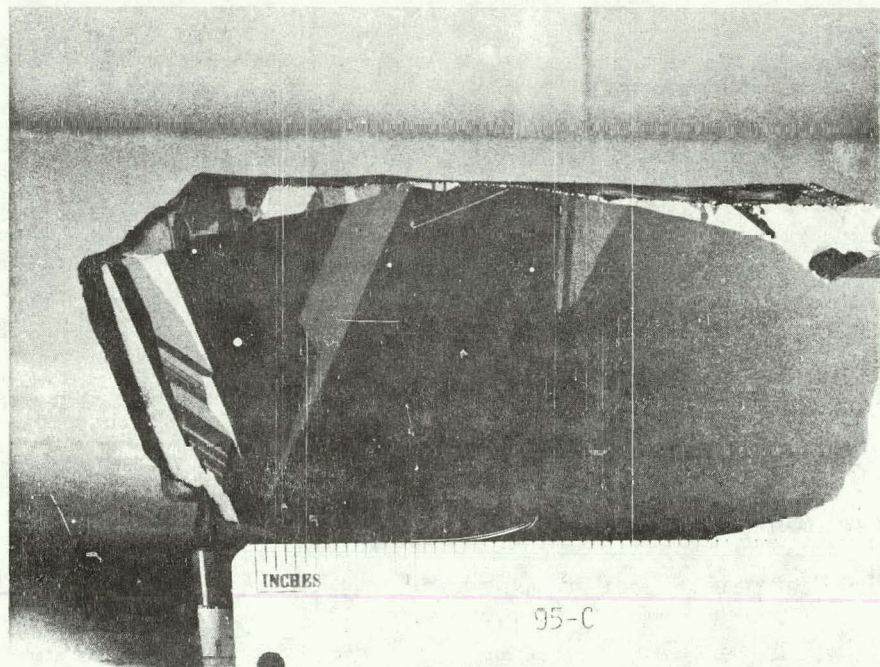


Figure 6. Polished and Etched Cross-section of Boule 95-C

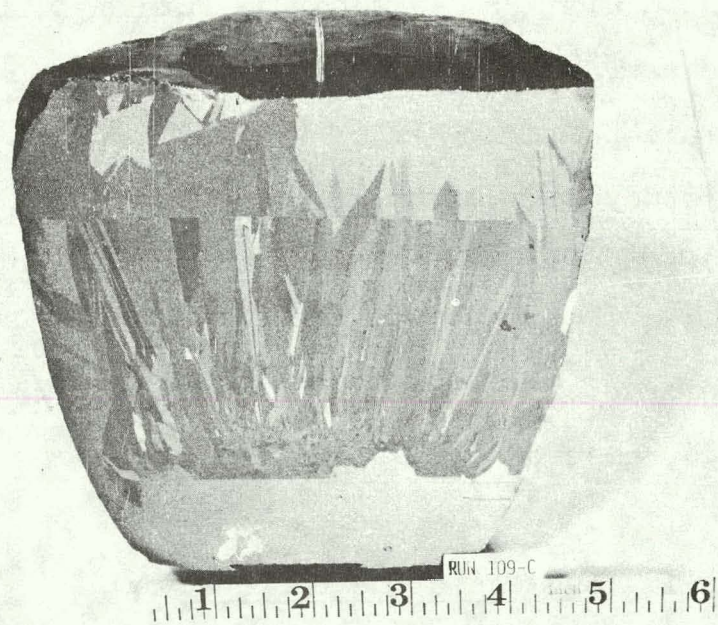


Figure 7. Polished and Etched Section of Boule 109-C  
Showing Melt-back and Growth on the Sides of Seed. Effect of Insulation Can Be Seen in Top Section.

impeded as the interface proceeds. This is further complicated by the fact that the conductivity of the silica crucibles drops significantly in the temperature range of seeding and growth cycles.<sup>19</sup> It has been demonstrated<sup>17</sup> that a silicon carbide coated graphite plug can be used through a hole at the bottom of a clear silica crucible for more efficient heat transfer. In order to study whether graphite plugs could be used instead of silicon carbide coated graphite plugs, further experiments were carried out to understand the following: (1) the formation of silicon carbide layer on graphite at high temperature; (ii) bonding of the seed to the plug to prevent it from floating in molten silicon<sup>20</sup>; (iii) the formation of a leakproof seal between the plug and the crucible even when the seed is melted out. The results of these experiments<sup>21</sup> showed that a leakproof seal can be formed between a graphite plug and the silica crucible. A 2 kg ingot was cast using such a technique in run 110-C. In spite of the furnace and heat exchanger temperature profiles being higher than regular runs, it was found that the heat transfer through the plug was more efficient. A polished and etched cross-section of boule 110-C (Figure 8) shows that no melt back of the seed was attained. Figure 9 shows a cross-section of boule 75 where the seed was melted out. The efficient heat transfer through the plug resulted in very large grains being formed.

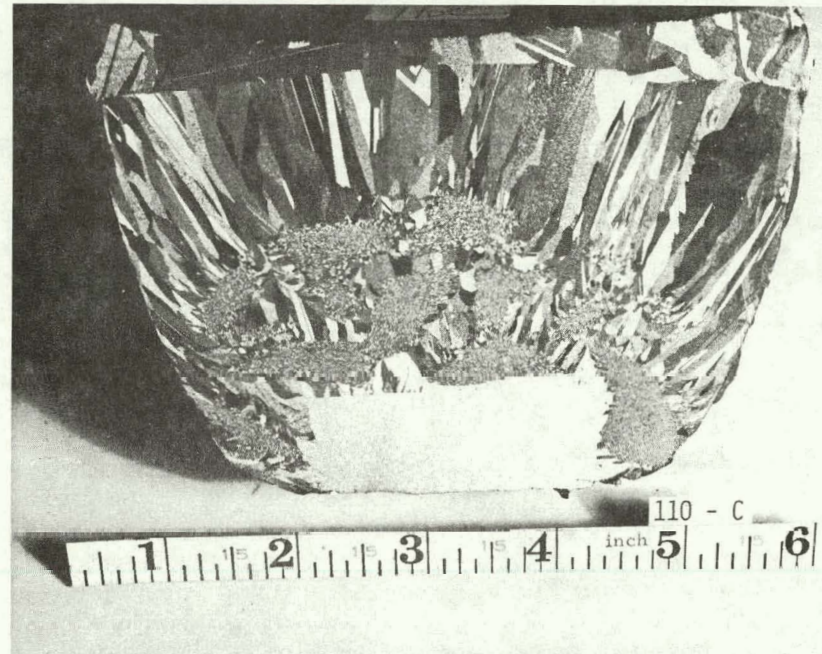


Figure 8. Polished and Etched Cross-section of Boule 110-C. Efficient Heat Transfer through Graphite Plug Prevented Seed Melt-back.

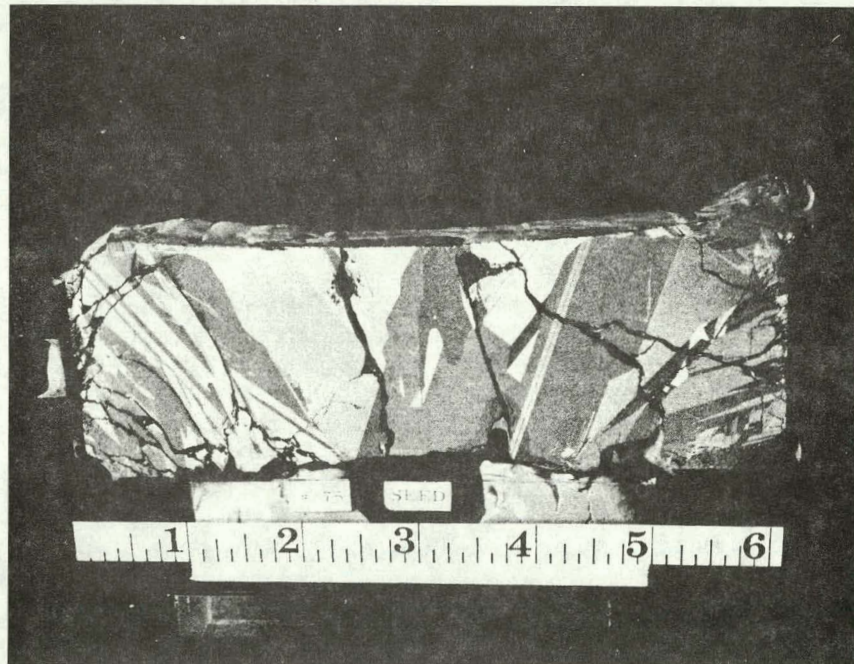


Figure 9. Polished and Etched Cross-Section of Boule 75-C.

### 1.3 MATERIAL CHARACTERIZATION

The silicon grown by the HEM was studied for crystallinity, orientation of grains, resistivity, dislocation density, minority carrier lifetime, and solar cell conversion efficiency.

#### 1.3.1 Crystal Structure

During the initial phases there were problems of proper "seeding" and therefore the resultant structure was rather poor. The material near the crucible walls was generally polycrystalline. This feature along with cracking of the ingot led to crumbling. A better control of the thermal flow characteristics along with crucible development showed less crumbling and cracking of the ingot, less penetration of molten silicon through the crucible walls and ease in removal of the ingot from the crucible. The best crystal structure ever seen in directionally solidified silicon was achieved in run 95-C. This 2.3 kg ingot was cast in a thin-walled clear silica crucible (wall thickness  $\approx$  0.045", 1 mm). A polished and etched section of this ingot is shown in Figure 10. Good seed melt back and growth were achieved. A large single crystal separated by twins exists, as shown by x-ray orientation analyses. The spots associated with the crystallographic directions A and B are about  $8^\circ$  off the  $\langle 110 \rangle$  orientation and are opposite of a twin boundary. Figure 11 shows the stereographic triangle locating these areas.

In run 103-C silicon was cast in a translucent graded crucible. There was no cracking of the ingot. A polished and

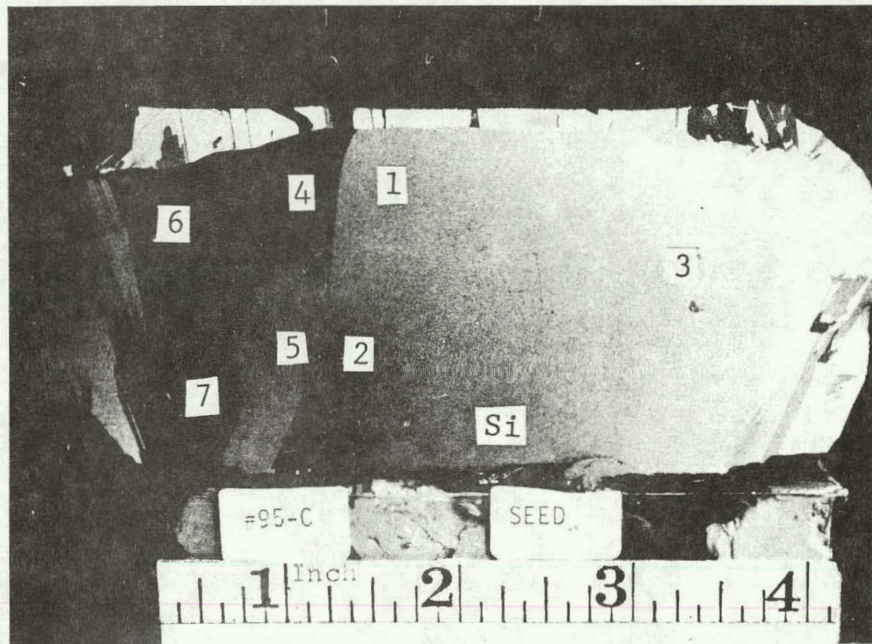


Figure 10. Polished and Etched Section of Boule 95-C.  
The numbers identify areas plotted on an x-ray stereographic triangle shown in Figure 11.

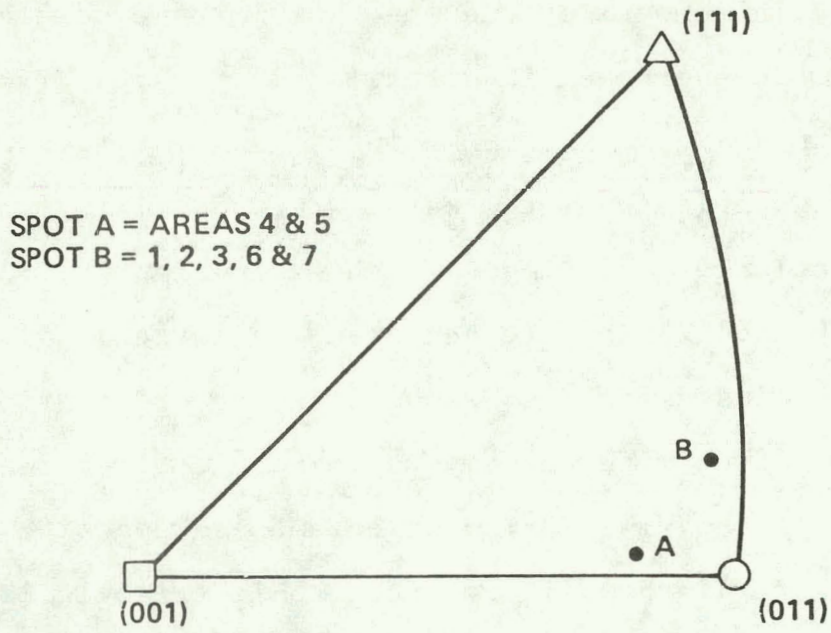


Figure 11. Orientation of Grains Perpendicular to the Cut Surface as Indicated by Spots on Figure 10, Plotted on a Stereographic Triangle

etched section is shown in Figure 12. The boule was almost all single crystal except some twinning on the sides. Good seed melt back was achieved; however, slightly beyond the new growth a twin plane developed and changed the orientation of the material.

### 1.3.2 Dislocation Density Measurements

A number of samples were studied for dislocation density in order to ascertain the quality of the HEM grown material. Each specimen was checked for orientation of the planes present in single crystal area. After orientation a major plane was exposed in order to determine dislocation density by the etch-pit method. The samples were ground through various abrasives with a final grind being #15 Microgrit (15 micron  $\text{Al}_2\text{O}_3$ ) on glass. The surfaces were then cleaned and etched in Dash etch ( $\text{HNO}_3$  : HF : Acetic Acid in 5 : 3 : 3) for about one minute followed by an etch in freshly prepared Sirtl etch (equal volumes of  $\text{CrO}_3$  solution and HF) for about 3 minutes. The samples were then washed, dried and examined on the metallograph. It was found that whenever good crystallinity material was obtained, the dislocation density was rather low as shown for some representative samples in Table I. These data are taken from as grown material with no post-annealing treatment.

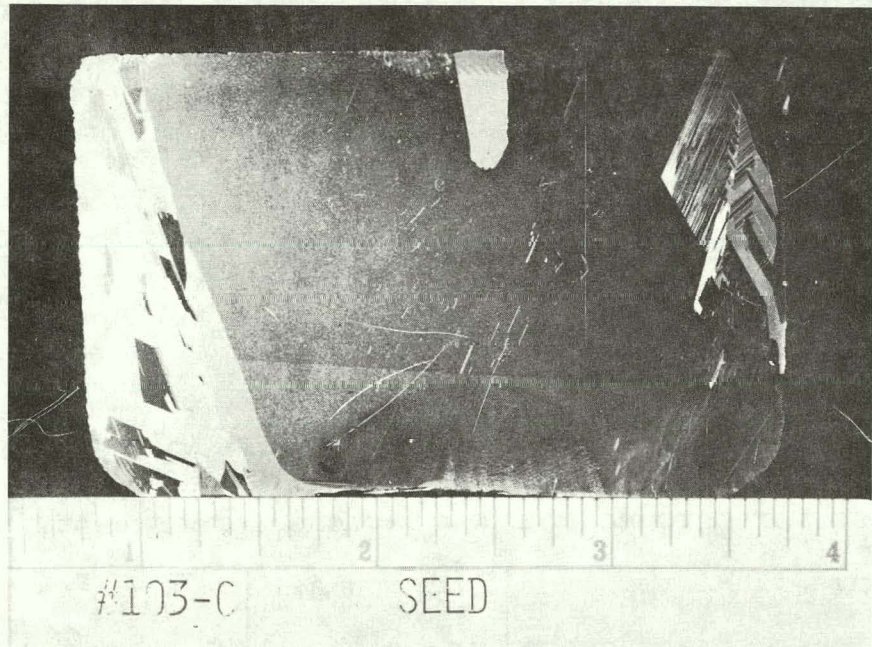


Figure 12. Polished and Etched Cross-section of  
Boule 103-C.

TABLE I. Dislocation Density Data on HEM Grown Boules

Run #	Dislocation Density	
	Seed Area/cm <sup>2</sup>	New Growth Area/cm <sup>2</sup>
26-C	$4 \times 10^2$	$(0.8-2) \times 10^2$
95-C	$7 \times 10^2$	$(0.2-1) \times 10^3$
103-C	$5 \times 10^3$	$(1-3) \times 10^3$
116-C	$(1-3) \times 10^3$	$(1-3) \times 10^3$

### 1.3.3 Lifetime Measurements

Minority carrier lifetime measurements were made on finished solar cells made from HEM grown material as well as control cells from Czochralski silicon. The technique used<sup>22</sup> is a variation of the open circuit voltage ( $V_{oc}$ ) decay method. The procedure is to forward bias the solar cells with a flash from a stroboscope and monitor the decay of the  $V_{oc}$ . This involves creating excess minority carriers in a junction using an external excitation, and monitoring the  $V_{oc}$  after this excitation has been abruptly terminated. The  $V_{oc}$  decay with time will have three distinct regions, viz., (i) a condition of high level injection; (ii) an intermediate level where excess minority carrier concentration in the base is greater than the thermal equilibrium minority carrier concentration, but less than thermal equilibrium majority carrier concentration; and (iii) a low level of injection.

The slope of the  $V_{oc}$  with time in the second stage is used to compute the minority carrier lifetime. Typical curves for a HEM grown and Czochralski grown silicon solar cells are shown in Figure 13 and results from other samples tabulated in Table II. The low lifetime for control samples may explain their low conversion efficiency (10.5 - 11% AMO).

Table II. Minority Carrier Lifetime Measurement Data

Sample	Lifetime (μsec)
HEM Silicon:	26C - 2
	72C - 2
	75C - 3
	95C - 1
Control Sample: *	26C
	72C, 75C
	95C

\*The numbers indicate the batch of HEM silicon the control samples are processed with.

#### 1.3.4 Solar-Cell Performance

Solar cells were fabricated and tested from the silicon grown by the HEM. This part of the work is provided by Optical Coating Laboratory, Inc., Photoelectronics Group in City of Industry, CA. The silicon sample was sent to OCLI as a chunk. The process sequence in fabricating the solar cells was as follows: An initial check was made of the conductivity type. Slices of cross-sectional area 2 cm x 2 cm were made which after cleaning were checked for resistivity and conductivity type. Control slices wer

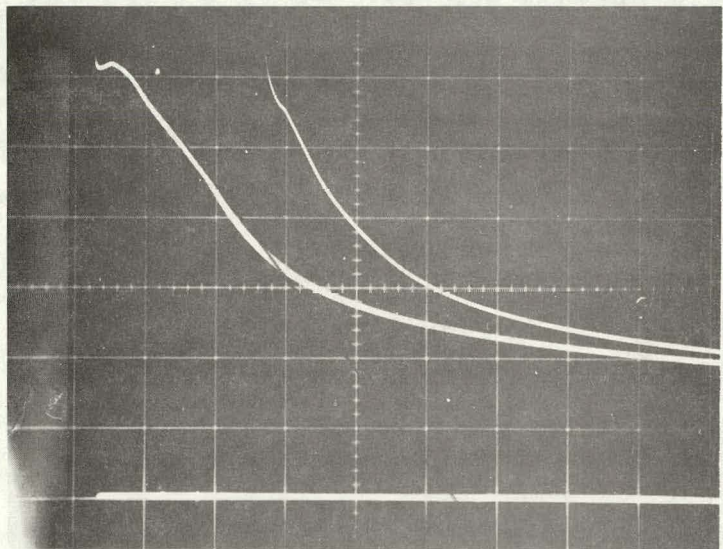
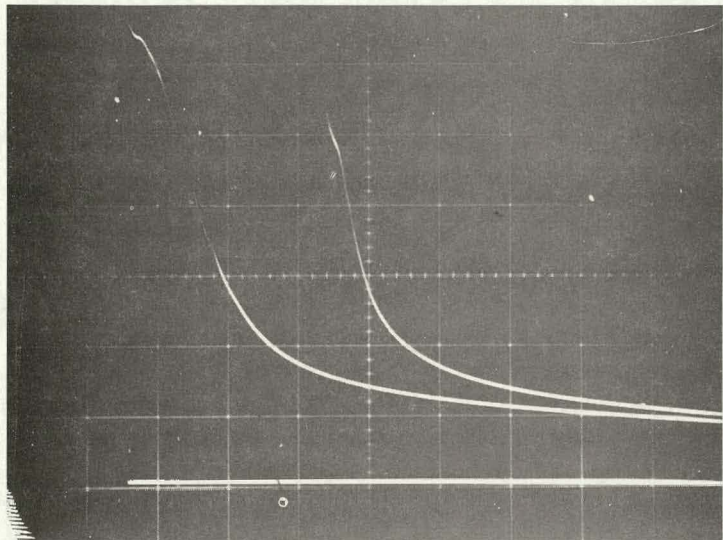


**Figure 13.** Typical  $V_{oc}$  Decay Curves for HEM and Control Samples. Scale: 0.1 V per division vertically and 100  $\mu$ sec per division horizontally. Top curve is for HEM cell 95C-1 and bottom curve is for control 95C.

added to the batch of test samples and they were all chemically polished. The back surface was protected during diffusion of a junction in  $\text{POCl}_3$  at  $875^\circ\text{C}$  for 15 minutes. The diffusion oxides were rinsed in HF acid. Front and back contacts were evaporated onto the samples. An  $\text{SiO}$  AR coating (in some cases) was formed by evaporation. A sinter at  $500^\circ\text{C}$  was carried out in hydrogen for 5 minutes followed by etching of the edge to clean the p-n junction. The solar cells thus fabricated were tested for I-V characteristics.

The first batch of solar cells were fabricated from an undoped ingot (run 26) with a resistivity of  $40-50 \Omega - \text{cm}$  and the efficiency was estimated at 6.6% (AM0), i.e., over 7% (AM1). The details of the I-V characteristics of other batches are shown in Table III. Assuming that the control samples are 11% (AM0) efficient, the efficiencies of the test samples are also tabulated. The solar cell conversion efficiencies, about 9% (AM1), are lower than expected because of impurity build-up in the furnace and thereby contamination of the silicon.

TABLE III. I-V Parameters (AMO) for Solar Cells Made  
from HEM Grown Silicon (DVM Readings)

Ingot	#	V <sub>oc</sub> (mV)	I <sub>sc</sub> (mA)	I <sub>450</sub> (mA)	CFF	AMO η %
72C	1	534	73.6	58.4	0.67	6.7
	2	537	73.6	60.8	0.69	6.9
	3	525	72.5	44.8	0.57	5.5
	4	538	75.3	53.8	0.63	6.5
75C	1	524	70.6	45.2	0.61	5.7
	2	529	68.0	53.1	0.68	6.2
	3	536	67.4	53.6	0.70	6.4
	4	536	66.7	54.4	0.70	6.3
Control	1	579	105.8	98.1	0.72	11.0
Control	2	579	100.8	96.2	0.74	11.0
95C	1	570	103.2	91.6	0.71	7.5
	2	564	105.2	82.5	0.65	6.9
	4	568	102.7	87.3	0.67	7.0
	5	558	101.6	80.0	0.63	6.4
	6	567	100.7	80.7	0.64	6.6
	7	565	105.5	88.9	0.67	7.2
	8	572	104.6	94.3	0.72	7.7
	9	569	104.3	96.2	0.74	7.9
Control		584	130.2	126.2	0.77	10.5

## 1.4 CRUCIBLE DEVELOPMENT

One major problem in casting silicon in silica crucibles is their bonding at high temperatures which results in the silicon cracking during the cool-down cycle. In clear crucibles there invariably appears to be attachment of the crucible to the ingot with a visible brown deposit, presumably  $\text{SiO}$ , sandwiched in between. A sample from run 89-C was examined with SEM. Figure 14 shows a micrograph of the boundary with cracking in the crucible as well as in the ingot. Microcracking is observed all along the interface. A visual examination showed that a dark brown band was present almost parallel to these cracks. The EDAX indicated that the silicon counts in the three regions (Figure 15) to be as shown in Table IV. A comparison of these data with the silicon counts calculated for  $\text{Si}=100\%$ ,  $\text{SiO}=64\%$ , and  $\text{SiO}_2=46\%$  indicates that the brown deposit is probably  $\text{SiO}$ .

TABLE IV. EDAX Counts in Three Areas of Figure 15

POSITION	MATERIAL	Si COUNTS/ UNIT TIME	NORMALIZED Si COUNTS/ UNIT TIME
Upper left corner	Silica, $\text{SiO}_2$	457	37
Middle	Brown interface	869	71
Lower right corner	Silicon, Si	1225	100

Figure 16 shows a polished and etched cross-section of a boule from run 74-C. X-ray analysis shows that areas marked



Figure 14. SEM Examination of Silica/Silicon Interface

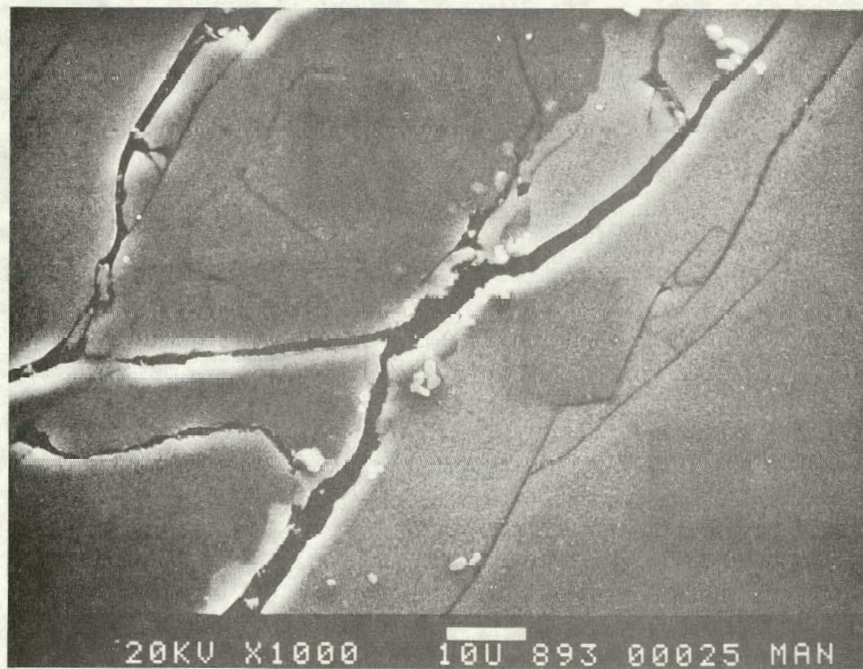


Figure 15. A Higher Magnification of Figure 14 Showing Areas where EDAX Counts Were Taken

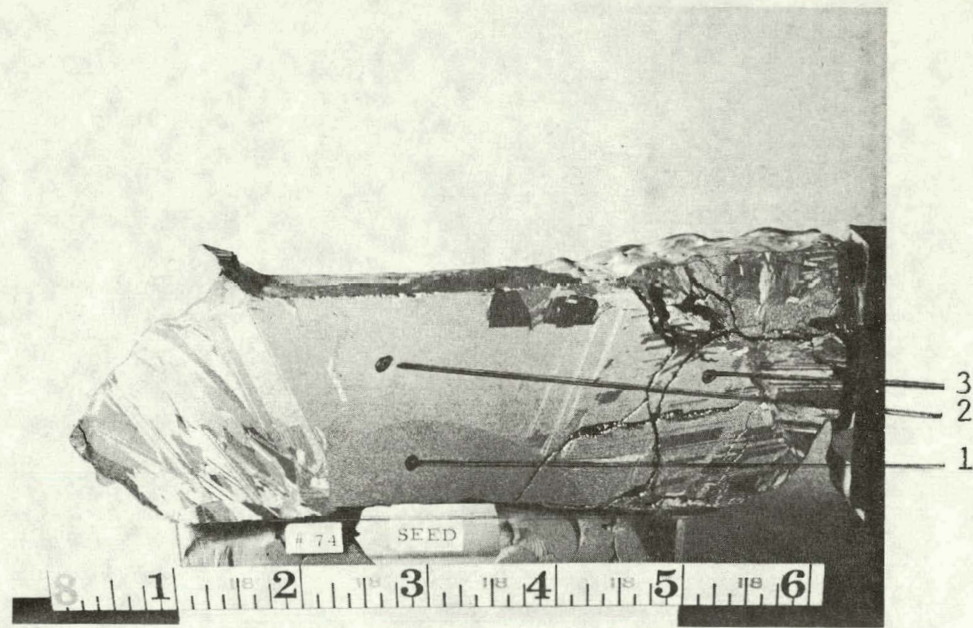


Figure 16. Polished and Etched Cross-section of Boule 74-C Showing Lateral Growth

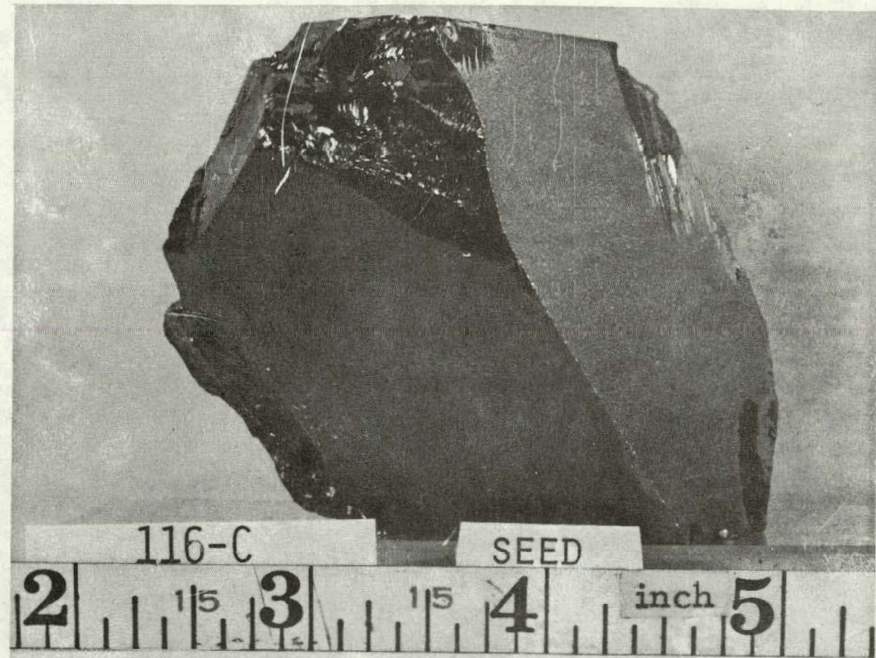


Figure 17. "As Removed" Fractured Section of Silicon Cast in a Clear Silica Crucible

1, 2, and 3 have the same orientation, indicating that the cracking took place after crystal growth was complete. Solidified ingots were viewed with a fiber optic light source and it was confirmed that cracking occurred during the cool-down cycle around 650°C. This coincides with the ductile-brittle transition of silicon.<sup>23</sup> Above this temperature it appears that silicon flows plastically to strain relieve itself.

Different kinds of sintered crucibles as well as clear silica crucibles have been used to cast silicon<sup>21</sup>. It has been found that, unlike the case of clear crucibles, the sintered silica crucibles attached only in some areas. Directional solidification and "seeded" growth were the most severe tests for cracking. Ingots solidified under other than these conditions, at times, were found to be crack-free.

Detailed phase identification and density measurement on crucible samples and microscopic examination of the silicon/silica interface samples led to the development of graded silica crucibles which were used to cast large crack-free silicon ingots.

#### 1.4.1 Clear Silica Crucibles

The use of fully dense clear silica crucibles always resulted in cracking of the silicon ingot. Even when silicon was heated to high temperatures, without going to the molten state, and cooled, the pieces of polycrystalline material near the silica showed attachment and signs of cracking. This cracking behaviour was not random but was characteristic in nature. This is clearly

illustrated by a fractured section (Figure 17) which is "as removed" from the crucible. It is a pyramidal shaped material, the surfaces of which are defined by smooth planar {111} surfaces. The bottom is part of the {111} seed surface. This is consistent with the report<sup>24</sup> that in silicon slip occurs in {111} planes. The shape of the section is as one would expect with {111} planar surfaces.

It is reported<sup>25,26</sup> that beryllium, aluminum and gold additions to silicon have prevented cracking of the ingot. However, in the present development of silicon for photovoltaic applications, this is not desirable. Hino and Stauss<sup>27</sup> have used clear silica crucibles, 0.25 to 0.50 mm wall thickness, to produce sound ingots 30 mm diameter weighing 50 to 100 gms. This procedure was attempted to grow 15 cm diameter, 2 to 2.5 kg ingots in fused silica clear crucibles with wall thickness about 1 mm. A 2.3 kg ingot cast in run 93-C is shown in Figure 18. It can be seen that the cracking was restricted to the surface of the ingot. The cracks extend about 50 to 100 microns into the bulk. A need, therefore, arises to grind the surface of the ingot before fabrication into solar cells which involves extra cost and loss of material. The integrity of such thin crucibles for casting large ingots is also questionable.

The casting of silicon in thin-walled crucibles relies on the fact that the crucible fails during the cool-down cycle and thereby relieves the stress and hence prevents cracking of the silicon ingot. Thus the crucible must resist penetration of molten silicon during solidification and be weak enough to fail during cool down.

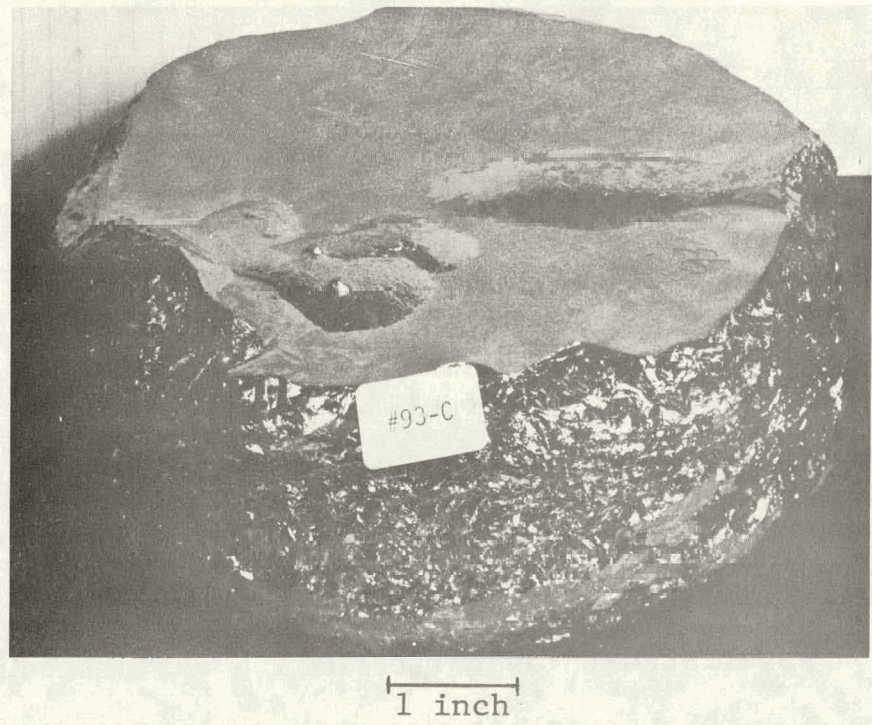


Figure 18. Crack-free Silicon Boule Obtained in Run 93-C.



Figure 19. Crack-free Silicon Cast in a Coated Crucible.

#### 1.4.2 Coated Crucibles

Since silicon bonds to silica and the use of thin wall crucibles restricts cracking to the surface of the ingot, it was felt that a spray coating inside the clear silica crucible would be sacrificially utilized. Silicon would adhere to the coating and the coating would peel off from the crucible during cooling, thereby causing no cracking of silicon. A number of experiments using this technique were tried and some small crack-free ingots were cast. However, the common problem in all these experiments was that molten silicon penetrated through the coating and attached to the crucible. In cases where penetration was rather limited, as for smaller samples, the ingots were sound (Figure 19) but generally the coating was removed partially because of the reaction with silicon to form SiO. Efforts were made to form a surface glass phase on the coating which would resist penetration. The high porosity resulted in a poor continuous glass layer so this approach was not satisfactory.

#### 1.4.3 Hot Pressed Crucible

In order to solve the cracking problem, it was felt that a sintered silica crucible would fail during the cool-down cycle because of the various phase transformations<sup>28,29</sup>. A hot-pressed crucible was initially attempted in order to avoid penetration of molten silicon. During run 84-C crack-free silicon was cast, a section of which is shown in Figure 20. However, when directional solidification was carried out, run 90-C, the ingot cracked. It

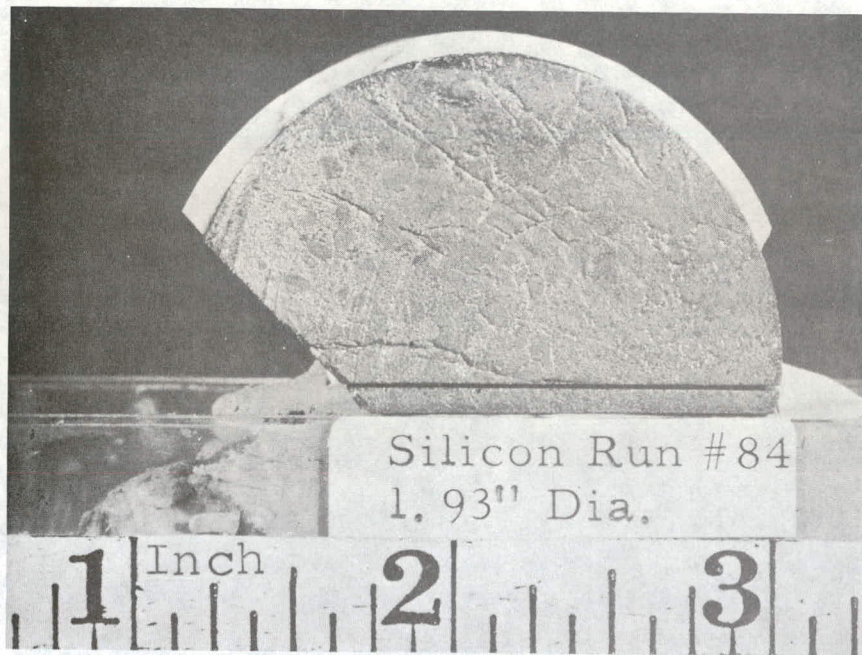


Figure 20. A Section of the Crack-free Silicon Cast in a Hot-pressed Crucible

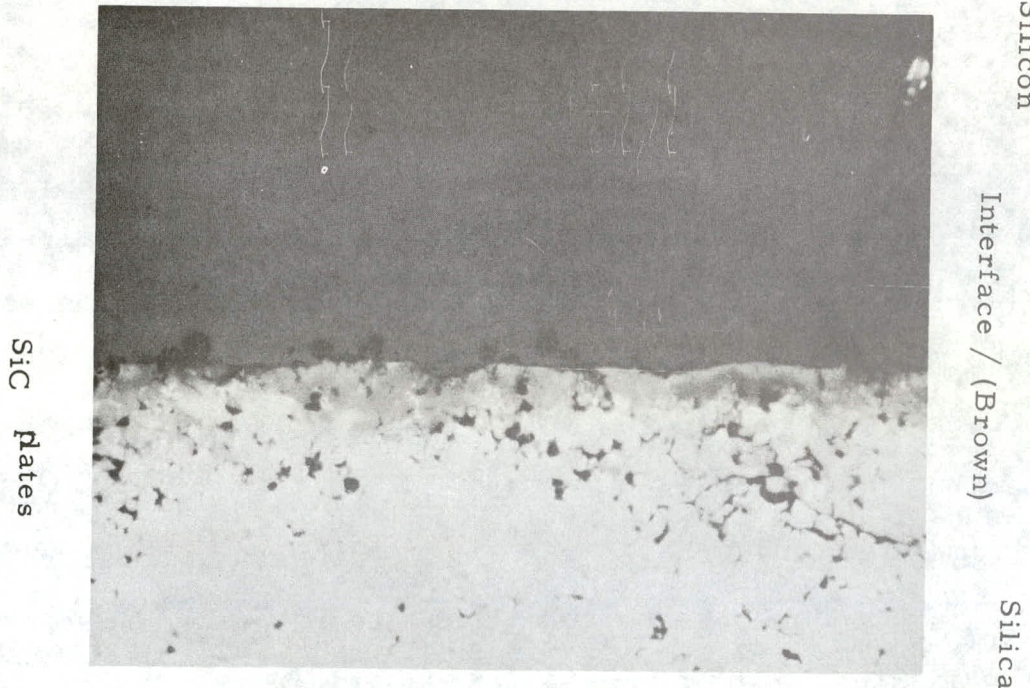


Figure 21. Optical Micrograph (100X) under Polarized Light for Hot-pressed Crucible

was found that silicon showed attachment in some areas to the crucible whereas in other areas it broke free easily. A section from the top portion of the crucible which was not in contact with silicon showed that it had sintered to about 98% of theoretical density and turned into a distorted cristobalite phase. Optical micrograph examination of the silicon/silica interface (Figure 21) shows that there was no penetration of silicon into the crucible, and a layer of SiO was observed as a brown deposit, the extent of which varied in different areas. This seems to be responsible for attachment of silicon to silica in some areas only.

#### 1.4.4 Pressure Cast Crucibles

The hot pressed crucibles did not show penetration of molten silicon but did not solve the cracking problem. It was intended to reduce the density of the crucible and thereby weaken it to fail during cooling. Pressure cast crucibles were fabricated using slips made from 8  $\mu\text{m}$  and 25  $\mu\text{m}$  particle size silica powders. The slip was poured into a graphite mold through a plunger and the slip was settled under an air pressure. These crucibles were used to cast silicon in run 90-C (Figure 22). The behaviour was similar to the hot-pressed crucibles. Optical metallography and density measurements showed that the 8  $\mu\text{m}$  was sintered to a finer grain size and denser structure than the 25  $\mu\text{m}$  pressure cast, thereby showing less of a reaction SiO layer (Figure 23).

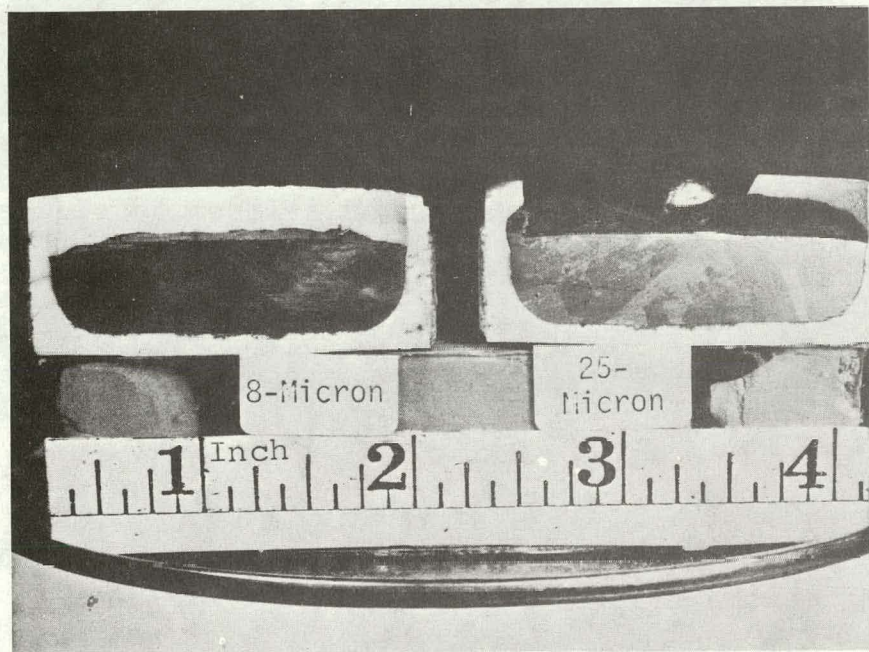


Figure 22. Crack-free Silicon Cast in Pressure Cast Crucible (Run 90-C)

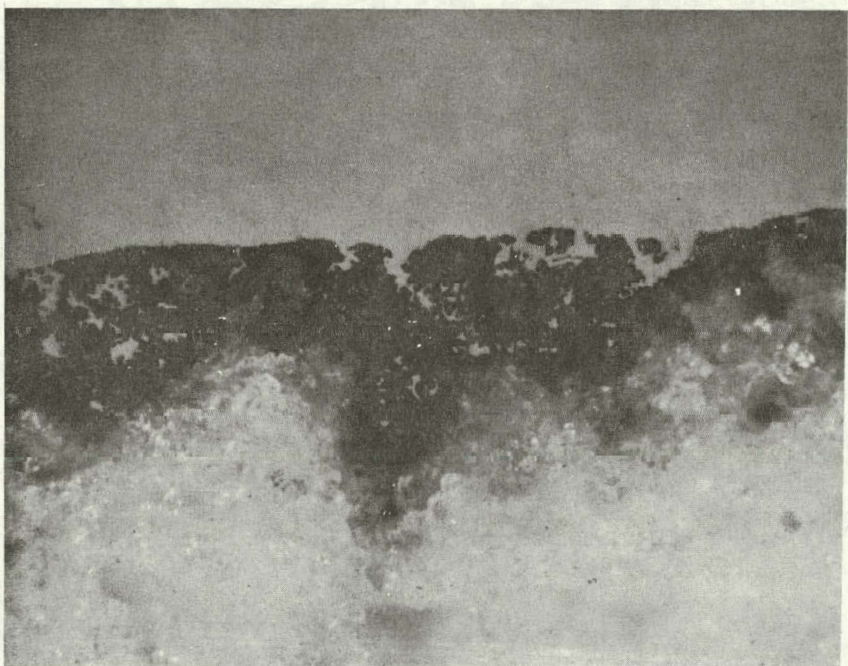
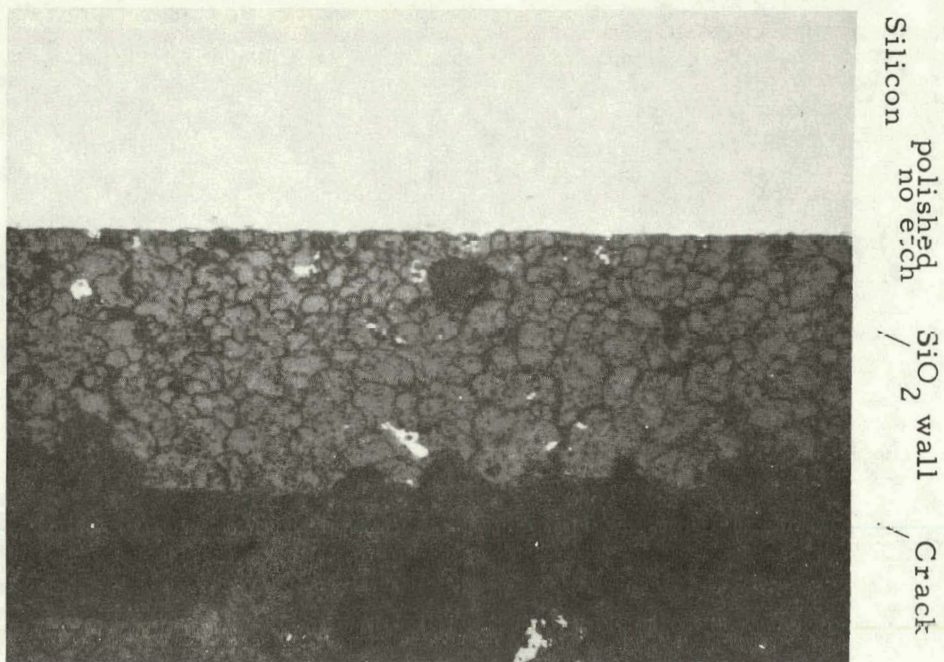


Figure 23. Optical Micrograph (100X) Showing the Silicon/Silica Interface for 8  $\mu\text{m}$  (above) and 25  $\mu\text{m}$  (below)

#### 1.4.5 Slip Cast Crucibles

In an effort to reduce the strength of the crucibles further, slip-cast crucibles were fabricated. Both the high purity as well as technical grade silica crucibles were used. The latter grade was expected to have a high alkali content which would aid the cristobalite formation leading to failure during cooling. Even though crack-free silicon was cast (Figure 24) the molten metal penetration was a problem (Run 92-C).

In addition, samples of low density crucibles have shown that sintering during ingot growth resulted in densification to above 95% of theoretical density<sup>6</sup>, hence the crucible did not fail during cooling.

In order to prevent penetration a thin glass layer was developed by heat treatment in the slip-cast crucible which showed no signs of ingot cracking (Figure 25). Many ingot casting experiments confirmed that this type of crucible was essential to casting crack-free silicon ingots in silica crucibles. The interior of the graded crucible was a continuous glass phase and the exterior low density. The gradation of the crucible across the wall thickness has to be with respect to density as well as phase composition.

#### 1.4.6 Graded Crucibles

An opaque graded crucible was used to consistently cast crack-free silicon ingots. Figure 26 shows the as-cast surface of a

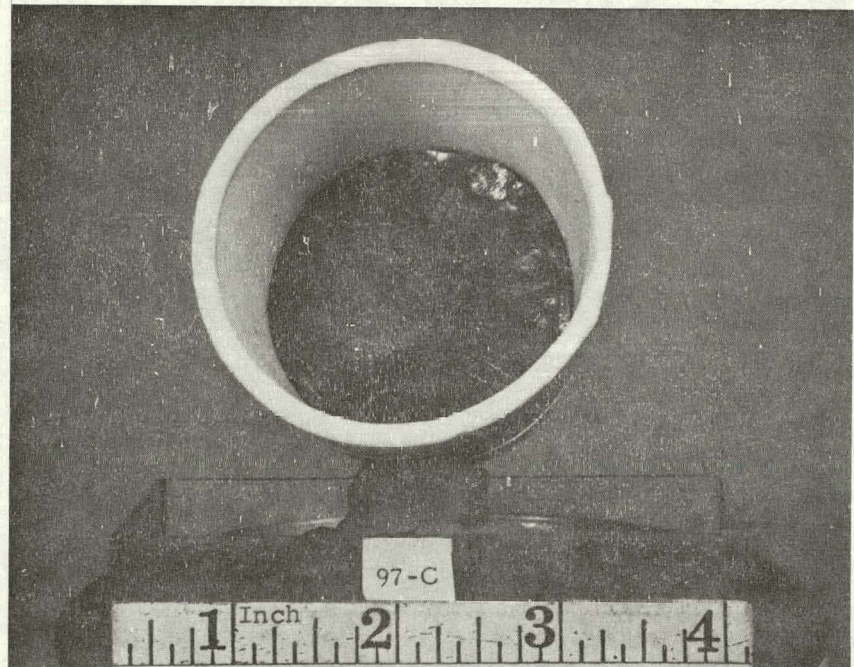
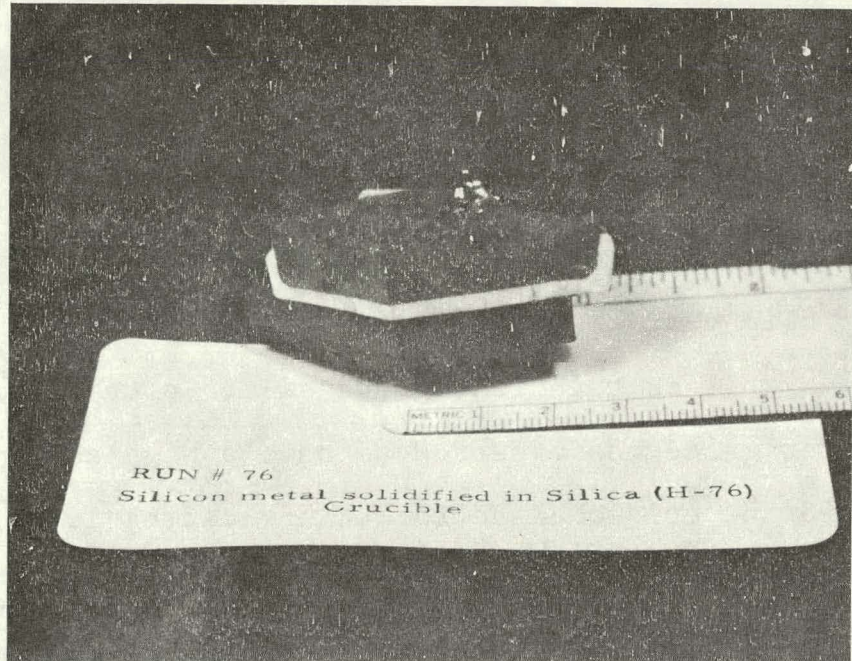


Figure 24. Crack-free Silicon Cast in High Purity (above) and Technical Grade (below) Slip Cast Crucibles

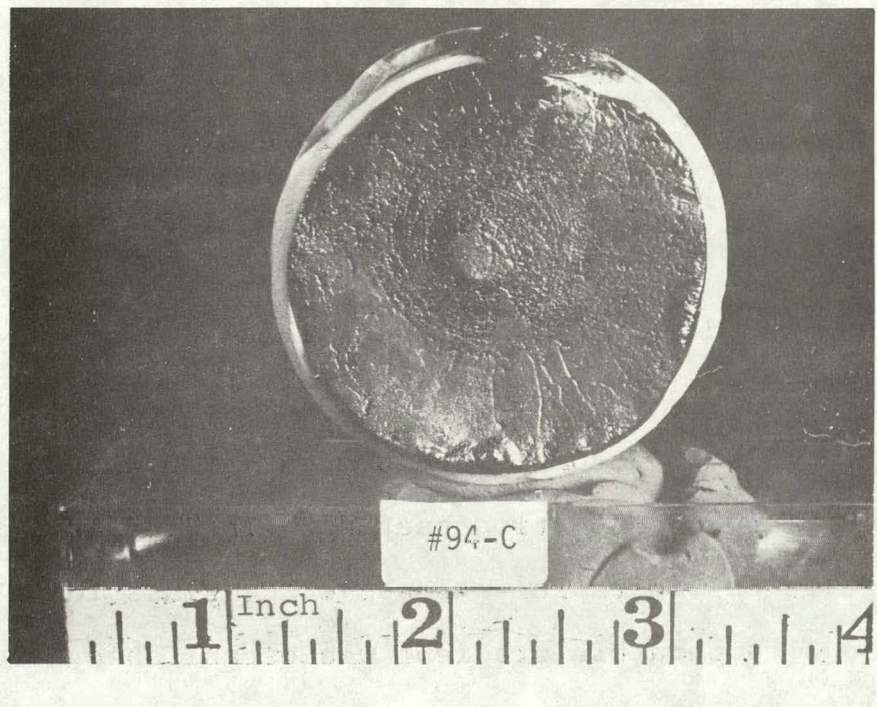


Figure 25. Crack-free Silicon Cast in a Glazed Crucible



Figure 26. Crack-free 3.3 Kg Silicon Boule Cast in Run 109-C

3.3 kg ingot from run 109-C. In Figure 27 an optical micrograph shows a section of the unused crucible with a dense inner layer and low-density backing. Figure 28 shows the structure after casting.

The graded structure in the silica crucibles is developed with respect to structure, cristobalite phase composition, and density. This is accomplished by heat treatment using flame, electrode, arc or induction heating. The inside surface of the crucible is raised rapidly to above the glass formation temperature and a temperature gradient was established across the crucible wall. Rapid heating and cooling ensures a dense glass interior phase. The temperature gradient causes a variation in density and cristobalite phase composition across the wall of the crucible. Further, this gradation in phase results in micro-cracking behind the dense interior layer. During cool-down cycle, the crucible delaminates, thereby preventing the silicon ingot from cracking.

A graded structure was also developed in a translucent silica crucible and an ingot from run 103-C is shown in Figure 29. An optical micrograph of the crucible after run 104-C is shown in Figure 30.

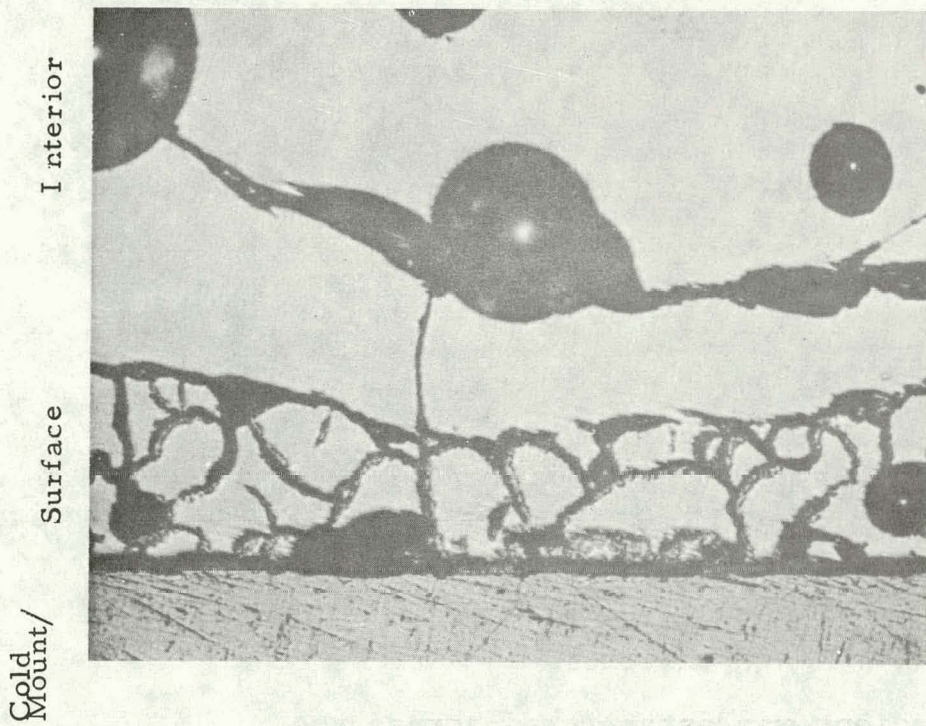


Figure 27. Optical Micrograph (250X) of a Section of Graded, Opaque Silica Crucible before Casting Silicon

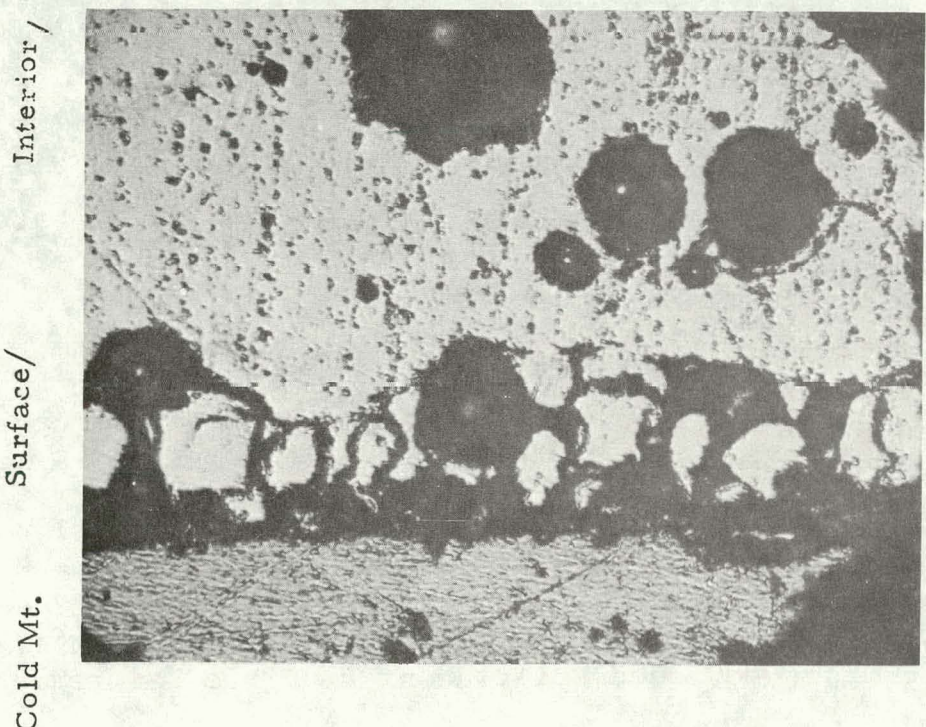


Figure 28. Optical Micrograph (250X) of a Top Section of Graded, Opaque Silica Crucible after Casting Silicon

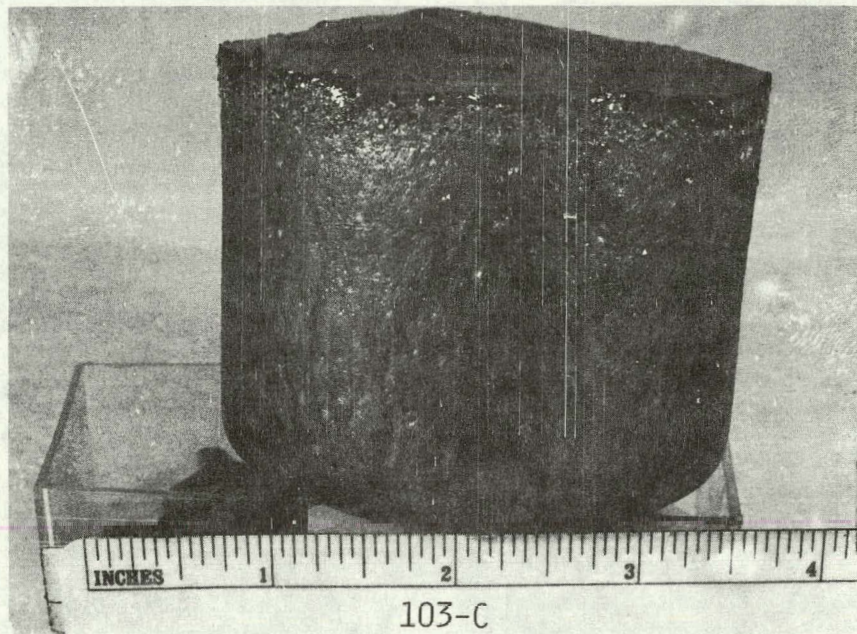


Figure 29. Crack-free Silicon Boule Cast in Run 103-C  
Using a Graded, Translucent Silica Crucible

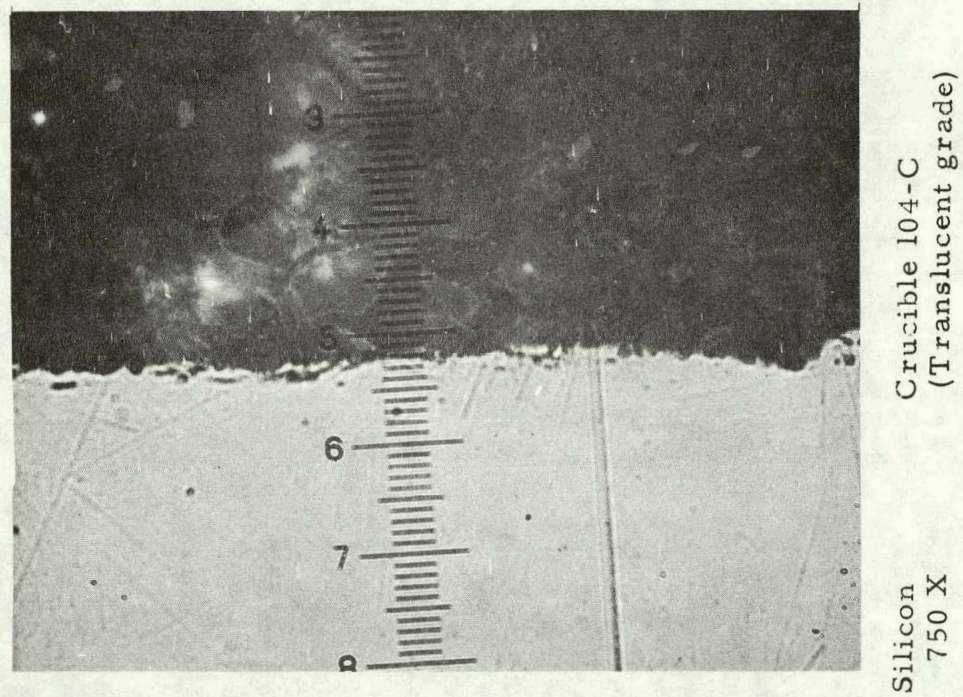


Figure 30. Optical Micrograph (750X) of the Silicon/  
Graded Translucent Crucible Interface

## 1.5 HEAT FLOW

The HEM is a simple process with no moving parts. The whole method is based on extraction of heat from the melt through the bottom by the heat exchanger. Therefore, the heat flow is very important in achieving good crystal growth. The thermal characteristics are all affected by the temperature profile in the furnace, control of heat input, size and shape of insulation around the melt, environment in the vicinity of the heat exchanger, heat extraction, etc. The heat flow characteristics for sapphire growth by the HEM have been established.<sup>30</sup> In case of silicon growth, the situation is complicated by a number of parameters, e.g., the conductivity of the liquid phase is higher than the solid phase,<sup>18</sup> the variation and poor conductivity of silica crucible,<sup>19</sup> the need to support the crucible with a retainer, etc. So far the emphasis in the program has been to find a suitable crucible which prevents cracking of the ingot. The size and shape of the container has not been specified; instead commercially available crucibles have been used after suitable heat treatment. Now that the type of crucible has been established, efforts will be concentrated on the heat flow to achieve fast growth rates and high crystallinity in the silicon ingot cast.

### 1.5.1 Theoretical Model

A finite difference thermal model was developed for the HEM growth of silicon using a general numerical differencing program, SINDA, in association with JPL. The features of this program

include subroutines for simulating phase changes and plotting isotherms which correspond to phase boundaries.

Calculations were based on a clear silica container 15 cm in diameter, 20 cm high with a wall thickness of 2.5 mm held in a graphite retainer and placed on a molybdenum heat exchanger. The physical properties of the various elements were taken from reported data.<sup>31</sup> The model was simplified by assuming that all furnace surfaces are at constant temperature. A sight port at the top of the chamber was assumed at 800°K. The melt temperature was taken as 1685°K and that the heat of solidification is released between 1685°K and 1685.01°K. The variation of the properties are incorporated in the computer program.

Initially a steady solution was calculated. This was done by assuming a nodal arrangement in the melt as shown in Figure 31. The calculations are being carried out for only one side of the center line. It should be symmetric for the other side. The isotherms obtained for the steady state solution of a furnace temperature of 1687°K are shown in Figure 32. It can be seen that the top sight port has a cooling effect on the central portion of the surface of the melt.

The steady state solution was used as a starting point of the transient solution, when the heat exchanger temperature was lowered to propagate growth of the crystal. Six different cases of heat exchanger decrease rate were calculated, including a 'step change' case when this temperature was lowered from 1683°K to 700°K. The effect of this on solidification time is shown in

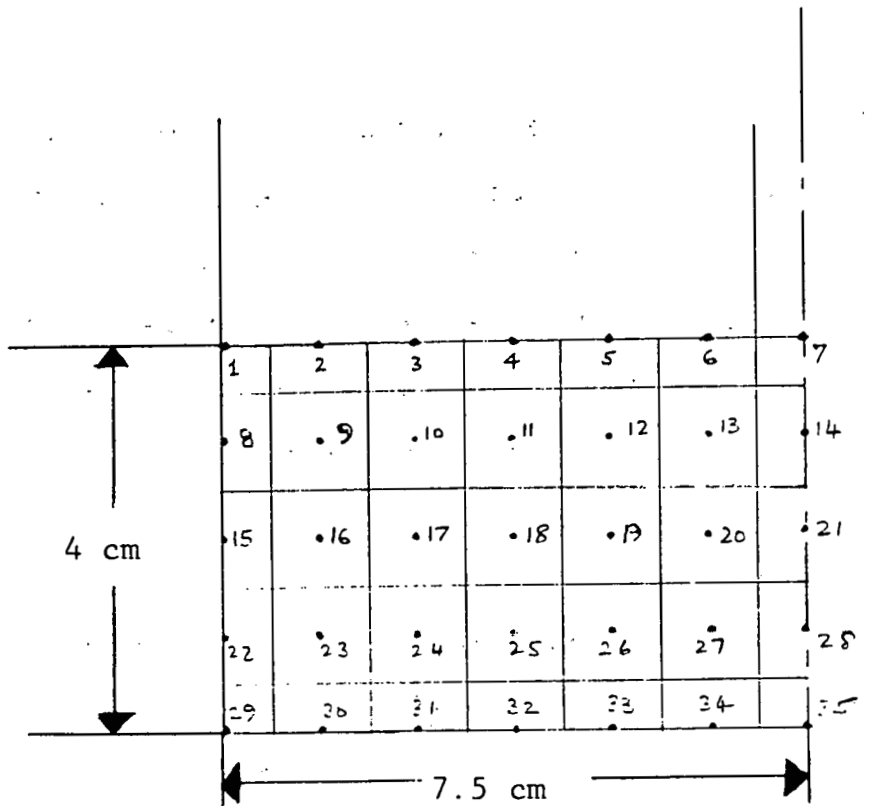


Figure 31. Nodal Arrangement in the Melt for the Finite Difference Model of Heat Flow

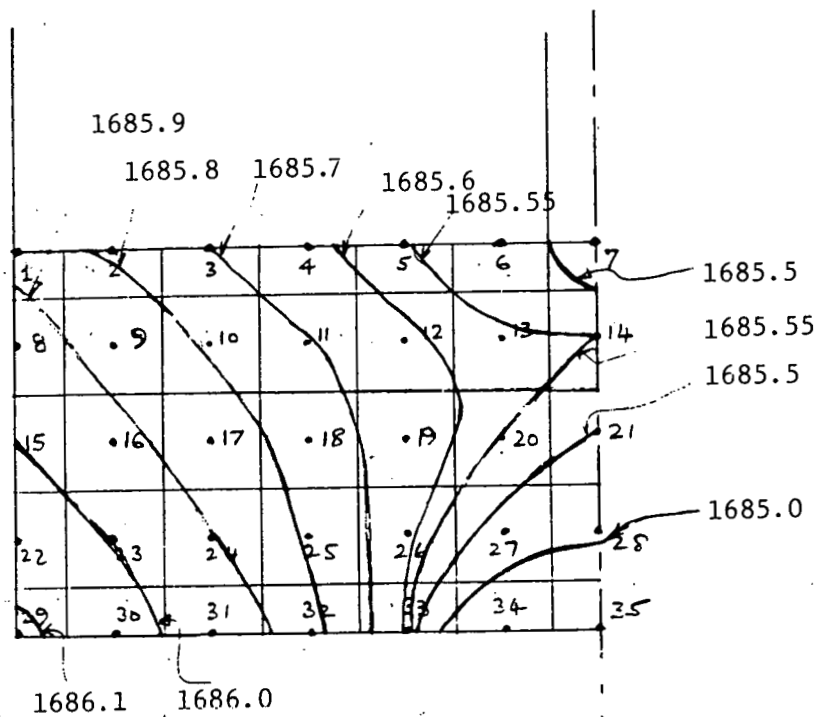


Figure 32 Steady State Solution Showing the Various Isotherms for Different Regions in the Melt

Figure 33. It can be seen that the faster the heat exchanger temperature is lowered, the shorter is the growth time. These calculations are based on the use of a graphite plug at the bottom of the crucible to enhance the heat transfer. An estimate of the growth time for a  $170^{\circ}\text{K}/\text{hour}$  decrease in heat exchanger temperature showed that growth time was reduced from 6.39 hours to 4.55 hours with the use of the graphite plug. Figure 34 shows the calculated shape of the solidification front as a function of time for the case of  $170^{\circ}\text{K}/\text{hour}$  heat exchanger temperature decrease. Similar shapes are obtained for other cases.

In the above analysis it has been assumed that the heat exchanger size is 2.5 cm. The effect of increase in size of the heat exchanger on the growth time is shown in Figure 35. This calculation is based on  $500^{\circ}\text{K}/\text{hour}$  decrease in heat exchanger temperature.

One of the shortcomings of the model is that it does not show any sensitivity of the superheat in the melt to the growth time. This is contrary to experimental evidence where it is seen that superheat prolongs the growth time considerably.

### 1.5.2 Theoretical Growth Rate

In deriving the equation for growth rate, it is assumed that the interface is hemispherical. The symbols and constants used are shown in Table V. In run 42-C the temperature in different regions of the heat exchanger was monitored as a function of the flow rate of helium. The results are shown in Figure 36.

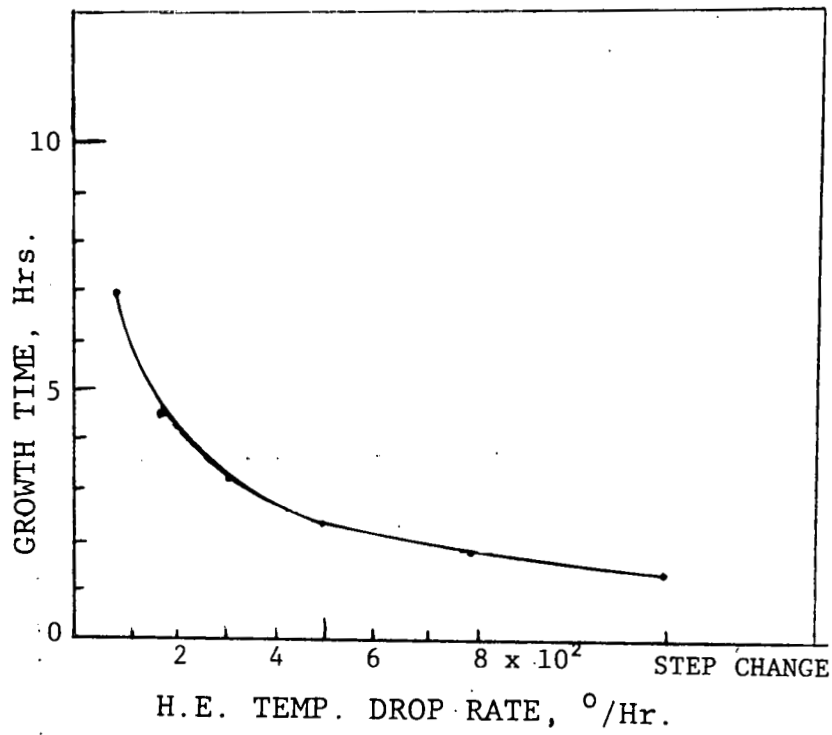


Figure 33. Effect of Rate of Decrease of Heat Exchanger Temperature on Solidification Time

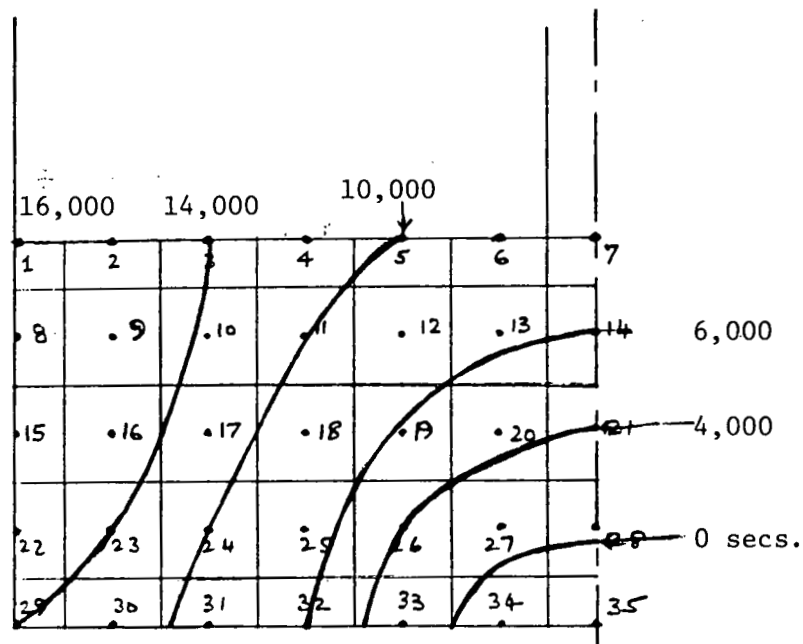


Figure 34. Shape of Solidification Front as a Function of Time

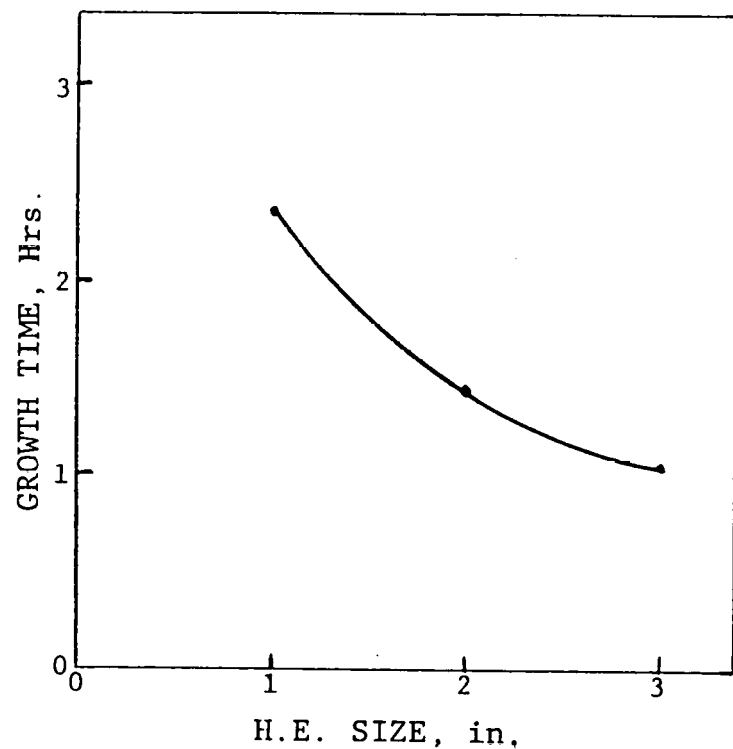


Figure 35. Effect of Size of Heat Exchanger on Growth Time

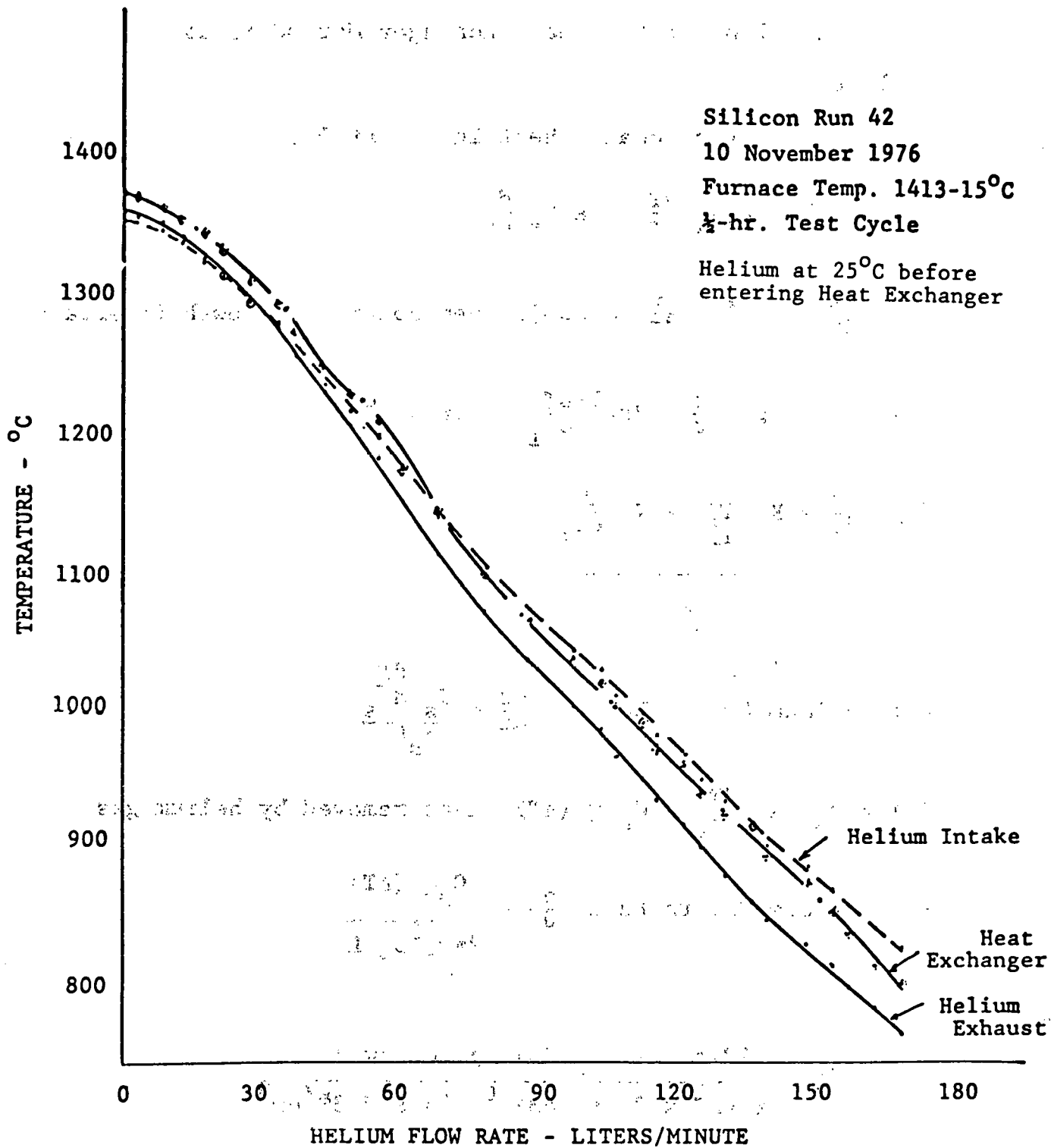


Figure 36.

Heat Flow for the Heat Exchanger Method is as follows:

$$\text{Latent Heat} + \text{Heat In} = \text{Heat Out}$$

$$(1) L \frac{dm}{dt} + A_1 K_1 \frac{dT}{dr_1} = A_s K_s \frac{dT}{dr_s}$$

$$(2) \frac{dm}{dt} = 2\pi r^2 \rho_s \frac{dr}{dt} \text{ assuming hemispherical growth interface}$$

$$(3) 2\pi r^2 L \rho_s \frac{dr}{dt} + 2\pi r^2 \frac{dT}{dr_1} = 2\pi r^2 K_s \frac{dT}{dr_s}$$

$$(4) \frac{dr}{dt} = \frac{K_s \frac{dT}{dr_s} - K_1 \frac{dT}{dr_1}}{\rho_s L}$$

$$(5) \text{Maximum Growth Rate} \quad \frac{dr}{dt} = \frac{K_s \frac{dT}{dr_s}}{\rho_s L}$$

$$(6) 2\pi r_s^2 K_s \frac{dT}{dr_s} = C_p Q (\Delta T) \text{ heat removed by helium gas}$$

$$(7) \text{Maximum Growth Rate} \quad \frac{dr}{dt} = \frac{C_p Q (\Delta T)}{2\pi r_s^2 \rho_s L}$$

$$\frac{dr}{dt} = \frac{.2215 \text{ Cal/1}^{\circ}\text{C} (\Delta T^{\circ}\text{C}) Q \text{ 1/min}}{r^2 \text{ cm}^2 \times 2\pi \times 432 \text{ Cal/g} \times 2.3 \text{ g/cm}^3}$$

$$\frac{dr}{dt} = \frac{3.54 \times 10^{-5} Q (\Delta T)}{r^2}$$

Determine maximum growth rate assuming:

$$\Delta T \approx 1000^\circ\text{C} \text{ at } 100 \text{ l/min (Figure 38)}$$

$$Q = 100 \text{ liter/min}$$

$$r = 4 \text{ cm}$$

$$\frac{dr}{dt} = \frac{3.5}{16} = .218 \text{ cm/min}$$

The preceding derivation and example shows that the maximum growth rate is dependent on the helium flow rate. To maintain growth rate constant, the helium flow must be increased as a function of  $r^2$ .

There is no theoretical maximum growth rate based on heat flow considerations. Growth rate is limited by the practical consideration of how large a gradient can be applied to the solid.

TABLE V. IDENTIFICATION OF SYMBOLS

---

L	= latent heat of fusion - 432 Cal/g
T	= temperature
$K_l$	= thermal conductivity of the liquid
$dT/dr_l$	= thermal gradient in the liquid at some point $r_l$ close to the interface
$A_l$	= $2\pi r^2$ = area of the isotherm which goes through $r_l$ - assume = to areas of interface
$k_s$	= thermal conductivity of the solid
$dT/dr_s$	= thermal gradient in the solid near the interface
$A_s$	= $2\pi r^2$ = area of the interface
$\rho_s$	= density of the solid at M.P. 2.3 g/cm <sup>2</sup>
$dr/dt$	= radial growth rate
m	= $2/3\pi r^3 \rho_s$
$dm/dt$	= mass freezing per unit time = $2\pi r^2 \rho_s \frac{dr}{dt}$
C	= Specific heat of helium 1.252 Cal/g°C (density of helium 0.1769 g/liter)
∴ C	= .2215 Cal/liter °C
Q	= Flow rate - liter/min

---

## 1.6 SOURCE OF FORMATION OF SILICON CARBIDE - EXPERIMENTAL

In the thermodynamic analysis (Appendix B) it was shown that the most likely source of SiC formation is from reaction



The CO is evolved from reaction of silica crucible with graphite retainers:

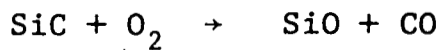


In run 106-C (Appendix A) a graphite piece was sandwiched between two pieces of single crystal silicon with polycrystalline silicon around them. The furnace was heated to close to the melting point of silicon and cooled. It was found that a silicon carbide layer was formed in areas where the graphite was in contact with silicon crystals and also a light layer in the immediate vicinity. The pieces of polycrystalline silicon far removed from the graphite piece did not show any evidence of SiC. In this experiment the graphite piece was not in contact with silica; hence, reaction evolving CO are suppressed. Consequently the polycrystalline silicon pieces were not coated with silicon carbide.

During recent runs the use of graphite retainers has been eliminated. A visual examination of the ingots cast shows a bright appearance in contrast to a layer of dull, yellow silicon carbide layer seen when graphite retainers were in contact with the silica crucibles.

Another possible source of CO formation is the oxidation of

the graphite furnace parts. These parts have been coated with a layer of silicon carbide with use. It has been observed that when poorer vacuum is achieved because of a leak, silicon carbide is formed on the ingot, probably from:



However, in the runs with vacuum-tight, 0.1 Torr, operation and absence of graphite retainers, no silicon carbide layer is seen.

## 2. SILICON CRYSTAL SLICING

### 2.1 ABSTRACT

A silicon crystal slicing project was undertaken to achieve the following goals:

Slice Specifications: Thickness - 0.015 cm

Size - 10 cm diameter or  
up to 10 cm x 15 cm

Accuracy - bow and taper  
<0.0025 cm;  
surface roughness  
<5 micrometers

Slicing Rate: 0.025 cm/minute (per wire/blade)  
for 10 cm kerf length

Kerf Length: 15 cm

Wire/Blade Thickness: 0.0075 cm wire/0.01 cm blade

Parallel Slices: 100

To accomplish these goals, a machine development, blade development, and ingot slicing program was undertaken. A multi-blade wafering machine was used to slice silicon ingots using wire with fixed diamond abrasive as the cutting tool.

A Varian 686 wafering machine was modified by installing a sensitive feed mechanism which incorporated a crystal rocking mechanism. In addition, a system for supporting

and guiding the wires was designed and installed.

For blade development all efforts were concentrated on impregnating or plating wire with diamond. Diamond electro-plated blades were developed using tungsten and stainless steel as a core. Wires electroplated with diamond had a very good life and did not fail due to diamond pull-out as was the case for impregnated blades. However, kerf width could not be reduced below 0.225 mm because diamond below 30  $\mu\text{m}$  could not be electroplated onto the wire. Kerf loss was reduced to 0.125 mm with impregnated wires. By plating after impregnation, the life and cutting effectiveness of the wires was greatly increased.

Slicing tests were performed on 4 cm silicon cubes and 7.6 cm diameter rods. Twenty-five wafers per cm (0.1 mm thick) were sliced from 4 cm cubes, and 0.25 mm kerf was consumed and yields ranged from 85 to 98%. Also, 7.6 cm diameter rods were cut into 0.1 mm thick, 25 wafers per cm. A yield of 50%, 50 wafers out of 100, was achieved for the 7.6 cm rods.

Surface roughness of the wafers was approximately  $\pm 0.5 \mu\text{m}$  and subsurface damage was 3 to 5  $\mu\text{m}$ .

The potential for efficiently slicing silicon with fixed diamond wire was established during this two-year effort. Thin wafers less than 0.1 mm were sliced with this method without breakage, to produce 25 wafers per cm with 3 to 5  $\mu\text{m}$  of damage.

It was demonstrated that the expendable material cost is low since only a small amount of diamond is plated on the wire and the wires can be used for many runs. To achieve good

slicing it was necessary to increase the local cutting force by rocking the work to minimize the contact length. In addition, the wires had to be guided with support rollers to minimize wander.

Slicing tests verified that impregnated wires fail due to diamond pull-out. This was minimized by nickel plating diamond impregnated wire. Electro-nickel plating diamond directly on the wires was also effective, but the kerf width could not be reduced below 9 mils as it can be for impregnated wire. Impregnated wires have the advantage that the diamond size concentration and distribution can be controlled better than for wires electro-plated with nickel and diamond. Plating after impregnation holds the most promise for reducing the kerf loss and therefore this effort is being accelerated.

Tungsten core wire was the best tested because of its high elastic modulus ( $50 \times 10^6$ ), its high elastic limit (250 KSI), and its resistance to hydrogen embrittlement during plating. Copper coatings were most desirable for impregnation since they were softest. In addition, the copper coating protected the tungsten core from corrosion.

## 2.2 INTRODUCTION

For ingot casting to be economically effective, slicing must be upgraded to slice larger ingots thinner with less kerf loss.

Crystal Systems has developed a blade abrasive system and modified a multi-blade wafer machine to cut hard materials.

Abrasive particles held in place on the cutting edge greatly improved cutting speed over free abrasive slurries for hard materials.<sup>41</sup> However, for fixed abrasives cutting rate becomes heavily dependent on the pressure of the cutting edge against the work. Cutting pressures can be increased by increasing the force on the blades against the work and/or by using thinner blades. Both methods result in blade wander. Cutting pressure was effectively increased by rocking the work to decrease the blade contact length; this minimized blade wander.

Crystal Systems has developed a blade charging process where the abrasive is impregnated into the cutting edge of the blade just as laps are charged for polishing or grinding.

For slicing with fixed diamond abrasive, wire was chosen as a substrate since it has the following advantages over flat blades:

- (i) Wires do not buckle with increase in feed force. Increase in feed force may increase rather than decrease stability.
- (ii) Wires do not torque the wafers. Therefore, thinner

wafers can be sliced with little surface damage.

- (iii) Wires can be pre-tensioned to higher stresses than flat blades, due to a symmetrical stress field.
- (iv) Wires may be more economical than blades since they are easy to fabricate and less metal is required.
- (v) Lower clamp pre-tension force can be applied to wire than blades due to its lower cross-sectional area. Therefore, a lighter blade carriage can be used and much higher speeds can be achieved.

## 2.3 MACHINE DEVELOPMENT

Initial emphasis was to modify the Varian 686 slicing machine for slicing silicon with wire. The original feed mechanism was replaced with a feed mechanism that was more sensitive to feed force. Besides being responsive to lower forces, the new feed mechanism has the following advantages:

- (i) The feed force can be controlled and resolved to within 0.01 lb/wire (4.5 g/wire) for 25 wires or 0.0025 lb/wire (1.1 g/wire) for 100 wires.
- (ii) Motion of the workpiece is incorporated in the feed mechanism so the workpiece motion could be coordinated with the motion of the blade carriage if desired.

By control of wire tension, feed force, and workpiece motion, a radial cut profile can be achieved to minimize the contact length between the wire and the workpiece. By minimizing the contact length, high cutting pressure can be achieved with light feed force.

Slicing tests at Crystal Systems have shown that for fixed abrasives, the cutting rate is heavily dependent on the pressure of the fixed diamond cutting edge against the work.

Wander of the cut was one of the factors that was limiting the slicing yield. Up to 10 mil, 0.25 mm per inch taper was experienced. Wander was caused by various factors such as (i) low wire tension, (ii) non-uniform distribution of diamond on the cutting edge, (iii) poor machine alignment, (iv) loading of the cutting edge with swarf, and (v) inadequate wire guidance and support.

For typical wire blade slicing operations support rollers are located on either side of the work. This supports the wire so that high feed forces can be used with no breakage and with greatly reduced wander.

A system using grooved rollers was installed to guide and support the wires.

With rollers supporting the wire on either side of the workpiece, much larger forces could be applied without breaking the wires. This support may be necessary when larger forces are applied for slicing larger cross-sectional area with thinner wires or blades.

Initially the workpiece was rocked synchronously with the bladehead. This caused considerable bouncing and poor cut quality.

Nonsynchronous rocking was achieved by driving the rocking mechanism with a 6 RPM electric motor using a crank. The crank did not produce a radial cut profile due to the sinusoidal crank motion that lags at the end of the stroke and is rapid at mid-stroke. A reversing linear drive was installed to drive the rocking mechanism and produce a linear motion over the entire stroke.

## 2.4 BLADE DEVELOPMENT

### 2.4.1 Introduction

Blade development efforts were restricted to wire rather than flat blades, since wires do not buckle and torque wafers with increase in feed force, allowing the slicing of thinner wafers with minimum surface damage. In addition, wires can be tensioned to higher stress than flat blades with less force because of the lower cross-sectional area. This allows for higher blade packing and higher speeds. Only impregnated wires were available at the start of this contract. These wires failed due to diamond pull out. Electroplated diamond wire blades were developed to cut effectively with minimum diamond pull out or diamond breakdown.

For the electroplated wires, the diamond particle size could not be reduced below 30  $\mu\text{m}$  because smaller diamond did not remain uniformly suspended in the plating solution. Therefore, kerf loss was not reduced below 9 mils, 0.225 mm. Kerf was reduced by using impregnated wire plated after impregnation to minimize diamond pull-out.

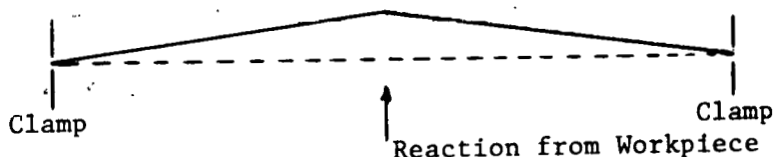
To slice thin wafers, wire wander was minimized by using guides. In addition, tensioning the wires to high stress and using wires with high elastic modulus minimized wander. Tungsten had the best mechanical properties of the wires tested and was used for most of the slicing tests.

Wire blade development efforts were concentrated in three areas:

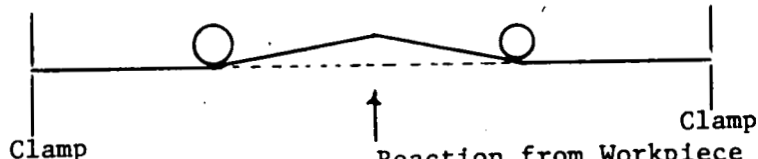
- (i) Mechanical properties of core wire
- (ii) Impregnating copper coated wire with diamond
- (iii) Electrolytically nickel plating diamond onto the wire core

#### 2.4.2 Mechanical Properties of Core Wire

It is desirable to utilize wire which has a high elastic limit and Young's modulus and use guide rollers to minimize wander. A diagram is presented below to demonstrate the deflection that will result with and without guide rollers.



(a) Without guide rollers



(b) With guide rollers

During slicing the forces on the wire are due to pretensioning of the blade pack and reaction of the feed force. These forces are mutually orthogonal. The force diagram can be represented as follows:



Therefore,  $\vec{F} = \vec{F_T} + \vec{F_F}$

$$|\vec{F}| = \sqrt{|\vec{F_T}|^2 + |\vec{F_F}|^2}$$

Initial length of wire,  $L_0 = 16$  in.

Diameter of wire core = 0.005 in.

$$\therefore \text{Cross-sectional area of wire core, } A = \frac{\pi (0.005)^2}{4}$$

$$= 1.96 \times 10^{-5} \text{ sq. in.}$$

It is shown in Appendix C that a force of 0.1 lb, 45 gms causes the 5 mil (0.125 mm) tungsten core to deflect 2.8 mils as compared to 3.5 mils for high strength steel music wire. This analysis shows that the tungsten, because of its higher modulus, will be more effective in resisting wander.

A typical stress strain curve for tungsten is presented in Figure 37. The tensile results expressed in terms of elastic limit 0.2% yield and ultimate engineering strength are summarized in Appendix D. The wires can be tensioned 80% of the yield strength and still remain below the elastic limit. One of the

potential problems that is not apparent from the tensile data is the effect of corrosion at the clamp. During nickel plating the wires are heavily etched to remove contamination. The etchant could not be thoroughly cleaned out of the clamp and therefore corrosion can cause the wire to fail at the clamp.

Embrittlement due to corrosion attachment or hydrogen was experienced in some plated wires. Stainless steel wires electroplated by one vendor failed in a brittle fashion during the first tests, but were not embrittled when electroplated by another vendor.

Tungsten wires that were nickel plated after cleaning with a caustic solution show improved yield strength, but were embrittled when cleaned with acids. Tungsten wire is not susceptible to hydrogen embrittlement as is the case for stainless steel,<sup>34</sup> but is subject to grain boundary attack by acids at elevated temperature.<sup>35</sup>

Wire cleaning and plating must be monitored very closely to minimize hydrogen and corrosive embrittlement, especially for ferrous wires.

Tungsten wires were nickel-plated and copper-plated with a 0.7 mil (17.5  $\mu\text{m}$ ) sheath for impregnation. In both cases, caustic cleaning procedures were used to avoid embrittlement. The corrosion was minimized even in the clamps, since the wire was protected by the nickel or copper sheath.

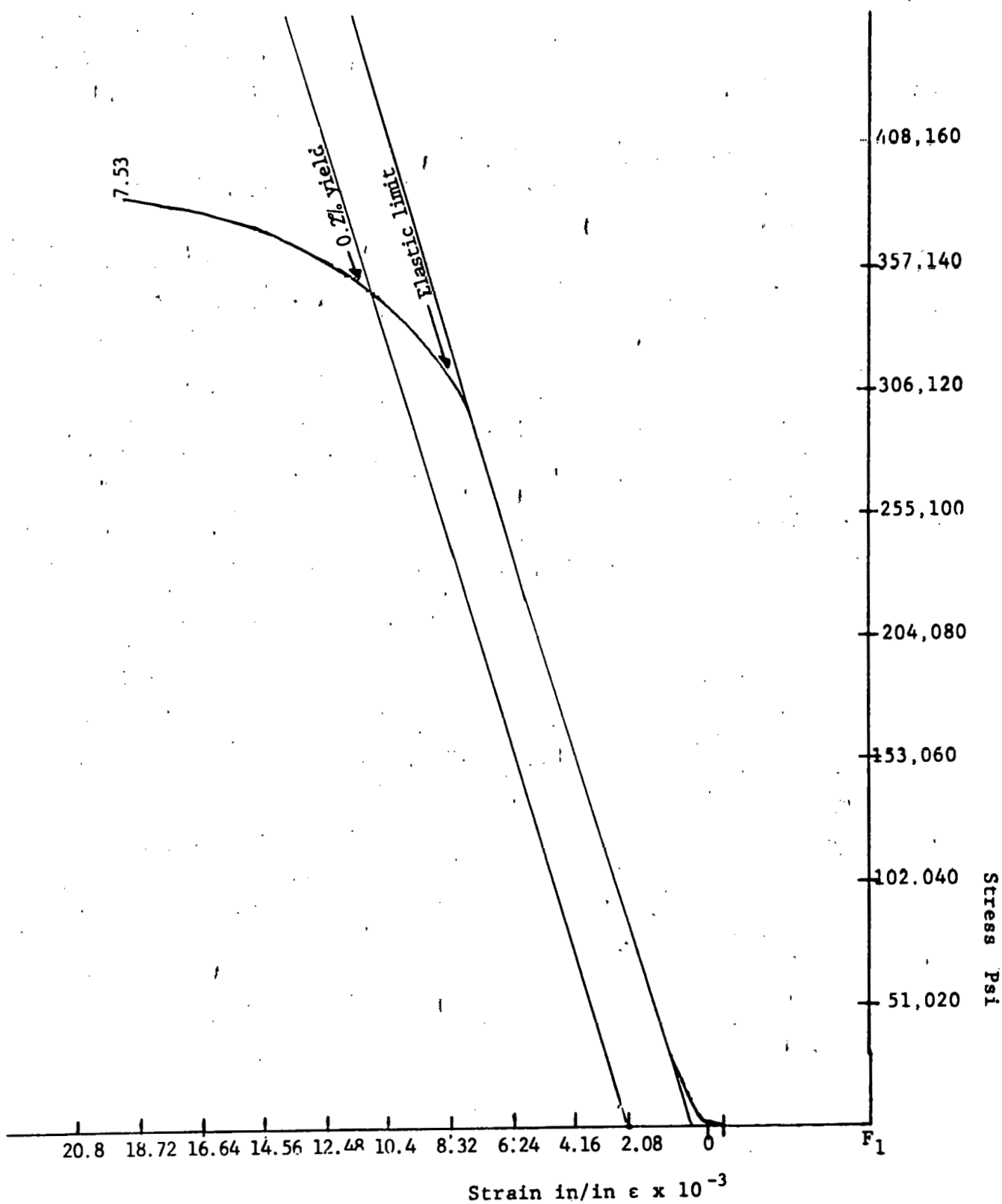


Figure 37. Engineering Stress Strain Curve for Plain Tungsten Wire

For good impregnation, the hardness of the coating should be low. The hardness of copper and nickel in the as-plated condition and of nickel plating in the annealed condition was measured and is presented in Table VI. This annealing treatment caused the 0.2% yield strength of the tungsten core to decrease from 340 KSI to 290 KSI, as can be seen in Appendix D. Copper is the softest coating even without annealing and therefore the first choice for impregnation.

Table VI. Hardness of Various Components of Wires  
Measured on a Leitz Microhardness Tester  
with a Knoop Diamond Point and Using a  
50 gram Load

Wire	Hardness	
Nickel plate on "as received" wire	482	(42 R <sub>C</sub> )
Nickel plate on "annealed" wire	347	(34 R <sub>C</sub> )
Tungsten core on "as received" wire	968	(72 R <sub>C</sub> )
Copper coating on stainless steel wire	142	(10 R <sub>C</sub> )
Steel core in stainless steel wire	801	(63 R <sub>C</sub> )

In summary, tungsten wire is the best tested to date because of its high elastic modulus ( $50 \times 10^6$ ), its high elastic limit (250 KSI), and its resistance to hydrogen embrittlement during plating. Copper coatings are most desirable for impregnation since they are soft; in addition, the copper coating protects the tungsten core from corrosion.

#### 2.4.3 Impregnated Wire

Initial slicing was performed with commercially available\* diamond impregnated wire with the following specifications:

<u>Diamond Impregnated Wires Carried in Stock</u>	<u>Diamond Size in Microns</u>
0.005 super wire	20
0.008 stainless steel and super wire	45

Almost all the wire that was tested was 5 mil (0.125 mm) high tensile strength stainless with a 1.5 mil (0.0375 mm) thick electrolytic copper sheath for holding 45 micron natural diamond. Severe wander was encountered in the one case where diamonds were impregnated into soft 8 mil (0.2 mm) stainless steel wire. The stainless wire was soft to allow for impregnation and therefore had a low yield strength which prevented proper tensioning.

---

\*Laser Technology, Inc., 10624 Ventura Blvd., No. Hollywood, CA 91604

Considerable variation in diamond concentration was experienced from lot to lot. Figure 38 is an SEM photograph at high and low magnification of two different lots of impregnated wire. Notice the low diamond concentration on the wires from lot 2 as compared with those from lot 3. Some diamonds were fractured during impregnation as can be seen in the highly magnified diamond particles of lot 3. Pronounced blade wander occurred when diamond concentration was as low and non-uniform as is shown for lot 2 in Figure 38. In order to increase the diamond concentration, the wire was impregnated twice. Figure 39 shows that the diamond concentration has been increased but the copper sheath is severely abraded by double impregnation prior to slicing silicon.

All impregnated wires failed due to diamond pull-out after slicing through a 4 cm cubic workpiece.

Diamond pull-out is illustrated in Figure 40 for an impregnated wire that cut through one 4 cm silicon cube at a feed force of approximately 0.15 lb per wire, a force that did not cause any pull-out in electroplated wire.

Pull-out was minimized by nickel plating after impregnation.

An effort was initiated to plate the impregnated wire by electro- as well as by an electroless plating process. Both of the methods were used to plate three thicknesses; viz, 0.1 mil, 0.3 mil, and 0.6 mil on commercial as well as Crystal Systems impregnated wires where diamonds are impregnated only on the cutting edge. The electroless plated wires were heated to 175°C,

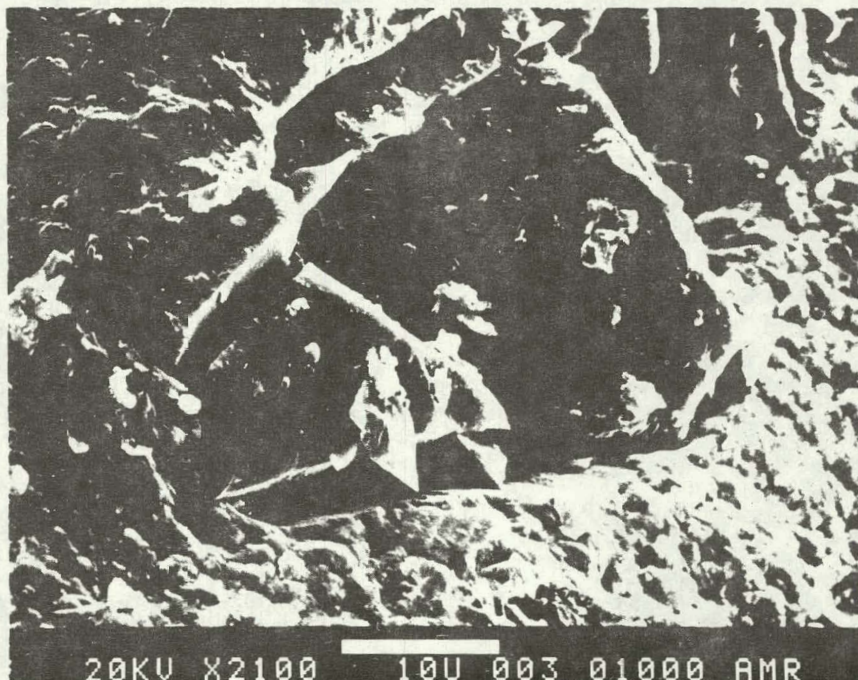
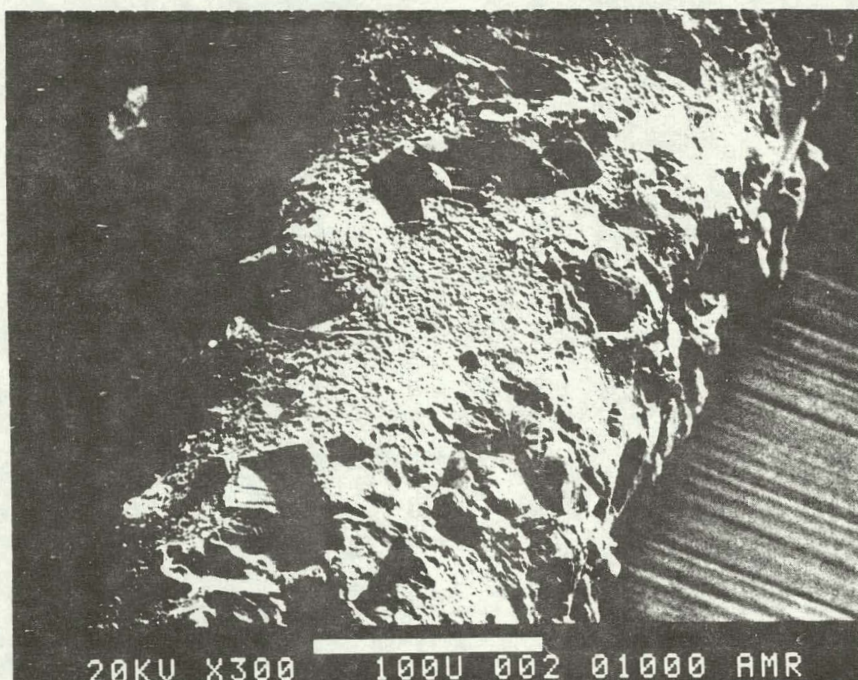
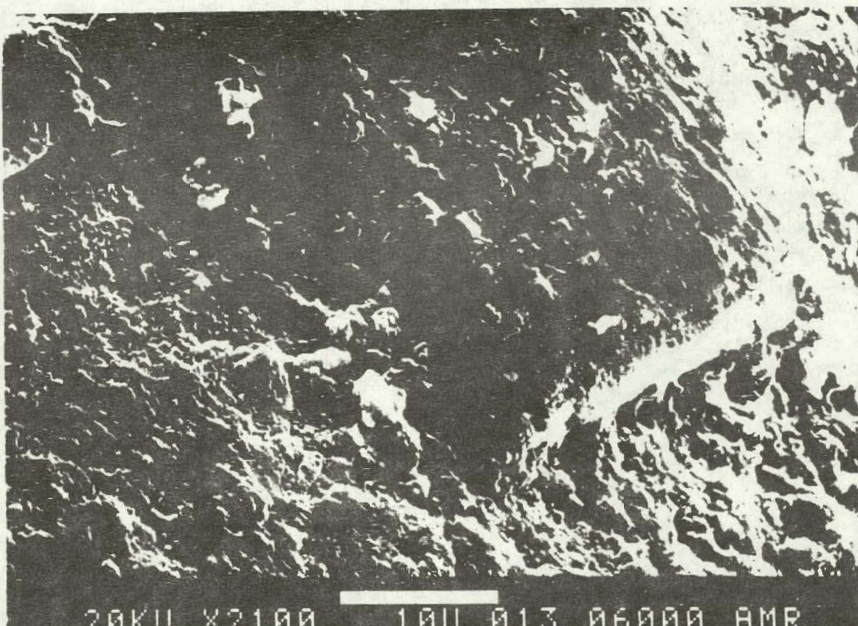
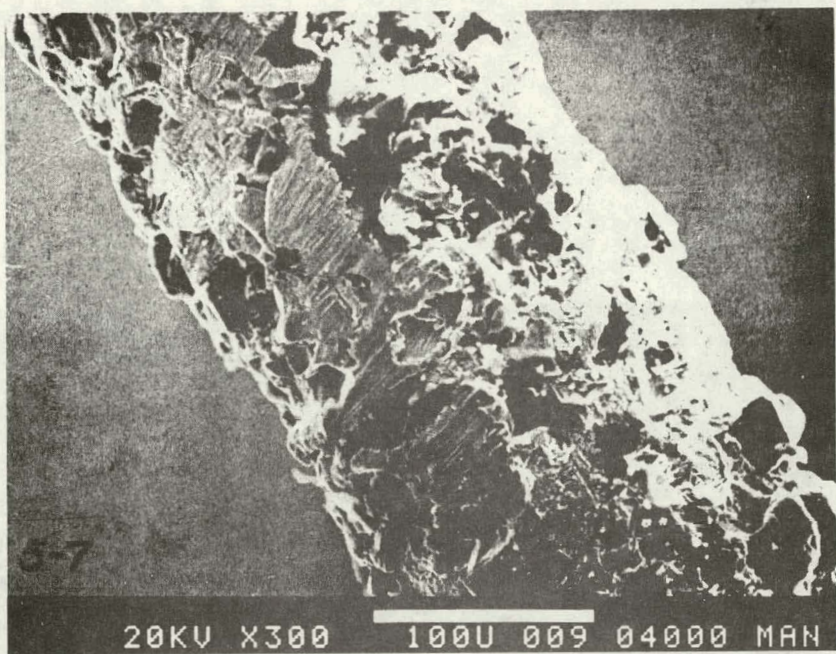


Figure 38 SEM of 8 mil Copper Sheathed Stainless Steel Wire Impregnated with 45  $\mu$ m Diamond. (Top) Lot #2, Used. (Bottom) Lot #3, Unused



20KV X300 100U 009 04000 MAN



20KV X2090 10U 010 04000 MAN

**Figure 39.** SEM of 8 mil, Copper Sheathed Stainless Steel Wire Double Impregnated with 45  $\mu$ m Diamonds.

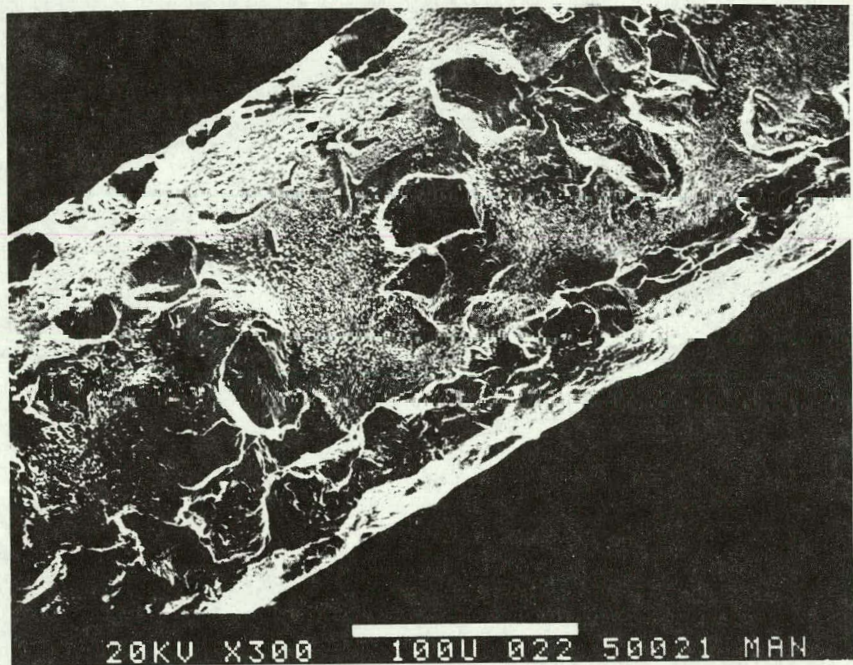


Figure 40. SEM of Diamond Impregnated Wire  
Used in Run 42-S Showing Diamond Pull-out.

230°C, and 290°C to study the effect of heat treatment. The samples were examined with a SEM. Details of the wires are shown in Table VII. It was found that both the commercial and Crystal Systems wires could be cleaned and plated with no difficulty. The electroless plating contracts when heated, thereby holding the diamonds more firmly. The 0.6 mil thickness plating showed signs of cracking due to densification during heat treatment. A 0.3 mil thick nickel plating was enough to hold the diamonds (Figure 41). Note the nickel coat on the cross-sectional view. A SEM of the same wire used to cut through three 4-cm cubes is shown in Figure 41. The only significant difference between the used and new wire is some abrasion of the nickel coating. There does not appear to be significant pull-out.

The development of impregnation/plating method can be utilized for reducing kerf losses. Diamonds can be impregnated only in the cutting edge by the Crystal Systems process, thereby reducing costs further.

In summary, diamond impregnated wires fail due to pull-out. Pull-out can be prevented by plating after impregnation. Impregnated wires have the advantage that the diamond size concentration and distribution can be controlled better than for wires electroplated with nickel and diamond. Plating after impregnation holds the most promise for reducing the kerf loss and therefore this effort is being accelerated.

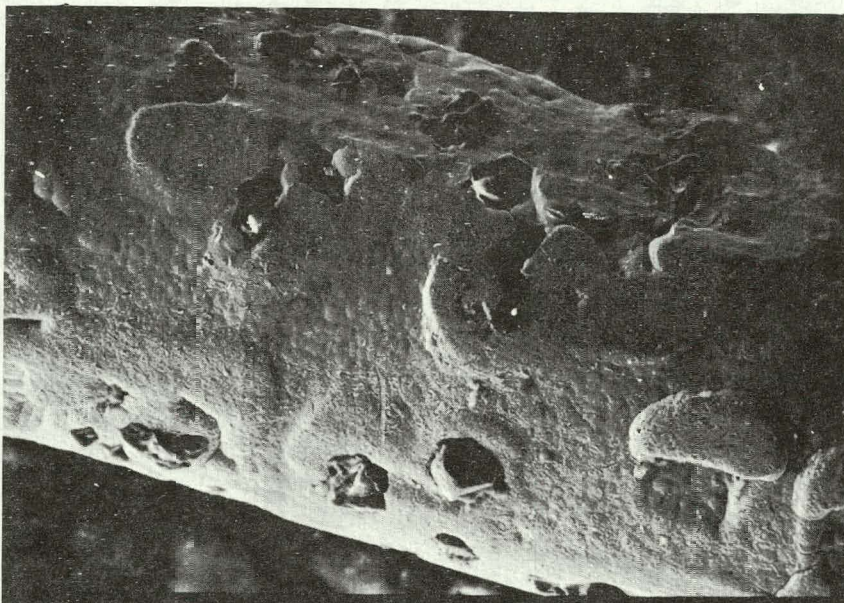
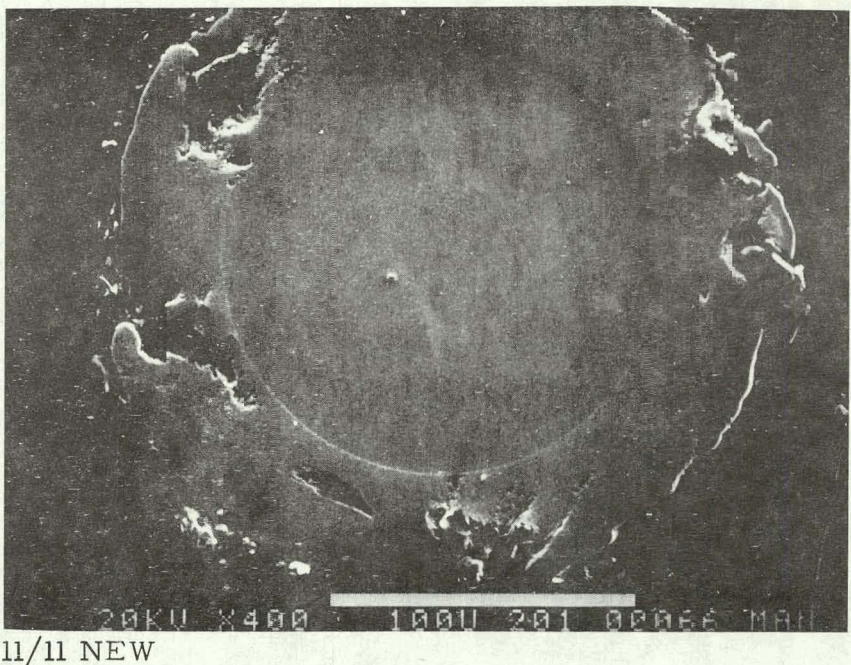
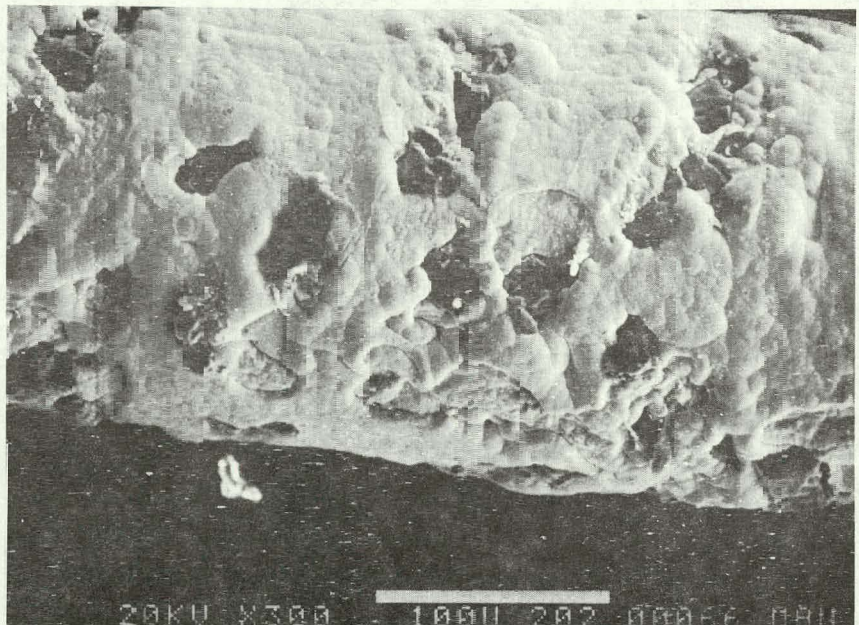


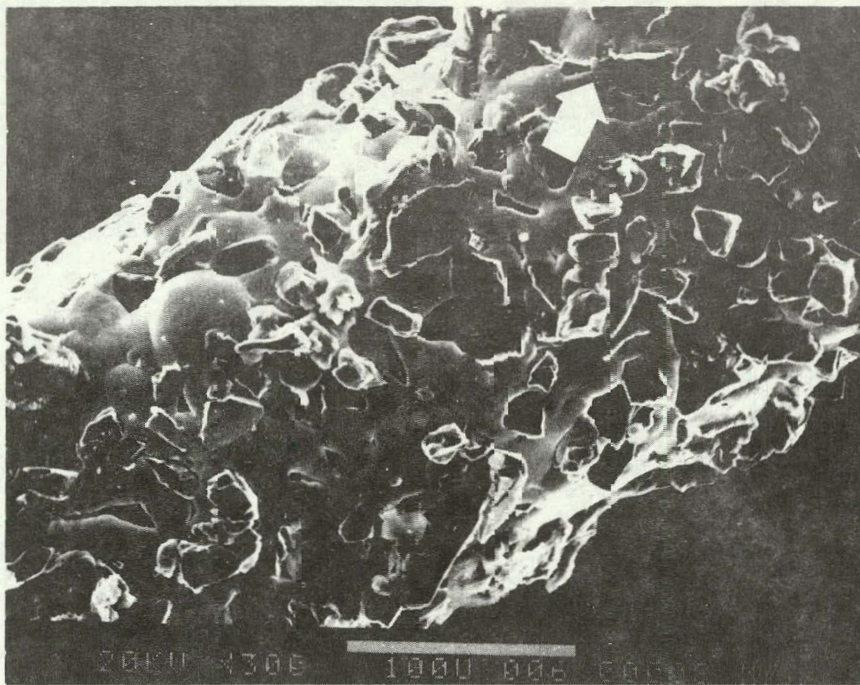
Figure 41. SEM of 8 mil Copper Sheathed Stainless Steel Wire Impregnated with 45  $\mu$ m Diamonds and Electroless Plated with 0.3 mil nickel. Top Shows Unused Wire, Bottom Picture Shows Wire Used through 12 cm of concrete.

TABLE VII . Details of Plating of Impregnated Wire

WIRE	PROCESS	HEAT TREATMENT TEMPERATURE °C	PLATING THICKNESS (mil)
Commercial	Electroless	-	0.1
Commercial	Electroless	-	0.3
Commercial	Electroless	-	0.6
Crystal Systems	Electroless	-	0.1
Commercial	Electroless	290°	0.1
Commercial	Electroless	290°	0.3
Commercial	Electroless	290°	0.6
Commercial	Electroplated	-	0.1
Commercial	Electroplated	-	0.3
Commercial	Electroplated	-	0.6
Crystal Systems	Electroplated	-	0.1

#### 2.4.4      Electroplated Wire

To eliminate diamond pull-out, electroplated wire blades were developed. Wires were fabricated by nickel plating diamonds with a proprietary process onto a 5 mil (0.125 mm) stainless or tungsten wire. Figure 42 is a SEM of the first wire blades that



74

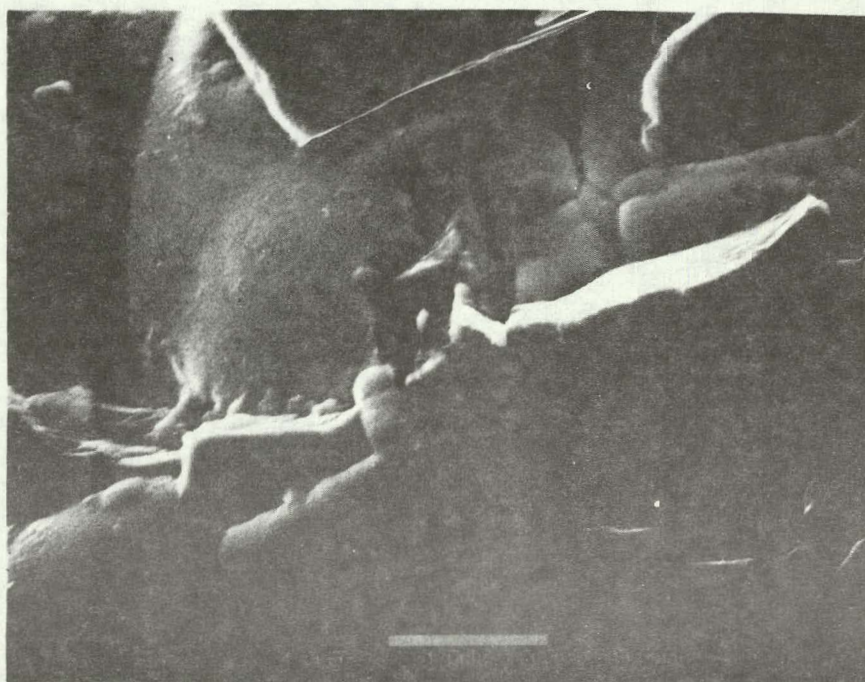


Figure 42. SEM of Tungsten Wire 5 mil, .127 mm Nickel Plated with 400 Mesh 37  $\mu\text{m}$  Diamonds (Unused)

were fabricated. The blades were fabricated with this process by nickel plating 400 mesh, 37  $\mu\text{m}$  diamonds onto a 5 mil, 0.13 mm stainless steel wire. Note the high concentration of diamonds in relation to the impregnated wire. Swarf removal was considered essential for this high diamond concentration. Swarf could easily fill in the small spacing between diamonds. In view of this, water with no additives was flushed over the work and out the drain. This prevented the possibility of swarf build-up that occurs in the coolant during recirculation.

At a feed force of 0.15 pounds, 68 gm per wire, cutting rates held in the vicinity of 3 mil/min, 0.075 mm/min, during much of the run, but wire breakage was a problem toward the end of the cut. This was apparently the result of hydrogen embrittlement during plating, related to the evolution of hydrogen.<sup>34</sup> The wires were not baked at 450°F as is a typical treatment for preventing hydrogen embrittlement in stainless plated products.<sup>36</sup>

A wire that had cut completely through the silicon block was examined with an SEM for signs of degradation. No signs of degradation can be observed.

Tungsten is not susceptible to hydrogen embrittlement<sup>35</sup> and has a high modulus of 50 million, high yield strength of 340,000 psi (Appendix D), and therefore it was selected as core material. Diamond, 400-mesh, 37  $\mu\text{m}$ , were electroplated on the wire with a nickel plating. Figure 43 is an SEM of wire

76

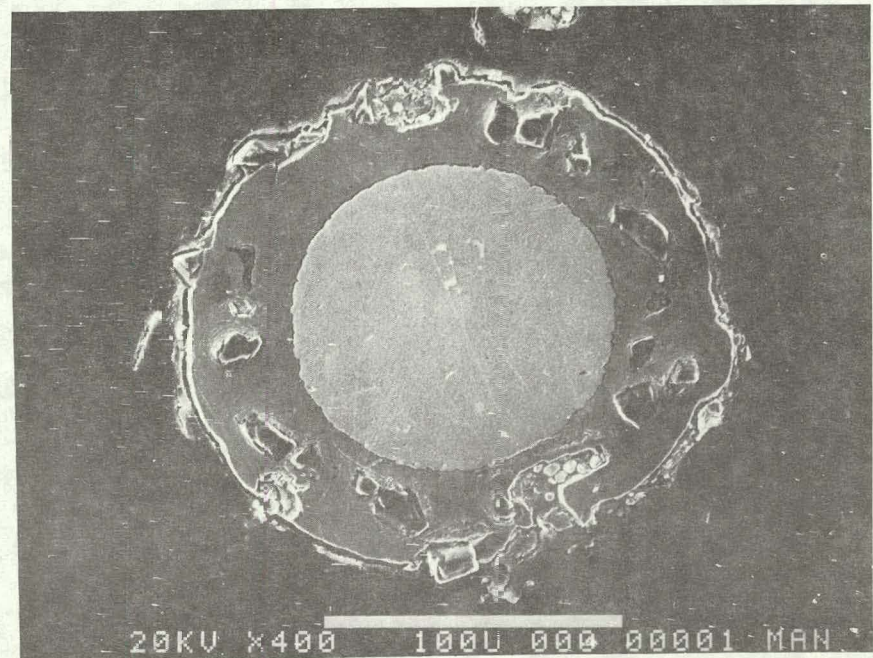
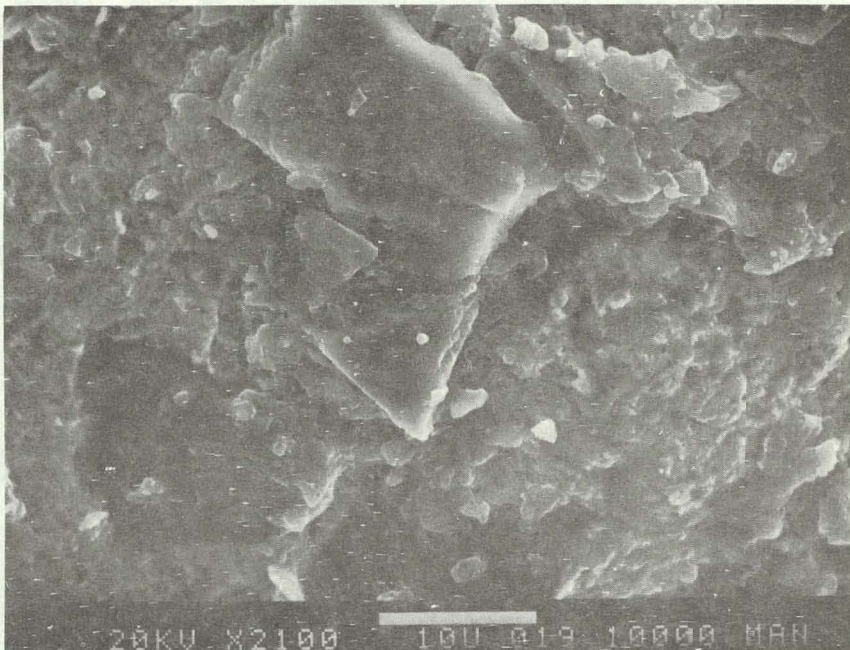
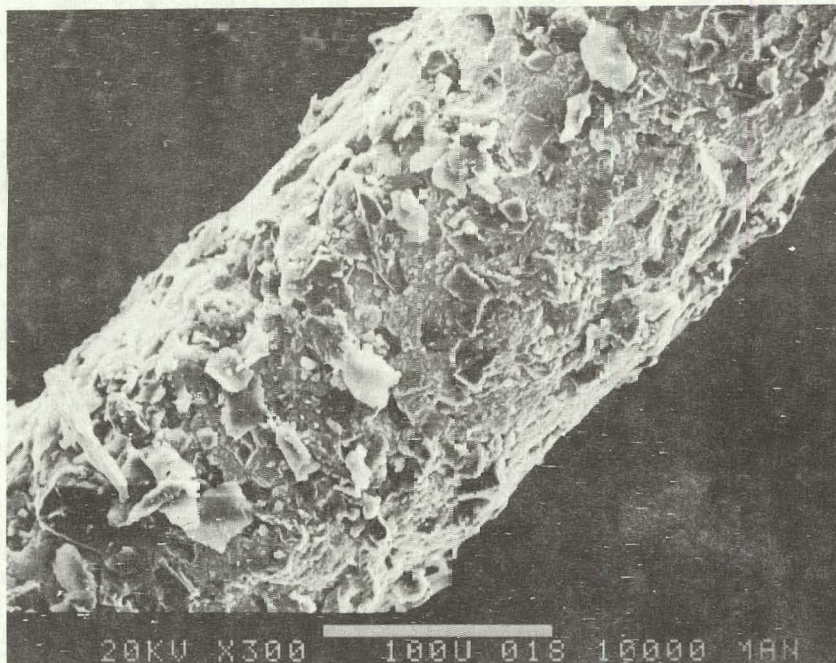


Figure 43. SEM of Tungsten Wire 5 mil, .127 mm Nickel Plated with 400-mesh 37  $\mu$ m Diamonds Used in Runs 18, 19, 20

used in three runs.

The diamond appears buried beneath the nickel plating in the unused wire and the concentration is much lower than for the diamond plated stainless steel wire.

No significant deterioration in performance or diamond pull out was observed in the tungsten plated wires even after slicing through 18 4-cm workpieces.

In an effort to reduce kerf the diamond particle size was decreased to 30  $\mu\text{m}$ . A high concentration of diamond was plated onto the surface but the plating thickness still was 2.5 mil; therefore, many diamonds were buried beneath the nickel coating.

Two attempts were made to electroplate 22  $\mu\text{m}$  diamonds on the tungsten wire, but in both attempts the concentration was very low. Apparently the surface area to volume ratio is unfavorable for electroplating. This is consistent with findings in the abrasive industry where bonded diamonds are not used below 45  $\mu\text{m}$ .<sup>37</sup>

In summary, tungsten wire electroplated with nickel to fix 45 and 30  $\mu\text{m}$  diamond particles in place performed very well. Minimum diamond pull-out was experienced with these electroplated wires. It appears that it will be difficult to reduce kerf below 8 mils with electroplated wires, since diamond particles below 30  $\mu\text{m}$  do not readily plate.

## 2.5 SLICING TEST

### 2.5.1 Introduction

Slicing tests were performed with a modified Varian 686 multi-blade wafering machine. Most of the testing was performed on 4 cm cubic workpieces using both diamond impregnated and plated wire as a cutting tool.

The slicing tests were conducted to determine the effect of feed force, surface speed, kerf length, rocking motion, and diamond tooling on cutting rate, wander, surface damage, and blade life.

Tests confirmed that cutting rate is heavily dependent on feed force and surface speed. Non-synchronous rocking of the workpiece was necessary to minimize kerf length and thereby achieve good cutting rates and surface quality. Wander was improved by an order of magnitude by using support rollers to guide the wires.

A summary of the silicon slicing tests is presented in Appendix E.

### 2.5.2 Slicing with Impregnated Blades

Typical cutting rates from run 2 are shown in Figure 44 for impregnated blades. This graph shows that the cutting rate was heavily dependent on feed force. For an increase in feed force from 67.5 to 96.5 g/blade, the cutting rate has nearly tripled.

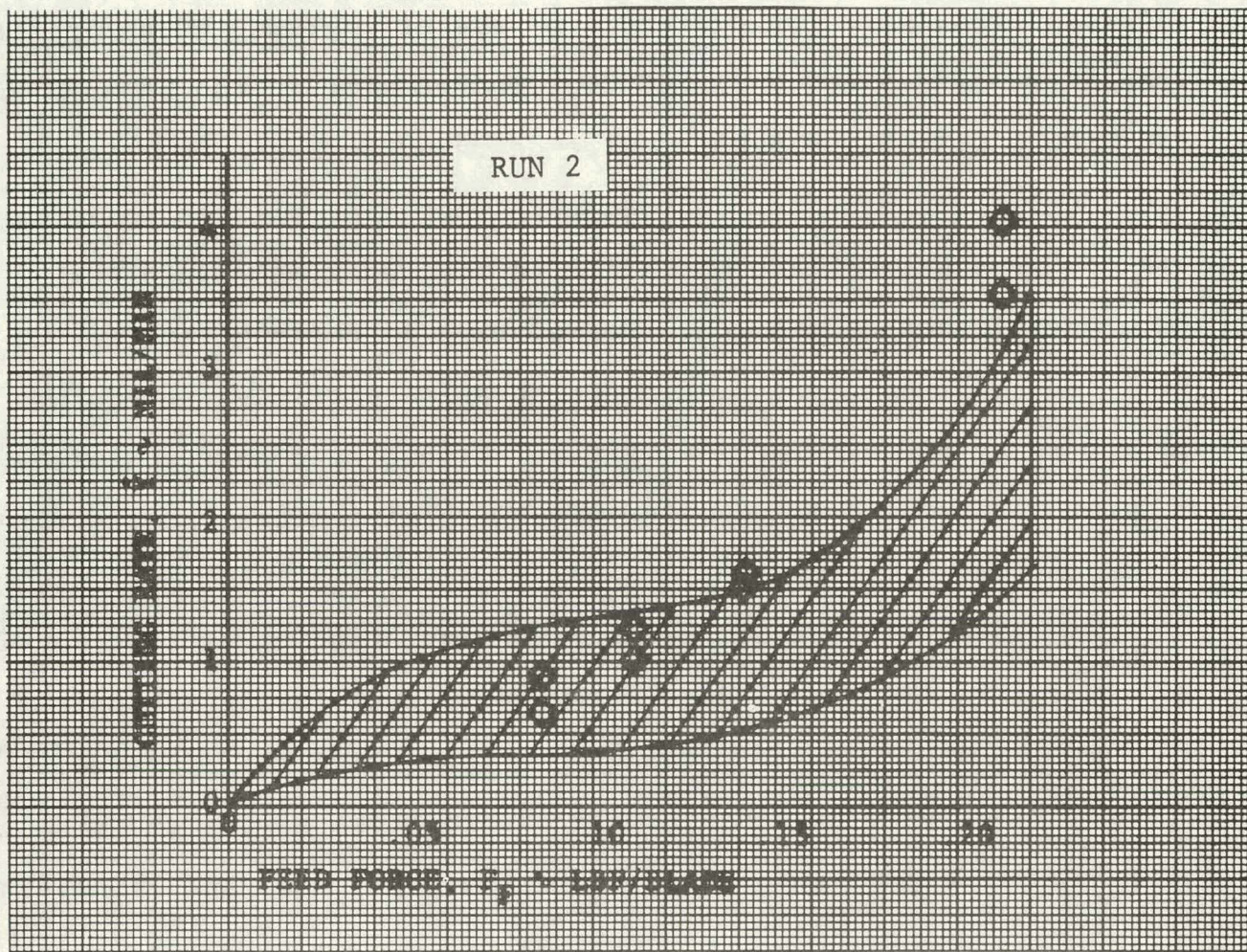
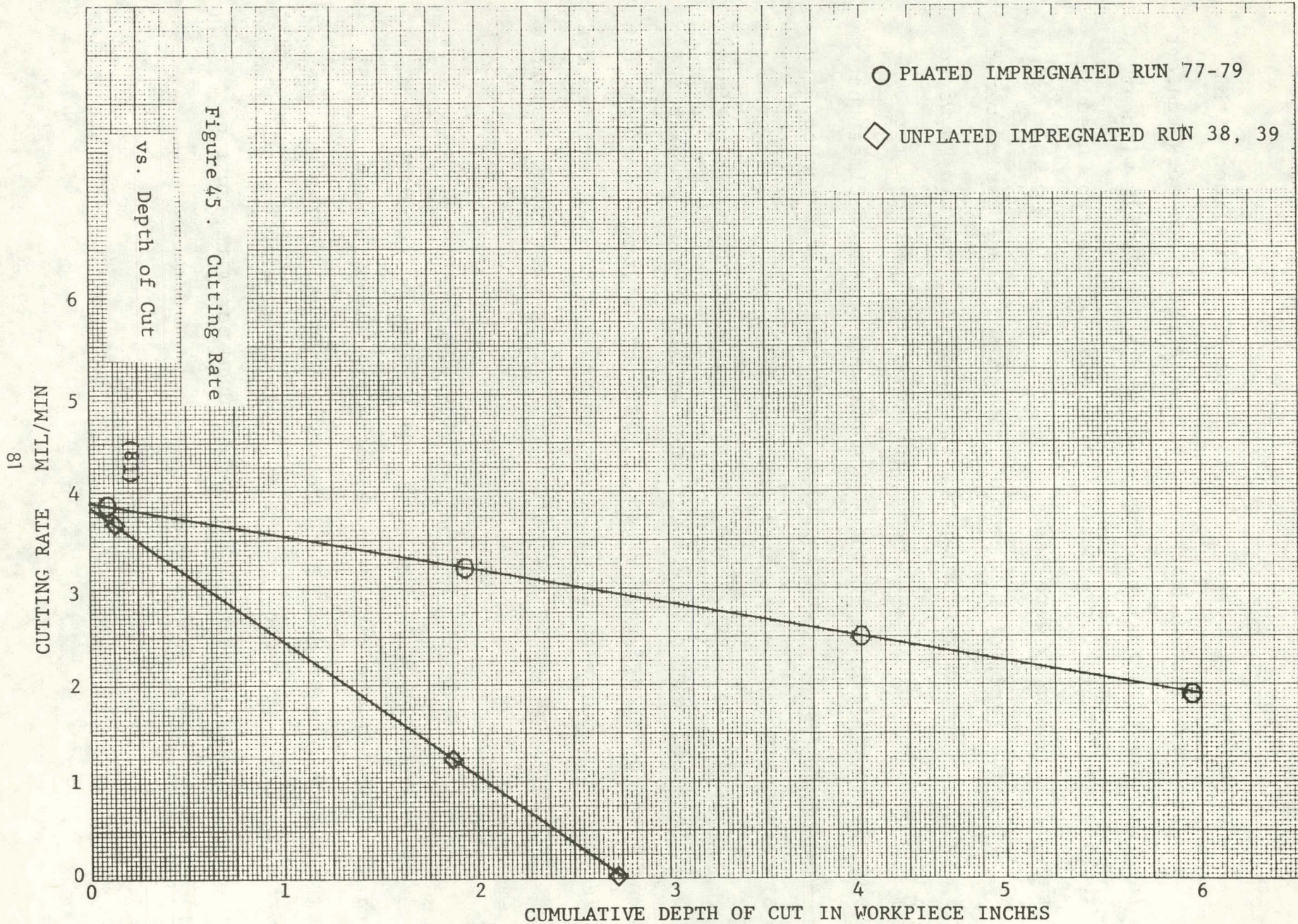


Figure 44. Feed Force Vs. Cutting Rate  
Surface Speed 140 ft/min

Runs 77-79 were carried out with impregnated wires (Figure 41) that were electroless plated with a 0.0075 mm, 0.3 mil nickel coating to hold the diamond particles in place. Figure 45 is included to compare the degradation rate of impregnated and plated wire in run 77-79 and unplated impregnated wire in run 38 and run 39. The unplated impregnated wire degraded to a zero cutting rate during run 39 after cutting 2.75 inches of silicon while the plated impregnated blade was still cutting at 2 mil/min after cutting 6 inches of silicon. Degradation in cutting rate was determined to be pull-out of diamond abrasive particles. This was confirmed by SEM examination (Figure 40) and by comparison with cutting performance of unplated wire with wire nickel plated after impregnation.

The effects of higher diamond concentration on cutting rate, abrasive life and wander were measured in run 7 using a double impregnated wire. After cutting more than twice the distance, cutting rates were at least comparable to those at the end of run 2B. Visual comparison of wafer surfaces from run 7 and 2 indicated a big improvement in surface quality.

It has been observed that impregnated wires fail due to diamond pull-out. This results in decreased cutting rates and blade wander. Wires that were double impregnated and wires that were plated after impregnation had a much longer life before cutting rates decreased.



### 2.5.3 Effect of Workpiece Motion

Run 16 was conducted to verify that silicon sliced with fixed abrasive must be rocked to minimize the blade work contact length. For this test the workpiece was held rigidly without rocking and double impregnated wire blades of the type used in runs 12, 13, and 15 were used.

A blade force of 0.3 pounds, 136 gm per blade was required in order to obtain cutting rates in the 2 to 3 mil/min, 0.05 to 0.075 mm/min range. This was twice the force required for comparable cutting rates in run 8 and one and one-half times that required in run 13, runs in which the workpiece was rocked with synchronous motion at a phase angle of 90°.

At this high feed force, cutting rates of 2 to 2.5 mil/min, 0.05 to 0.065 mm/min were maintained at first; then wires broke and cutting rates deteriorated to near zero at the end of the cut. In addition, wafer surfaces were very rough. Run 16 verified that silicon must be rocked for effective slicing with fixed diamond abrasive.

Run 17 was conducted to determine the effects of non-synchronous rocking of the workpiece on slicing performance. Blades were of the double impregnated type used in runs 12, 13, 15, and 16. Water was used as a coolant and the workpiece was rocked with a frequency of one-half cycle per minute.

At a feed force of 0.2 pounds, 90 gm per wire, cutting

rates were maintained in the range of 2 to 3 mil/min, 0.05 to 0.075 mm/min throughout the run.

The wafer surfaces generated in this run were dramatically smoother in appearance than wafer surfaces from previous tests, with virtually no waves, scoring, steps or other surface roughness.

The cut was made in one continuous operation with no shutdowns and startups. In addition, prior to the run, the feed mechanism was modified slightly in order to eliminate some of the play in rocking components.

The entire wafer surfaces from this run appeared of comparable quality to the very best smaller areas on wafers from earlier runs with synchronous rocking of the workpiece at a phase angle of 90°.

#### 2.5.4 Slicing with Diamond Plated Wire

Using impregnated blades it was established that cutting effectiveness decreased rapidly due to diamond pull. ID blades used in the semi-conductor industry have a very good life.<sup>38</sup> Typically wheels cut 2000 to 3000 2-inch diameter silicon slices. Diamond is held on the ID of these blades by nickel plating. In view of this, diamond plated wires were developed. The first diamond plated wire was used during run 14. These wires cut effectively at approximately 2 mil/min but could only be used for one run since they failed due to embrittlement.

For slicing runs 18 through 36 a wire pack with twenty-eight 5 mil (0.127 mm) diameter tungsten wires was used. Tungsten

was chosen as a core material because of its high modulus of 50 million and high strength of 400 thousand psi. Four hundred mesh diamonds were electroplated on the wire with a nickel plating.

Feed forces for all runs was 0.2 pounds (90 gm) per wire and slow non-synchronous rocking of the workpiece was used.

Average cutting rates for each run are presented in Figure 46. The average rates were calculated by dividing the depth of workpiece by the length of time required to cut through it. A cutting rate of over 6 mil/min (0.15 mm/min) was achieved for the first run 18-S until it cut into the glass mounting block. This is illustrated in Figure 47, a graph of Cutting Rate vs. Distance Cut.

The cutting rate remained below 2 mil/min (0.05 mm/min) for the next run 19-S. It was terminated after cutting 2 cm and the wire package was turned over. Cutting rates of about 6 mil/min (0.15 mm/min) were experienced until the wires cut into the glass. Soaking and cleaning the wires with methanol to remove swarf or the epoxy bond did not increase cutting rates above 2 mil/min (0.05 mm/min) that were achieved at the end of the previous run.

Light dressing with a soft  $\text{Al}_2\text{O}_3$  stick increased the rates to 2.75 mil/min (0.069 mm/min) for the remainder of the run.

A graphite mounting block was used rather than the glass. This did not degrade the performance of the wires after cutting into it.

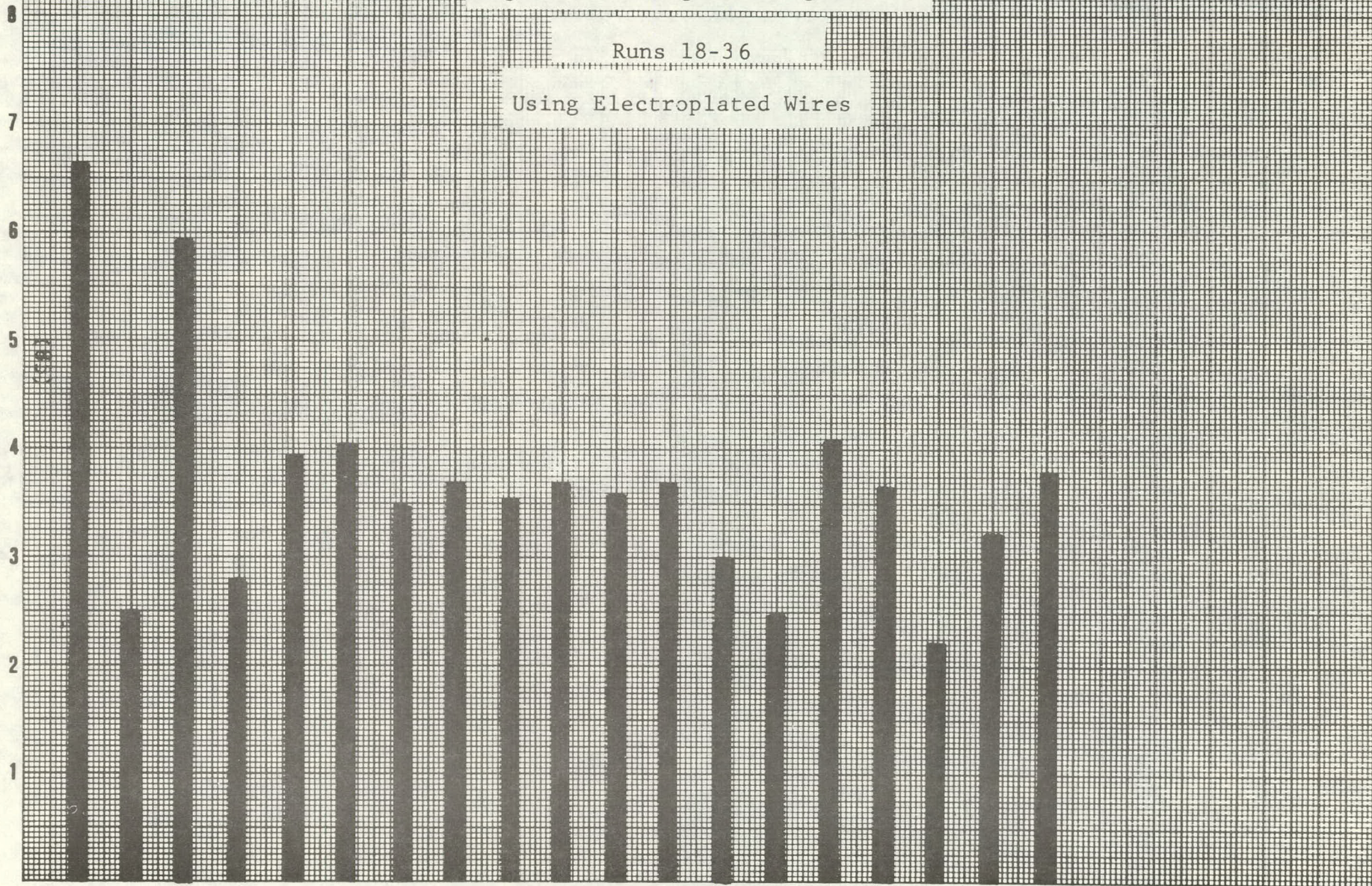
For the next run 20-S, no degradation in cutting rate was experienced. An average cutting rate of 3.9 mil/min, 01 mm/min was

Figure 46. Average Cutting Rates

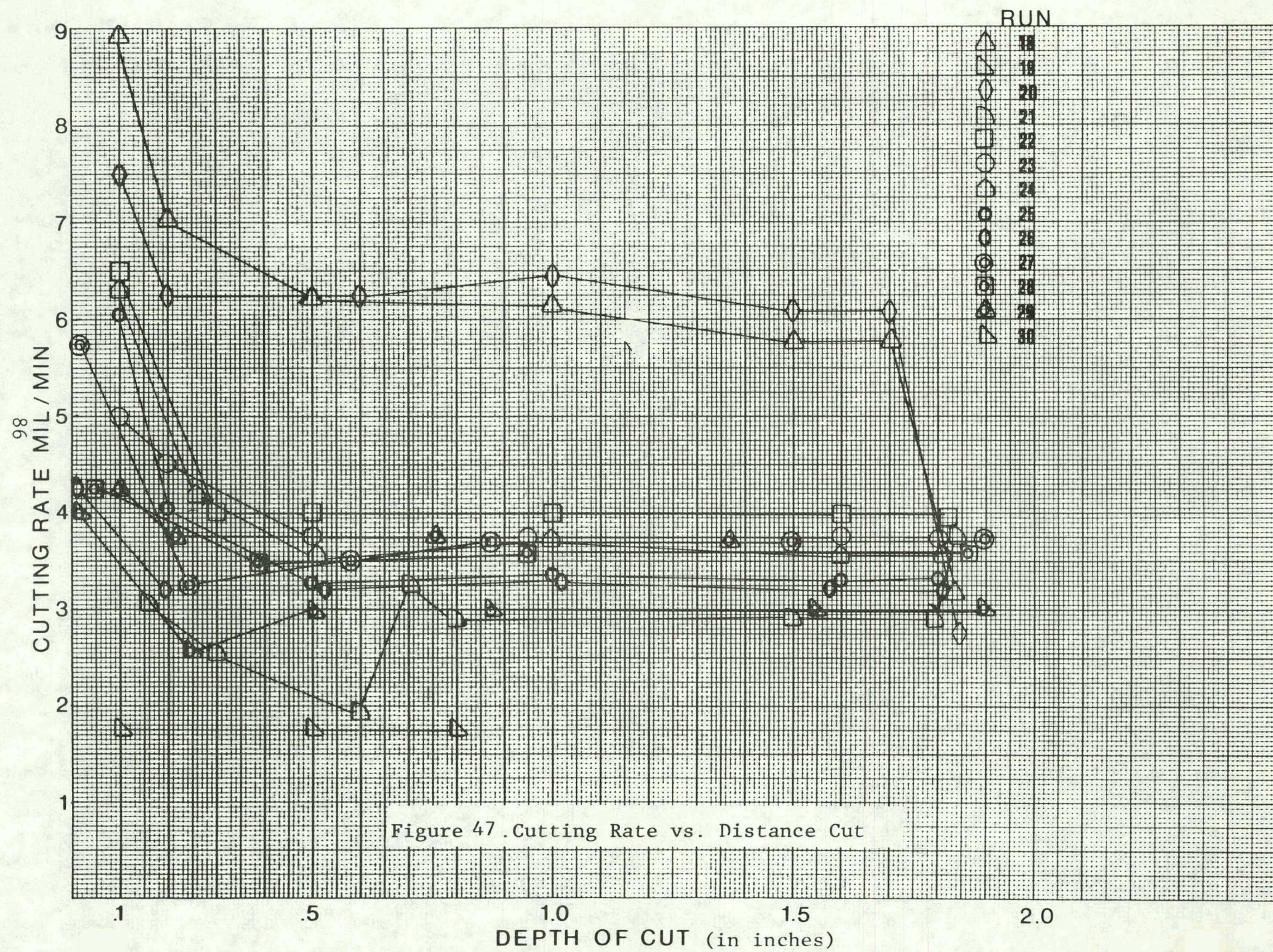
Runs 18-36

Using Electroplated Wires

CUTTING RATE MIL/MIN



RUN 18 19 20 21 22 23 24 25 26 27 28 29 30 31 32 33 34 35 36



in fact achieved after light dressing.

The glass mounting blocks that were used until this run appear to have degraded the performance and life of the wire after cutting into it.

After the graphite mounting block was used, cutting rates stabilized at approximately 3.5 mil/min (0.9 mm/min) through run 29-S. Wafer surface quality appeared to improve for each run. Sudden increase in feed force and machine stoppage caused localized roughness increases. The taper for the worst wafers was about 1 mil/in. (0.001 mm/cm). Kerf loss was approximately 9 mil (0.225 mm) for all wafers. Wafer-to-wafer thickness variation increased from run 18-S to 29-S. The wires were not precision spaced in the wire package and increasing variation in wafer thickness indicated a degradation of the grooves in the rollers.

Stiffening of the sensitive feed mechanism and modification of roller support system were successful as surface quality parallelism and wafer-to-wafer thickness variation in run 30-S show improvement.

Some of the noise suspected to be from the feed mechanism is in fact being transmitted through the roller support system due to acceleration of the bladehead. This condition may be minimized by altering roller support system, but this will be an inherent problem when reciprocating a massive bladehead.

For runs 31-S, 32-S, and 35-S, the speed of the non-synchronous rocking was varied from one-half to 50 cycles/min.

It was difficult to draw any conclusions from these tests since the run to run differences in cutting rates outweigh the effect of changes in rocking speed. For run 35-C, the rocking rate was changed during the run. It appeared that the cutting rate increased up to about 6 cycles per minute and held constant for further increases. More conclusive results will be obtained when the number of wires is increased, since this increases the sensitivity.

Runs 33-S and 34-S were conducted to determine the effect of bladehead speed on cutting rate and surface quality. For run 34-S the entire cut was made at 40 cycles/min, half the usual speed. Cutting rates of 2.2 mil/min (0.06 mm/min) were maintained throughout the run. There was no observable difference in surface quality over previous runs. For run 33-S, the cutting rate increased directly with the bladehead speed, as shown by other investigation for loose abrasive slicing.

Run 36-S was conducted to determine the effect of dry cutting. The dry cutting was aborted after cutting less than a mm, due to loading of the blade. The run was continued wet with an average cutting rate of 3.76 mil/min (0.1 mm/min) indicating that there was no damage to the wire from cutting dry.

After 18 runs with the same diamond-nickel-tungsten blade package, all producing the highest quality wafers obtained from the program to date, no significant deterioration of performance had been observed. No wires or wafers have broken throughout these

tests. If there was no mechanical failure of the wire, only degradation in cutting performance, the whole blade package could be turned over for further cutting.

Since cutting was so effective, i.e., good surface with very little wire wander, it was apparent that the spacing could be decreased to cut more wafers per unit length. For run 41-S wire was spaced at 15 mil (0.375 mm) intervals to produce 64 wafers per inch. None of the wires came together during the run. The wafers ranged from 5 to 7 mils (0.125 to 0.175 mm) thickness. Wafer roughness was measured with a Rank Tallysurf Profiliometer in the areas outlined on the tracing shown in Figure 48. The surfaces parallel to the wire direction 3 and 4 were smoother than the profile across from the cut 1, 2, and 5.

Life tests using the nickel-plated tungsten core wire were carried out in runs 51-S through 60-S and 62-S through 65-S. The as-received wires after plating measured about 10 mil (0.254 mm) each. The blade pack was used without any dressing before or in between runs. The average thickness of the wafer cut, calculated on the basis of a stack of 20 wafers, was 5.5 mil (0.140 mm) (run 51-S); 6.5 mil (0.165 mm) (run 55-S); and 7.25 mil (0.184 mm) (run 60-S). Initially the average cutting rates were 3.0 mil/min, (0.076 mm/min) for run 51-S at 38 gms feed force, but it dropped to 1.13 mil/min, 0.029 mm/min in run 60-S for a feed force of 25 gms. However, in run 57-S when the feed force was 38 gms better cutting rates were obtained. This again shows the strong effect

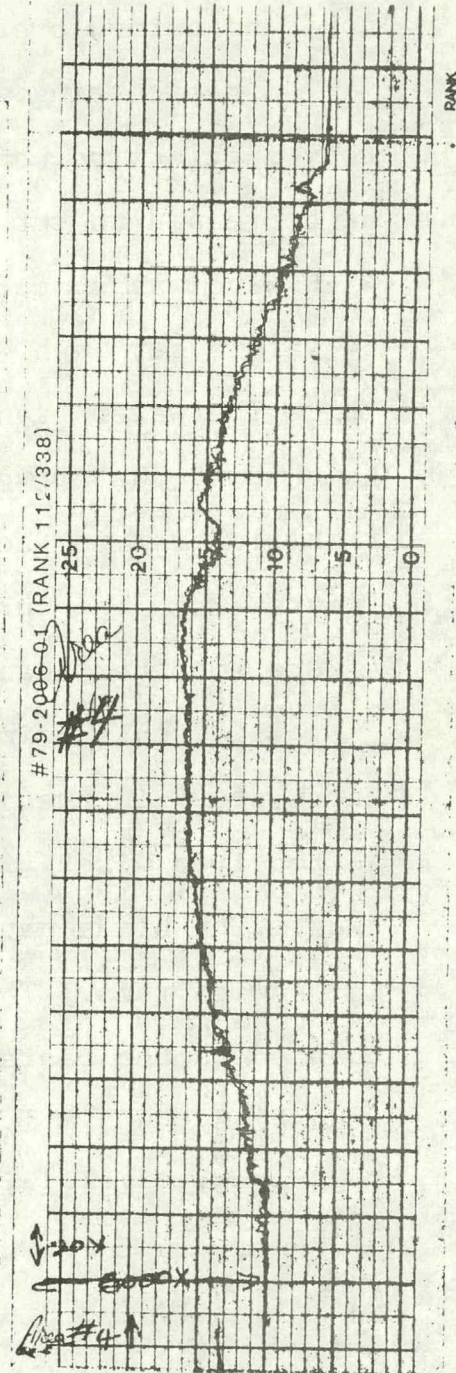
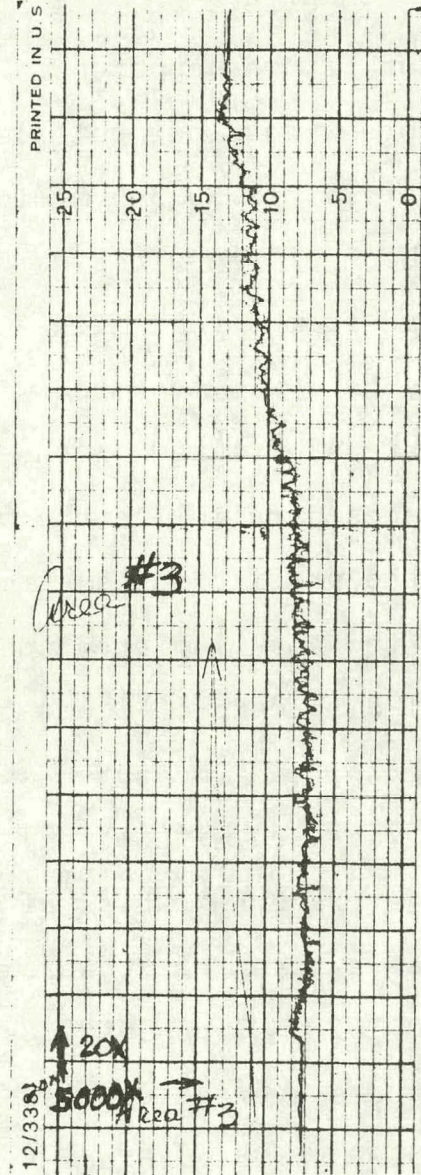
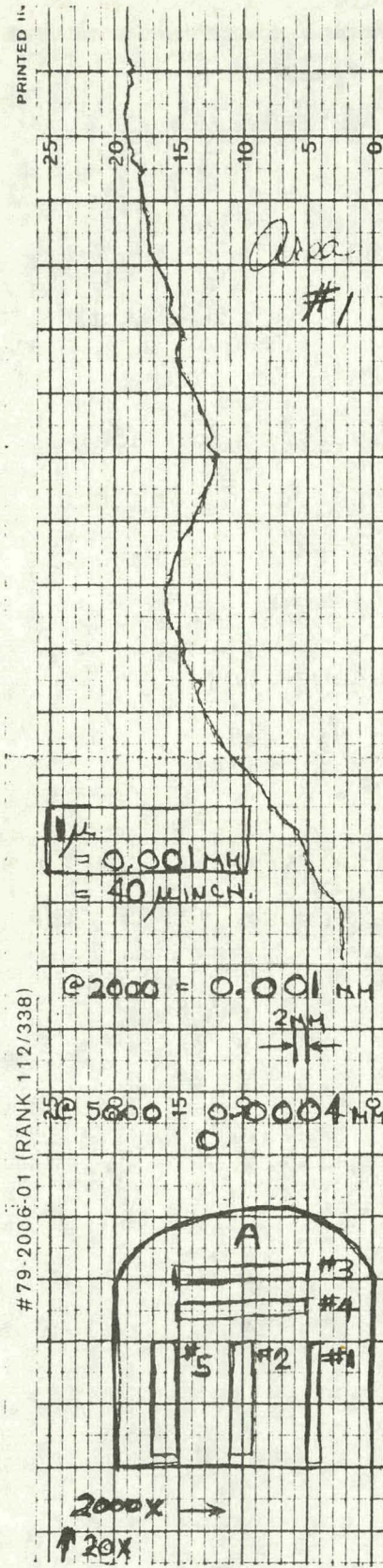


Figure 48. Profilometer tracing of 0.0055 silicon wafer 41-S

of feed forces on the cutting rates. High wafer yields obtained are indicated in Appendix E. The wafers damaged were due to the wires coming together during slicing. Some of the factors contributing to this are roller degradation and misalignment.

The usual stroke length in slicing has been 8 inches, 20.3 cm. In run 58-S and 59-S a stroke length of 4.5 inches and 6.0 inches respectively were used. However, the frequency of 108 cycles per minute and a feed force of 0.07 pounds per blade, 32 gms per blade were kept constant. These experimental conditions correspond to a minimum surface feet of 126.3 ft/min for run 58-S and 169.6 ft/min for 59-S.

In run 60-S the stroke length was changed after cutting part of the way; however, the surface feet was kept constant at 168 by increasing the cycles/min from 80 to 108. No change in cutting rates was observed. This shows that even if the stroke length is changed, it does not affect the cutting rate as long as the surface feet/min is maintained constant.

Within the limited data taken it appears that the cutting rate is independent of stroke length but depends on surface ft/min.

#### 2.5.5 Slicing a 7.6 cm Diameter Workpiece

To slice a 3-inch, 7.6 cm diameter workpiece, modification to the multi-blade wafering machine had to be made. This included: (i) Fabrication of a wire support system large enough to span a 7.6 cm workpiece; and (ii) Fabrication of pivot blocks to rock the workpiece about its center.

Run 70-S was undertaken with a 7.6 cm diameter workpiece. Extreme vibration in the feed mechanism occurred. This was apparently caused by the added drag forces due to a larger kerf length. The vibration caused 70 to 80% wafer losses.

Examination of the 7.6 cm diameter workpiece revealed a non-circular cut profile that was not apparent in 4 x 4 cm workpieces. A non-circular cut profile was caused by crank motion, i.e., lag at end of each stroke. This was undesirable since it did not minimize the contact length between the wire and workpiece. The crank motion was replaced by a linear motion drive. In addition, the feed mechanism was stiffened and carefully aligned. Run 71-S was conducted to verify the cause of the vibration. For this run, good quality wafers were sliced with 50% yield.

In summary, slicing tests verified that impregnated wires fail due to diamond pull-out. This can be minimized by nickel plating diamond impregnated wire. Electro-nickel plating diamond directly on the wires was also effective, but the kerf width could not be reduced below 9 mils as it can be for impregnated wire. Non-synchronous rocking of the workpiece is essential to minimize the contact length, thereby increasing the cutting rate and surface smoothness. The cutting rate is heavily dependent on feed force and proportional to surface speed. Thin wafers less than 4 mil, 0.1 mm can be sliced with fixed abrasive particles on wire using support rollers to minimize wander.

## 2.6 WAFER CHARACTERIZATION

### 2.6.1 Evaluation of Work Damage in Silicon Wafers

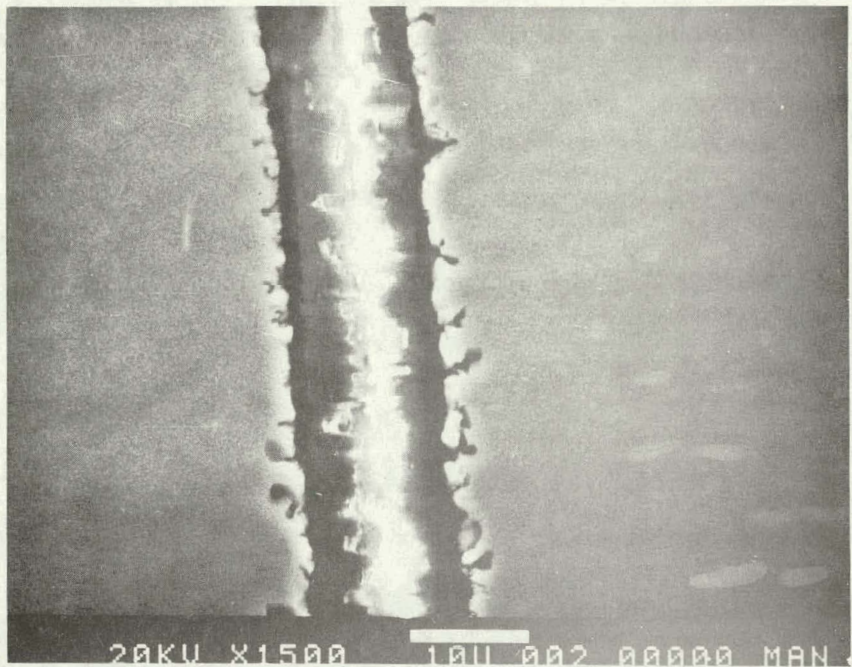
The wafering process developed by Crystal Systems has optimized the cutting of silicon wafers. The fixed abrasive method (FAM) has successfully produced wafers as thin as 4 mils (0.1 mm) over cross-sectional areas as large as 7.6 cm diameter. Even though data do suggest that this type of cutting produces less work damage in the surfaces when compared to the more conventional O.D. or I.D. type wafering, actual measurements of the work damage in these surfaces have not been conclusive in defining the depth of the residual cutting damage.

Since the expected damage will be very shallow, the problem is complicated by the thinness of the wafer and the shallowness of the damage. Hence, any measurements on the actual wafers was difficult.

One approach that has been used to measure the distribution of dislocations across a cut surface and determine if there is a significant concentration of dislocations near the cut surfaces. Such a study requires that a major crystallographic plane be exposed and etch pits developed on that plane.

A sample from the end cut was chosen because it was thick enough (6 mm) to be easily handled. The wafer was sectioned to expose a (110) plane at right angles to the (111) sliced surface. The (110) surface was polished and etched in a Sirtl etch. The depth of damage, as measured by the extent of the fissures into the material, is in the range of up to approximately 3  $\mu\text{m}$ . A SEM photograph of the two wafers is shown in Figure 49 and a magnified view in Figure 50.

In order to determine the depth of damage by another established method, tapered sections were prepared. Prior to beveling and polishing, the surface was sputter cleaned and sputtered with thin layers of chromium and gold, then electroplated with nickel. The coating preserved the original sliced surface during polishing and the  $2.3^\circ$  bevel from the (111) sliced surface allowed a 25X magnification through the thickness direction. After carefully polishing through Syton the samples were Sirtl etched to bring out dislocations. Figure 51 is a 1000X magnification metallograph of the unetched wafer showing a surface irregularity of  $\pm 0.5 \mu\text{m}$ . This is in agreement with surface roughness measurements obtained with a profilometer tracing shown in Figure 52. The etched section at 1000X magnification (Figure 53) shows dislocation pile-up on the surface. This extends only 3 to 5  $\mu\text{m}$  into the bulk, the same as the fissures shown in the (110) cross-section Figure 49.



Edge # 60

Edge #58

**Figure 49 .** SEM Photograph at 1500X Magnification of Two Wafers Showing Microfissures

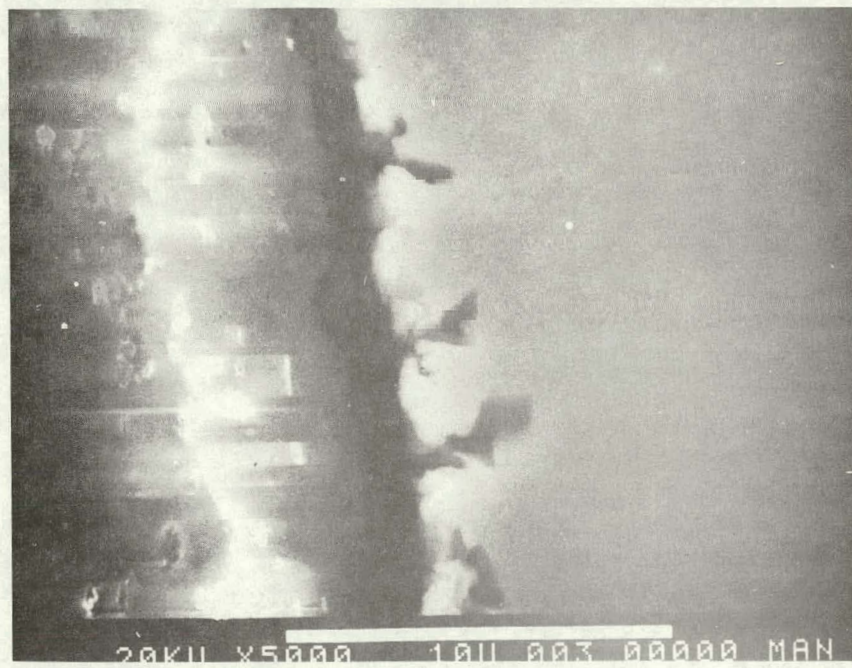


**Figure 50 .** SEM Photograph at 5000X of the Edge of Wafer 58-S

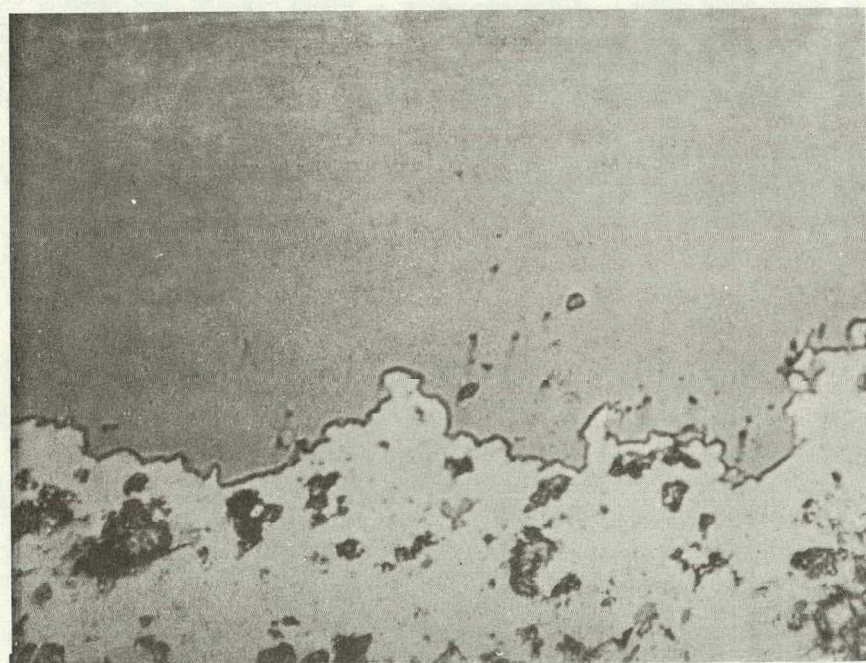


Figure 51. Photomicrograph at 1000X Magnification  
of Polished Tapered Section of Wafer (Run 59)  
Showing Surface Roughness

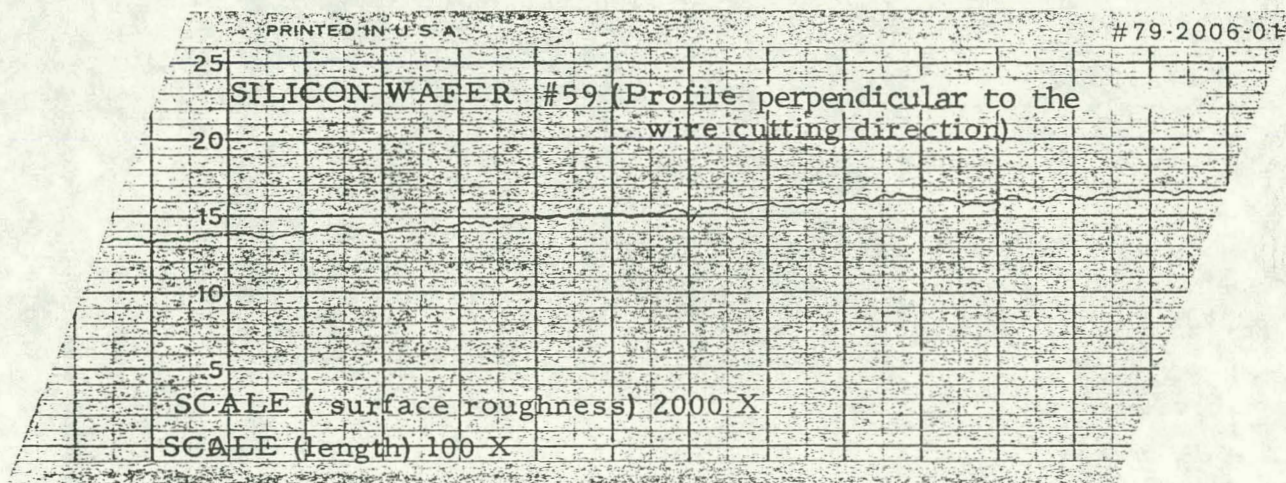
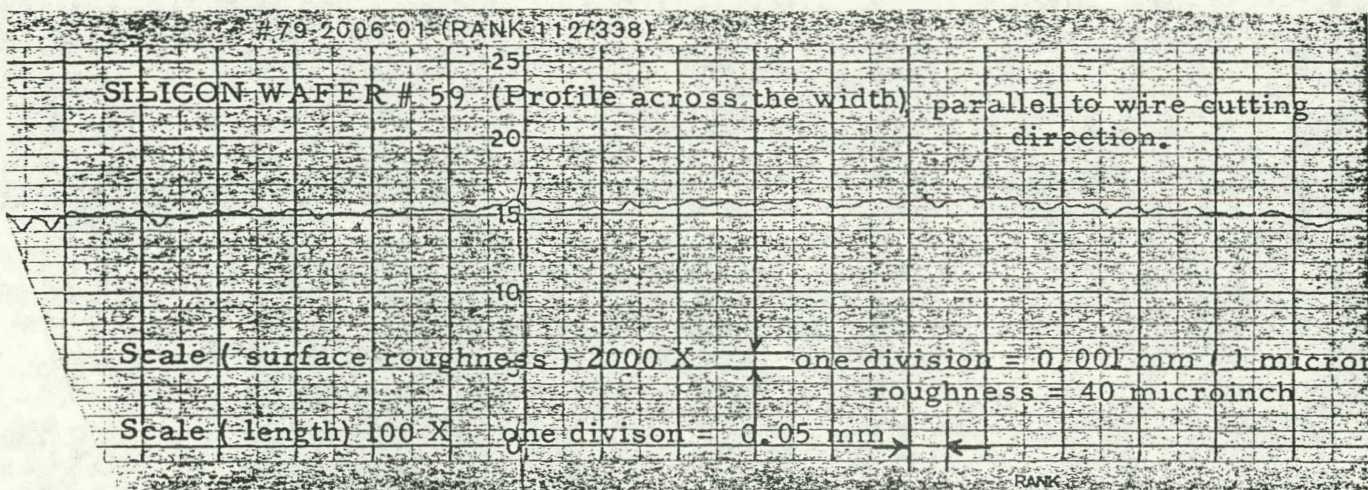


Figure 52. Profiliometer Tracing of Wafer (Run 59-S)  
 Sliced with 45  $\mu$ m Diamond and 32 gm Feed Force

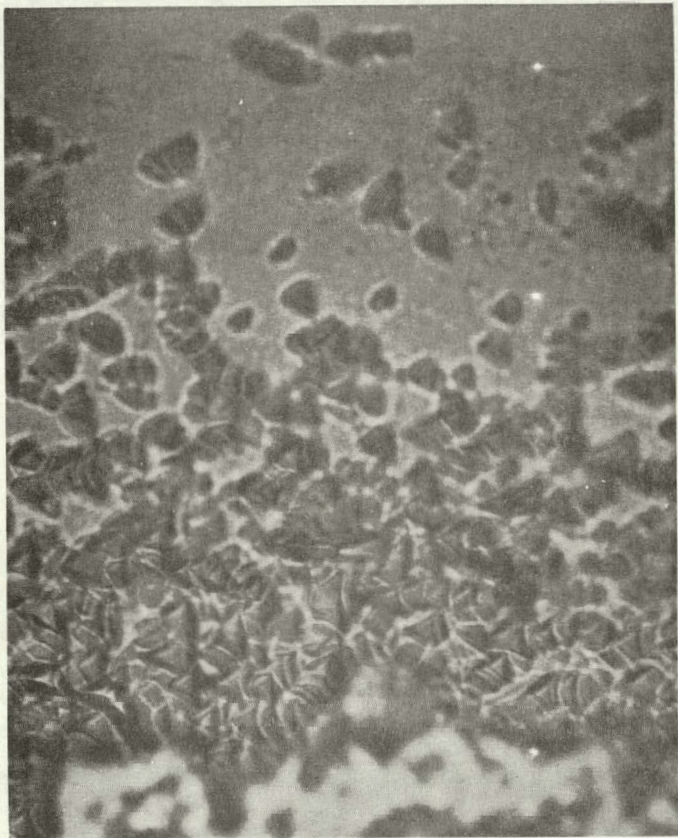


Figure 53. Photomicrograph at 1000X Magnification  
of Etched Tapered Section of Wafer (Run 59)  
Showing Dislocation Pile-up on Surface

### 2.6.2 Examination of Silicon Swarf

An aqueous solution silicon swarf generated by cutting a solid of silicon with a diamond impregnated wire, 45 micron particles, under a load of 32 grams per cutting blade was examined with the SEM.

The aqueous solution was centrifuged and the sediment then air dried. A small portion of the solid was then re-dissolved in alcohol and mixed in an ultrasonic bath. A drop of the solution was then placed on an aluminium stud and allowed to dry.

Figure 54, an SEM photograph at 15,000X, shows that the silicon swarf is a very finely divided material. The particle size is of the order of 2-3 microns but with some sub-micron particles in the residue. The individual particles have sharp edges and boundaries which suggest the material is being "fractured" out of the bulk material, rather than being eroded away. There are some isolated particles of the larger 30-45 micron diamond grit in some of the lower magnification views.

The Energy Dispersive X-ray Spectra (EDAX) displays the composition of the particles. These data show that the major component in the particles is silicon.

The shape and distribution of the particles in this sample are similar to silicon particles generated at high feed forces. There does not seem to be any significant effect on the size and shape of particles generated by varying the loading on the cutting blades.

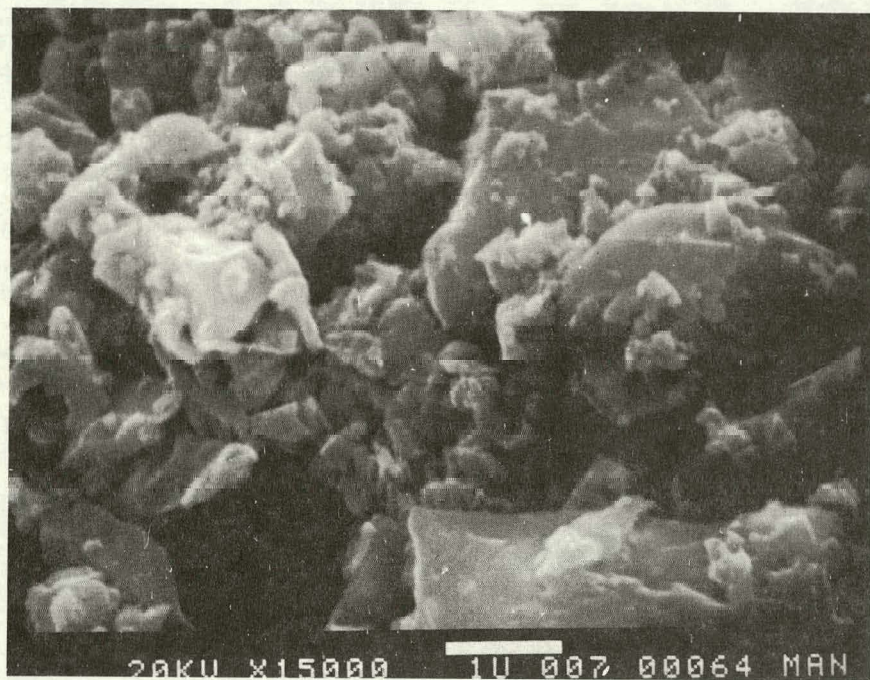


Figure 54. SEM of Silicon Swarf

### 3. ECONOMIC ANALYSIS

The economic analysis is being carried out on a projected cost basis when the development is completed and a plant is set up for production of silicon wafers. Since the cost of polycrystalline silicon will determine the cost of the final product, the calculations are based on add-on costs of casting and slicing. This analysis is carried out in three steps, viz., (1) growth of a silicon boule--ingot casting; (ii) sectioning and grinding of ingot into billets--ingot sectioning; and (iii) slicing the billets into wafers--ingot slicing.

### 3.1 INGOT CASTING

#### Assumptions:

- (1) The plant is based upon casting by Heat Exchanger Method. The size of the boule cast is 30 cm x 30 cm x 30 cm. However, the effect of size on cost parameters will be examined in the analysis.
- (2) A 100% yield factor, no need for grinding or chopping.
- (3) Cost of furnace is \$30,000.
- (4) Ten-year linear depreciation with 83% utilization.
- (5) Power consumption based on 10 Kw furnace @ 2.5 ¢/Kwh.
- (6) Direct labor at \$4.50/hr and 10 units/operator.
- (7) Supervision and overhead is 150% of direct labor costs.
- (8) Crucible is an expendable item at a cost of \$85 each. The impact of the variation of this expense on the cost analysis will be considered.
- (9) A \$20 per run miscellaneous cost is included for furnace parts, seed, recycled helium losses, etc.

Boule size	=	30 cm x 30 cm x 30 cm
	=	$27 \times 10^3 \times 2.33$ gms
	=	62.91 Kg
Man hours:		
	Cleaning	0.5 Hr.
	Charge Preparation	0.5 Hr.
	Melt Down Time	8.0 Hr.
	Melt Stabilization	1.0 Hr.
	Growth Period	$26.0^*$ Hrs.
	Cool Down	<u>12.0 Hrs.</u>
	Total	<u>48.0 Hrs.</u>

\* Considered as variable later in the analysis.

Depreciation/Run	=	$\frac{30,000 \times 48}{10 \times 52 \times 7 \times 24 \times 0.83}$
	=	\$19.86
Overhead & Labor/Run	=	$2.5 \times 4.50 \times 48/10$
	=	\$54.00
Power Cost/Run	=	$10 \times 48 \times 0.025$
	=	\$12.00
Crucible Cost	=	\$85.00
Miscellaneous Costs	=	\$20.00
Total add-on cost of casting/boule	=	\$19.86 + \$54.00 + \$12.00 + \$85.00 + \$20.00 = \$190.86
Add-on cost of casting/kg	=	\$3.03/Kg

In the above analysis it has been assumed that the crucible costs of \$85 and the solidification time is 26 hours. The impact of these variables on the add-on cost/kg is considered and results presented in Figure 55. For comparison purposes the asymptotic growth costs<sup>39</sup> based on multicharge configurations of the Czochralski method are also shown.

Another assumption is that of ingot size. In Figure 56 the effect on the growth costs of all the three assumptions in the above analysis, viz., ingot size, materials cost and growth rate, are shown. Materials costs are the crucible cost plus the miscellaneous costs. The growth costs using the Czochralski 1 charge and 5 charge approach reported are also shown. It should be pointed out that the materials cost of \$85 used is representative of larger ingots. They are expected to be much less for smaller ingots. In spite of this, the growth costs for small HEM grown ingots still compares favorably with Czochralski ingots.

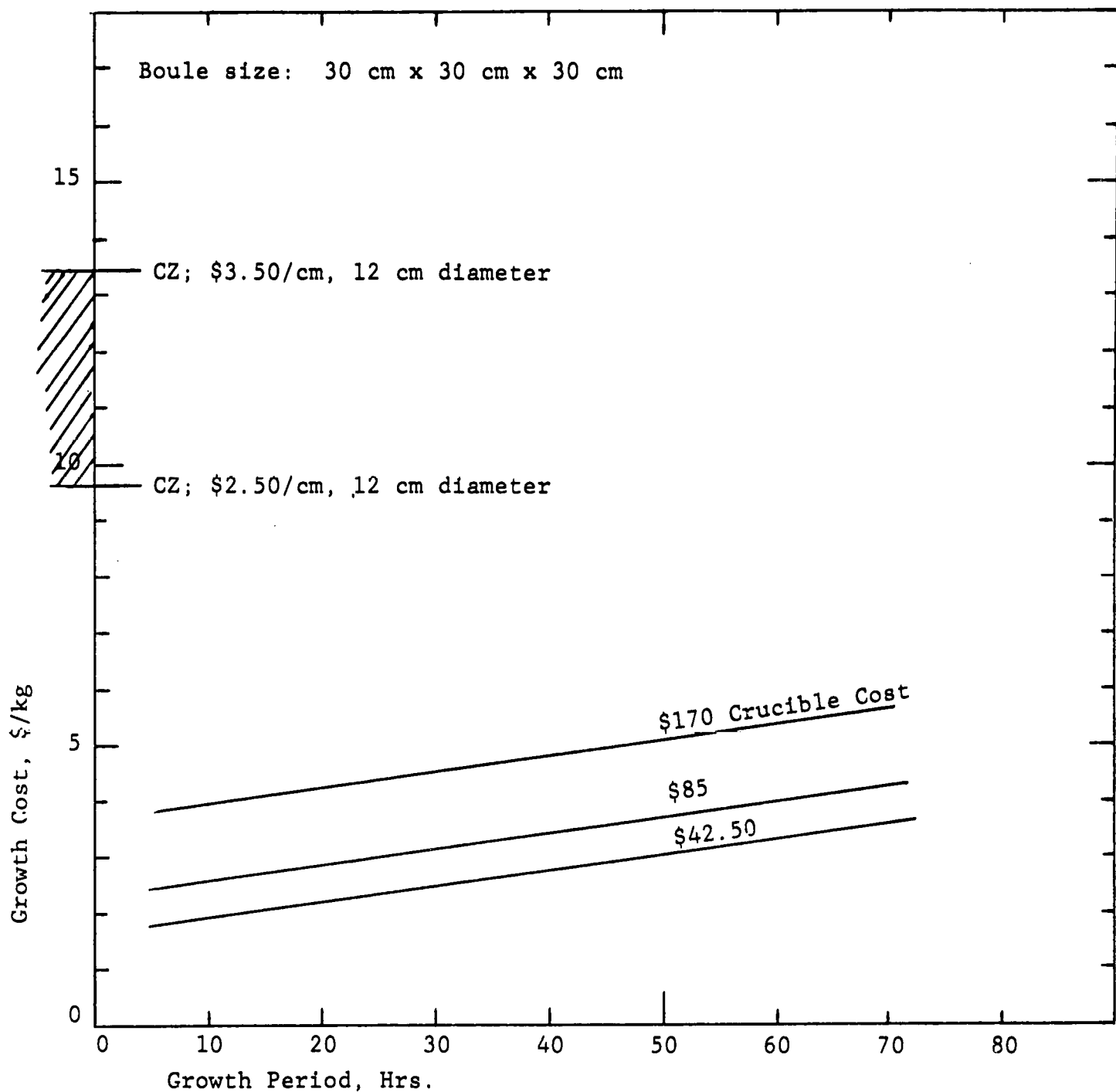


Figure 55. Impact of Crucible Cost and Solidification Time on Add-on Cost/kg

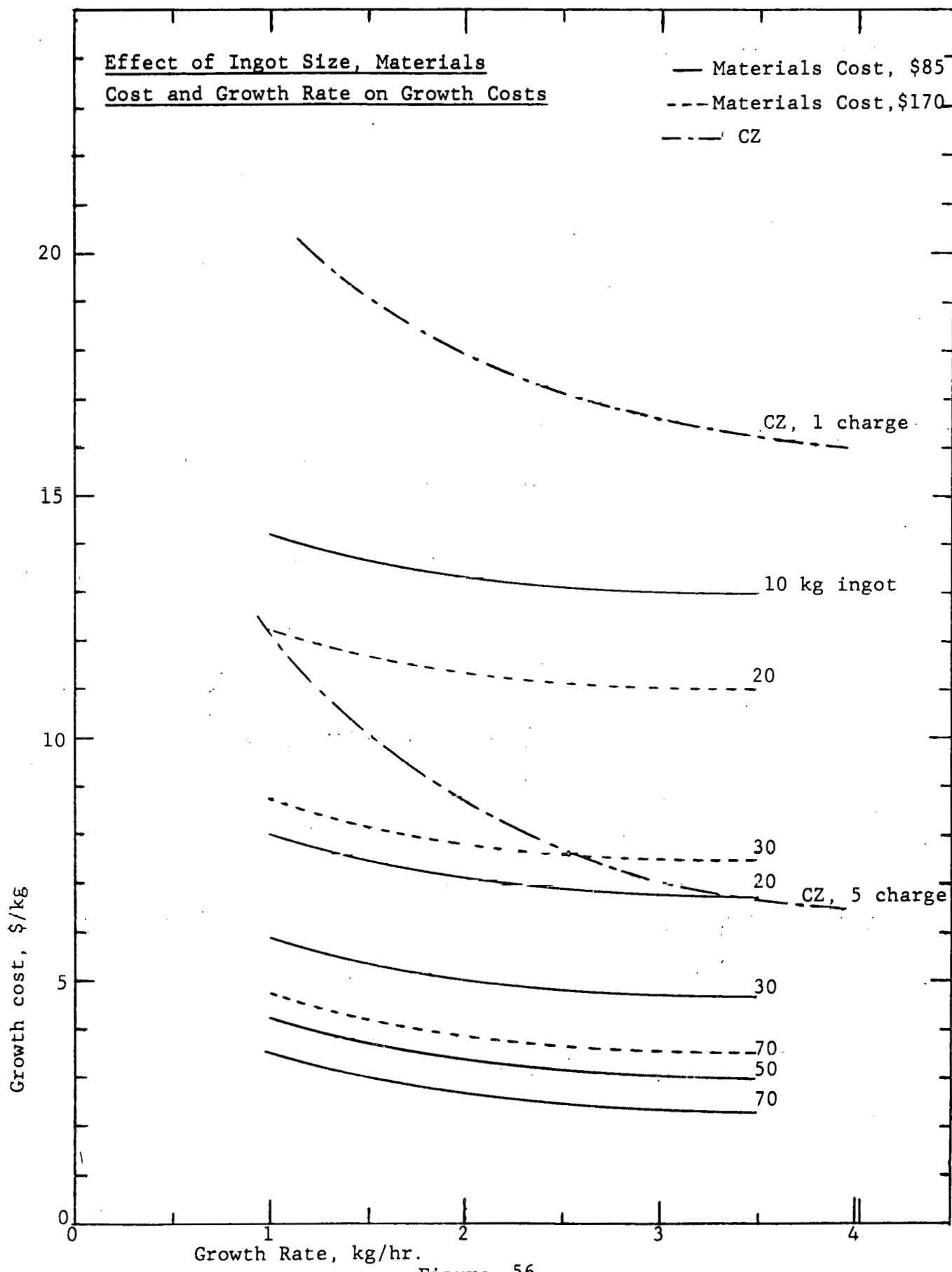


Figure 56

### 3.2 INGOT SECTIONING

#### Assumptions:

- (1) The 30 cm x 30 cm x 30 cm ingot cast is sectioned and ground to exact size into 9 billets of 30 cm x 10 cm x 10 cm size. This is performed with a band saw and grinder in 8 hours.
- (2) 100% yield.
- (3) Cost of band saw and grinder is \$25,000.
- (4) Ten year linear depreciation with 83% utilization.
- (5) Direct labor is \$4.50/hr and 1 unit/operator.
- (6) Supervision and overhead is 150% of direct labor costs.

$$\begin{aligned}\text{Depreciation/boule} &= \frac{25,000 \times 8}{10 \times 52 \times 7 \times 24 \times 0.83} \\ &= \$2.76\end{aligned}$$

$$\begin{aligned}\text{Labor & Overhead/boule} &= 2.5 \times 4.50 \times 8/1 \\ &= \$90.00\end{aligned}$$

$$\begin{aligned}\text{Total add-on cost of sectioning/boule} &= \$2.76 + \$90.00 \\ &= \$92.76\end{aligned}$$

$$\text{Total add-on cost of sectioning/Kg} = \$1.48$$

### 3.3 INGOT SLICING

#### 3.3.1 Cost of Expendable Material

A cost analysis of diamond and wire for wire slicing was made using current operation data to determine the cost of expendable materials per square meter of silicon material sliced. Five mil core material is plated and charged with diamond to 100 concentration.

Data: 100 Concentration of diamond = 72 carats/in<sup>3</sup> of bond  
(NBS Standard)

Cost of diamond - \$2.25/carat

Cost of 5 mil wire = \$40/lb or \$0.0035 per wire blade

8" stroke of machine, 9" abrasive length

5 mil, 0.125 mm wire core

0.75 mil, 18  $\mu\text{m}$  plating thickness

1.2 mil, 30  $\mu\text{m}$  diamond

$$\begin{aligned}\text{Volume of bond per wire} &= \frac{\pi}{4} (D_2^2 - D_1^2) \\ &= \frac{\pi}{4} \{(7 \times 10^{-3})^2 - (5 \times 10^{-3})^2\}9 \\ &= 0.170 \times 10^{-3} \text{ in}^3\end{aligned}$$

$$\begin{aligned}\text{Carats of diamond per wire} &= 72 \times 0.170 \times 10^{-3} \\ &= 12.24 \times 10^{-3} \text{ carats}\end{aligned}$$

$$\begin{aligned}\text{Cost of diamond per wire} &= 2.25 \times 12.24 \times 10^{-3} \\ &= \$0.0275\end{aligned}$$

In commercially impregnated wire, the diamonds are uniformly impregnated over the diameter. Crystal Systems has developed a process whereby diamonds are impregnated only in the cutting

edge, thereby reducing the diamond costs by half.

	<u>Commercial</u> <u>Process</u>	<u>CSI</u> <u>Process</u>
Cost of diamond/wire	\$ 0.0275	\$ 0.0138
Cost of wire	\$ 0.0035	\$ 0.0035
Cost of diamonds + wire/blade	\$ 0.0310	\$ 0.0173

Assuming each wire cuts 0.1 square meter of silicon, cost of expendable material/square meter of wafer,

For commercial process = \$ 0.310

For CSI process = \$ 0.173

### 3.3.2 Cost Analysis for Slicing

Assumptions:

- (1) Slicing into wafers is carried out by the fixed diamond abrasive wire.
- (2) 64 wafers/inch are mounted in the bladepack for slicing.
- (3) 100% yield, no loss due to breakage of wafers.
- (4) Cost of slicer is \$25,000.
- (5) Ten year linear depreciation with 83% utilization.
- (6) Direct labor is \$4.50/hr and 10 units/operator.
- (7) Supervision and overhead is 150% of direct labor costs.
- (8) The blade is copper-coated tungsten, impregnated with diamonds and electroless nickel plated after impregnation.

(9) Slicing is at 0.1 mm/minute.

(10) A miscellaneous cost of \$25 per boule sliced is added for slicer parts, setup epoxy, electroless nickel plating, etc.

1 boule will produce  $\frac{30}{100} \times \frac{30}{100} \times \frac{30}{2.54} \times 64 = 68.03$  sq. meters  
of silicon wafer

Time to slice 1 billet (30 cm x 10 cm x 10 cm) at 0.1 mm/min.

$$= \frac{10 \times 10}{0.1 \times 60} = 16.67 \text{ Hrs.}$$

Set-up time = 1.33 Hrs.

Time to slice/boule =  $(16.67 + 1.33) \times 9$   
= 162 Hrs.

Depreciation/boule =  $\frac{25,000 \times 162}{10 \times 52 \times 7 \times 24 \times 0.83}$   
= \$55.86

Labor & Overhead/boule =  $\frac{2.5 \times 4.50 \times 162}{10}$   
= \$182.25

Cost of wire and diamond/boule =  $0.173 \times 68.03$   
= \$11.77

Miscellaneous cost/boule = \$25.00

Total cost of slicing/boule =  $$55.86 + \$182.25 + \$11.77 + \$25.00$   
= \$274.88

Total cost of slicing = \$4.04/sq. m of silicon wafer

Total cost of casting, sectioning & slicing/boule  
= \$190.86 + \$92.76 + \$274.88  
= \$558.50

This is equivalent to \$8.88 per Kg of ingot cast and \$8.21 per square meter of silicon wafer produced. This analysis shows that these costs are below the ERDA/JPL targetted costs of \$10.90/m<sup>2</sup> by 1985.<sup>40</sup> It is assumed that these will be the final costs for production after development is completed.

#### 4. CONCLUSIONS

1. Crack-free silicon ingots up to 3.3 kg have been cast by the Heat Exchanger Method (HEM).
2. The boule sections show a high degree of single crystallinity and formation of large grains. Such structure should be acceptable for processing into solar cells.
3. Solar cells made from low purity HEM-cast material have shown conversion efficiency of over 9% (AM1). Other properties measured are dislocation density less than 100 per  $\text{cm}^2$ , minority carrier diffusion length 31  $\mu\text{m}$ , and lifetimes 20  $\mu\text{sec}$  after solar cell fabrication.
4. A crucible compatibility study program has involved the development of graded crucibles which fail during the cool-down cycle, thereby leaving a sound ingot.
5. The source of silicon carbide impurity in silicon has been identified with the reaction of graphite retainers with silica crucibles.
6. It has been established that a leak-proof seal can be formed between the graphite plug and a silica crucible. The graphite plug will result in achieving high growth rates.
7. Excellent surface quality, i.e., surface irregularities and 3-5  $\mu\text{m}$  surface damage, was achieved by non-synchronous

rocking to produce a radial cut profile in the silicon piece.

8. Wire wander was reduced by an order of magnitude to less than 0.01 mm per cm of cut depth by guiding and supporting the wires with grooved rollers.

9. Commercially available diamond impregnated wires failed due to diamond pull out. Plating after impregnation or electro-plating diamonds directly on the core minimized diamond pull-out and loss in cutting effectiveness.

10. Wires plated after impregnation hold the most promise for reducing kerf because the diamond size concentration and distribution can be controlled better than for wires directly electroplated with diamonds.

11. Tungsten wire was the best core material because of its high strength, high Young's modulus, and resistance to hydrogen embrittlement.

12. Diamond costs were cut in half by impregnating only the bottom half of the wire where active cutting takes place.

13. For fixed abrasive slicing with wire, a longer and lighter blade carriage can be used. This will allow the blade carriage to be reciprocated more rapidly to increase the surface speed.

14. A projected add-on economic analysis shows that the silicon cast by HEM process and sliced using the fixed abrasive multiple wire slicing technique will yield \$8.21/sq meter of silicon wafer.

## 5. REFERENCES

1. T. G. Digges, Jr., M. H. Leipold, K. M. Koliwad, G. Turner and G. D. Cumming, "Some Observations on the Characteristics of Low-cost Silicon Sheets," 5th IEEE Photovoltaic Specialists Conference, Baton Rouge, LA , 1976.
2. H. D. Erasmus and J. A. Persson, "Preparation and Properties of Silicon Monoxide," Trans. Electrochem. Soc. 95, 316-318 (1949).
3. D. F. Gibbons, "Thermal Expansion of Some Crystals with the Diamond Structure," Phys. Rev. 103, 569-571 (1956).
4. P. H. Gaskell, "Thermal Properties of Silica, Part 2 - Thermal Expansion Coefficient of Vitreous Silica," Faraday Soc. Trans. 62, 1505-1510 (1966).
5. C. V. Hari Rao, H. E. Bates and K. V. Ravi, "Electrical Effects of SiC Inclusions in EFG Silicon Ribbon Solar Cells," J. Appl. Phys. 47, 2614-2619 (1976).
6. F. Schmid and C. P. Khattak, "Heat Exchanger-Ingot Casting/ Slicing Process," ERDA/JPL 954373, Crystal Systems, Inc., Quarterly Technical Progress Report No. 8, October, 1977.
7. F. Schmid and D. Viechnicki, "Growth of Sapphire Discs from the Melt by a Gradient Furnace Technique," J. Amer. Ceram. Soc. 53, 528-529 (1970).
8. K. M. Kim, A. F. Witt and H. C. Gatos, "Crystal Growth from the Melt and Destabilizing Thermal Gradients," J. Electrochem. Soc. 119, 1218-1226 (1972).
9. K. M. Kim, A. F. Witt and H. C. Gatos, "A Crystal Growth Method Based on Controlled Power Reduction under Stabilizing Thermal Gradients," J. Mater. S. 6, 1036-1037 (1971).
10. F. Schmid and D. J. Viechnicki, "A New Approach to High Temperature Crystal Growth from the Melt," Solid State Tech. 16, 45-48 (1973).

11. T. G. Digges, Jr. and F. Schmid, "Growth of Large Silicon Single Crystals by a Casting Technique," *Electrochem. Soc. Spring Meeting Extended Abstracts* 77-1, 279-280 (1977).
12. E. Billig, "Some Defects in Crystals Grown from the Melt: I. Defects Caused by Thermal Stresses," *Proc. Royal Soc. A235*, 37-55 (1956).
13. D. Viechnicki and F. Schmid, "Growth of Large Monocrystals of  $Al_2O_3$  by a Gradient Furnace Technique," *J. Crystal Growth* 11, 345-347 (1971).
14. D. Viechnicki and F. Schmid, "Crystal Growth Using the Heat Exchanger Method (HEM)," *J. Crystal Growth* 26, 162-164 (1974).
15. F. Schmid and B. Reynolds, "Heat Exchanger-Ingot Casting/Slicing Process," ERDA/JPL 954373, Crystal Systems, Inc., Quarterly Technical Progress Report No. 3, June, 1976.
16. F. Schmid, "Heat Exchanger-Ingot Casting/Slicing Process," ERDA/JPL 954373, Crystal Systems, Inc., Quarterly Technical Progress Report No. 6, March 1977.
17. F. Schmid and C. P. Khattak, "Heat Exchanger-Ingot Casting/Slicing Process," ERDA/JPL 954373, Crystal Systems, Inc., Quarterly Technical Progress Report No. 7, July 1977.
18. Yu. M. Shashkon and V. P. Grishin, "Thermal Conductivity of Silicon in the Solid and Liquid States near the Melting Point," *Soviet Phys.--Solid State* 8, 447 (1966).
19. R. W. Powell, C. Y. Ho and P. E. Liley, "Thermal Conductivity of Selected Materials," *Natl. Bur. Stands. NBS-8*, Category 5, 99-106 (1966).
20. G. L. Pearson and R. G. Treuting, "Surface Melt Patterns on Silicon," *Acta Cryst.* 11, 397-399 (1958).
21. F. Schmid and C. P. Khattak, "Heat Exchanger-Ingot Casting/Slicing Process," ERDA/JPL 954373, Crystal Systems, Inc., Quarterly Technical Progress Report No. 8, October 1977.
22. T. W. Ekstedt, J. G. Mahan, R. I. Frank and R. Kaplow, "Measurement of Minority Carrier Lifetime in Solar Cells from Photo-Induced Open Circuit Voltage Decay" (to be published).
23. G. L. Pearson, W. T. Read, Jr. and W. L. Feldman, "Deformation and Fracture of Small Silicon Crystals," *Acta Met.* 5, 181-191 (1957).

24. F. Seitz, "The Plasticity of Silicon and Germanium," *Phys. Rev.* 88, 722-724 (1952).
25. H. C. Torrey and C. A. Witmer, "Crystal Rectifiers," McGraw-Hill Book Co., New York (1948).
26. W. R. Runyan, "Silicon Semiconductor Technology," McGraw-Hill Book Co., New York (1965) p. 19.
27. J. Hino and H. E. Stauss, "Melting of Undoped Silicon Ingots," *J. Metals* 4, 656 (1952).
28. C. N. Fenner, "Stability Relations of the Silica Minerals," *Amer. J. Sci.* 36, 331-384 (1913).
29. W. Witel, "Structural Anomalies in Tridymite and Cristobalite," *Ameri. Ceram. Soc. Bull.* 36, 142-148 (1957).
30. F. Schmid, U. S. Patent No. 3,898,051, Aug. 5, 1975.
31. Touloukian et al., "Thermophysical Properties of Matter," Rohsenow and Hartnett, "Handbook of Heat Transfer."
32. Nat. Bur. Standards Circ. C447 (1943).
33. Metals Handbook, Vol. I, "Properties and Selection of Metals," 8th Ed. (1961).
34. H. J. Read, Hydrogen Embrittlement in Metal Finishing, Reinhold Publishing Co., N.Y. (1961).
35. F. Badger, *Ind. Eng. Chem.* 50, 1608 (1958).
36. "The Pretreatment and Protection of Steel Parts of Tensile Strength Exceeding 90 Ton F/in<sup>2</sup>," Min. of Defense, Spec. DEF-162 H.M.S.O., London (1968).
37. B. W. Dunnington, "Proceedings: Diamond--Partner in Productivity," 50 (1974).
38. G. S. Kachadian, "A Systems Approach to Semiconductor Slicing to Improve Wafer Quality and Productivity," *Solid State Tech.*, Sept. (1970).
39. K. M. Koliwad, M. H. Leipold, G. D. Cumming, and T. G. Digges, Jr., "Economic Analysis of the Cost Silicon Sheet Produced from Czochralski Grown Material," IEEE Photovoltaic Specialists Conference, Baton Rouge, LA (1976).

40. R. W. Aster and R. G. Chamberlain, "Interim Price Estimation Guidelines," LSSA Project, JPL Report No. 5101-33 (1977).

APPENDIX A. TABULATION OF HEAT-EXCHANGER AND FURNACE TEMPERATURES

RUN	PURPOSE	SEEDING		GROWTH CYCLE			REMARKS
		FURN. TEMP. ABOVE M.P.	H.E. TEMP. BELOW M.P.	H.E. TEMP. °C/HR.	FURN. TEMP. °C	GROWTH TIME IN HOURS	
1 - 10	To test equipment	-	-	-	-	-	-
11	Improve seed melt back.	10	125	15°C/1st 138°C/6.5	10°C/7.5 Hr.		Almost no melting into seed. Ingot polycrystalline, badly broken.
12	Improve seed melt back.	10	98	150°C/1st 112°C/5	10°C/6 Hr.		Almost no melting into seed. Ingot polycrystalline, badly broken.
13	Improve seed melt back.	9	100	20°C/1st 139°C/4.5	9°C/5.5 Hr.		Almost no melting into seed. Ingot polycrystalline.
14	Improve seed melt back. Slow initial growth.	11	92	13°C/1st 286°C/7.4	11°C/8.4 Hr.		Lost seed. Ingot crumpled into pieces.
15	Improve seed melt back. Fast initial growth.	12	100	25°C/1st 138°C/4.5	12°C/5.5 Hr.		Good melt into seed. Ingot polycrystalline.
16		10	102	9°C/1st 99°C/14	10°C/15 Hr.		Almost no melting into seed. Ingot polycrystalline.
17		11	90	5°C/1st 190°C/18	18°C/19 Hr.		Seed meltback to 1½" diameter, 0.3" height. Ingot large broken single crystal.

APPENDIX A. TABULATION OF HEAT-EXCHANGER AND FURNACE TEMPERATURES (cont.)

RUN	PURPOSE	SEEDING		GROWTH CYCLE			REMARKS
		FURN. TEMP. ABOVE M.P.	H.E. TEMP. BELOW M.P.	RATE OF DECREASE H.E. TEMP. °C/HR.	FURN. TEMP. °C	GROWTH TIME IN HOURS	
18		17	112	$3^{\circ}\text{C}/1\text{st}$ $167^{\circ}\text{C}/31$	$32^{\circ}\text{C}/32\text{ Hr.}$		Seed completely melted out. Ingot large columnar grain. Cracking minimized.
19		16	112	$6^{\circ}\text{C}/1\text{st}$ $90^{\circ}\text{C}/14$	$18^{\circ}\text{C}/15\text{ Hr.}$		Seed completely melted out. Ingot large columnar grain. Very good directional solidification. Almost no cracking.
20	Slow initial growth by increasing liquid gradient.	15	132	$3^{\circ}\text{C}/1\text{st}$ $78^{\circ}\text{C}/15$	$15^{\circ}\text{C}/16\text{ Hr.}$		Seed meltback to $\frac{3}{4}$ " dia. by 0.2" height. Some seeding; mostly columnar grains. Good directional solidification.
21	Decrease furnace superheat and slow initial growth.	20	100	$1^{\circ}\text{C}/1\text{st}$ $98^{\circ}\text{C}/18$	$20^{\circ}\text{C}/19\text{ hr.}$		Seed melted out; large columnar grains.
22	Decrease furnace superheat. Increase H. E. temperature.	11	90	$4^{\circ}\text{C}/1\text{st}$ $56^{\circ}\text{C}/21$	$11^{\circ}\text{C}/22\text{ hr.}$		Good seed meltback and seeding. Seed interface not apparent.

APPENDIX A. TABULATION OF HEAT-EXCHANGER AND FURNACE TEMPERATURES (cont.)

RUN	PURPOSE	SEEDING		GROWTH CYCLE			REMARKS
		FURN. TEMP. ABOVE M.P.	H.E. TEMP. BELOW M.P.	H.E. TEMP. °C/HR.	FURN. TEMP. °C	GROWTH TIME IN HOURS	
23	Decrease furnace superheat. Increase H.E. temperature.	7	80	8°C/1st 84°C/18	7°C/19 hr.		Good seed melt-back and seed-ing.
24	Decrease furnace and H.E. temperature.	3	80	7°C/1st 47°C/11	3°C/12 hr.		No seed melt-back. Some growth off top edge of seed.
25	Decrease furnace temperature and H.E. temp.	8	78	12°C/1st 172°C/24	8°C/25 hr.		Good seeding. Center portion single crystal.
26	Decrease furnace temperature and H.E. temp.	8	70	13°C/1st 130°C/11.5	8°C/12.5 hr.		Good seeding. Center portion single crystal.
27	Decrease furnace temperature and H.E. temp.	4	73	4°C/ 6 40°C/8.5	4°C/14.5 hr.		No seed melt-back. Poly-crystalline.
28	Seed and propagate single crystallinity.	9	50	10°C/1st 85°C/13.5	9°C/14.5 hr.		Seed melted out. Columnar grains 1/2" Ø extending to concave growth interface at top of ingot.

APPENDIX A. TABULATION OF HEAT-EXCHANGER AND FURNACE TEMPERATURES (cont.)

RUN	PURPOSE	SEEDING		GROWTH CYCLE			REMARKS
		FURN. TEMP. ABOVE M.P.	H.E. TEMP. BELOW M.P.	H.E. TEMP. °C/HR.	FURN. TEMP. °C	GROWTH TIME IN HOURS	
29	Seed and propagate single crystal to crucible wall.	6	60	16°C/1st 40°C/12.5	9°C/13.5 hr.		Seed melted out. Columnar grains 1/4" Ø not extending to convex growth interface at top of ingot.
30	Seed and propagate single crystal to crucible wall.	10	70	10°C/1st 200°C/14.5	10°C/15.5 hr.		Seed melted out. Columnar grains 1/4" Ø. No visible growth interface.
31	Seed and propagate crystal. Reduce H. E. temp. at seeding.	4	72	6°C/1st 70°C/9.5	4°C/10.5 hr.		Seed melted out. Columnar grains with twins 1/2" Ø extending to flat interface.
32	Seed and propagate crystal.	13	90	10°C/1st 130°C/14	6°C/15 hr.		Seed melted out. Columnar grains 1/4" Ø. Slightly convex growth interface.
33	Seed and propagate crystal. Reduce H.E. temp. at seeding.	6	90	106°C/8.75	6°C/8.75 hr.		Good seeding and growth across dia of crucible. Convex growth interface.

APPENDIX A. TABULATION OF HEAT-EXCHANGER AND FURNACE TEMPERATURES (cont.)

RUN	PURPOSE	SEEDING		GROWTH CYCLE			REMARKS
		FURN. TEMP. ABOVE M.P.	H.E. TEMP. BELOW N.P.	H.E. TEMP. °C/HR.	DECREASE FURN. TEMP. °C	GROWTH TIME IN HOURS	
34	Seed and propagate single crystal	7	90	200°C/11	7°C/11 hr.		Seed melted out. Columnar grains $\frac{1}{2}$ " Ø extending to concave growth interface at top of ingot.
35	Seed and propagate single crystal	10	100	326°C/14	10°C/14 hr.		Seed melted out. Slow cool crystal causing it to totally shatter.
36	Seed and propagate single crystal, lower furnace temp.	5	100	290°C/11	5°C/11 hr.		Seed melt back partially with good seeding and complete crystal growth across bottom of crucible to top.
37	Seed with new-type seed.	4	90	--	Power Terminated	--	Seeding in area of seed.
38	Crucible coating run	12	No H.E.	N/A	12°C/5 hr.		Coating with 200 looks promising.
39	Crucible coating run	10	No H.E.	N/A	10°C/5 hr.		One crucible ingot produced without cracking.

APPENDIX A. TABULATION OF HEAT-EXCHANGER AND FURNACE TEMPERATURES (cont.)

RUN	PURPOSE	SEEDING		GROWTH		REMARKS
		FURN. TEMP. ABOVE M.P.	H.E. TEMP. BELOW M.P.	RATE OF DECREASE H.E. TEMP.	FURN. TEMP.	
40	Determine cause of SiC deposit. Use unground crucible.	6°C	No heat exchanger	No heat exchanger		Heavy SiC deposits on melt stock facing crucible walls.
41	Develop crucible coatings to prevent cracking.	6°C	No heat exchanger	No heat exchanger		Crucible and ingot cracked--coating too thin.
42	Determine mode of heat transfer to helium gas in heat exchanger. Determine cause of SiC deposit.	6°C	Varied			Light SiC deposits.
43	Determine cause of SiC deposit. Partial vacuum with helium atmosphere.	6°C	194°C	No growth cycle.		SiC deposit on seed and melt stock.
44	Seed and propagate crystal growth.	5°C	50°C	150°/15.75 hrs. 9.52°C/hr.	.3°C/hr.	Good seeding with single crystal growth to top and crucible wall.

## APPENDIX A. TABULATION OF HEAT-EXCHANGER AND FURNACE TEMPERATURES (cont.)

RUN	PURPOSE	SEEDING		GROWTH CYCLE			REMARKS
		FURN. TEMP. ABOVE M.P.	H.E. TEMP. BELOW M.P.	H.E. TEMP. °C/HR.	FURN. TEMP. °C	GROWTH TIME IN HOURS	
45	Determine maximum growth rate. Increase rate of heat exchanger temperature decrease.	6	70	85°C/4.3 19.8°C	12°C 2.8°C/hr.		Good seeding with growth spherical interface to within 3/8" of top surface.
46	Determine maximum growth rate. Increase rate of heat exchanger temperature decrease.	5	70	170°C/3.5 48.5°C	9°C 2.6°C/hr.		Good seeding with growth spherical interface to within $\frac{1}{2}$ " of top.
47	Determine maximum growth rate. Increase rate of heat exchanger temperature decrease.	9	70	262°C/5 52.4°C	9°C 1.8°C/hr.		Good seeding with flat interface to 1/8" from top. Cracking minimized.
48	Develop crucible coating to prevent cracking.	5	70	189°C/2.4 78.75°C	7°C 2.9°C/hr.		Cracking near top of ingot.
49	Develop crucible coating to prevent cracking	1	1280	-- Run terminated --			Silicon powder did not sinter and silicon permeated graphite crucible to form SiC

## APPENDIX A. TABULATION OF HEAT-EXCHANGER AND FURNACE TEMPERATURES (cont.)

RUN	PURPOSE	SEEDING		GROWTH CYCLE			REMARKS
		FURN. TEMP. ABOVE M.P.	H.E. TEMP. BELOW M.P.	H.E. TEMP. °C/HR.	FURN. TEMP. °C	GROWTH TIME IN HOURS	
50	Determine maximum growth rate. Increase rate of heat exchanger temperature decrease	9	70°C	551°C/4 138°C	9°C 2.25°C/hr.		Growth to top of boule. Partial seeding single crystal in center section
51	Determine maximum growth rate. Increase rate of heat exchanger temperature decrease.	11	1362	722°C-4.66 155°C	2.36°C/hr.		Seed melt out. Polycrystalline ingot.
52	Determine maximum growth rate and prevent cracking.	6	1360	560°C-5 111°C	1.2°C/hr.		Good seeding. Helium back filled at 840°C to break crucible. Ingot shattered.
53	Develop coating inside graphite crucible to prevent cracking.	4	-	1			No silicon penetration into crucible or cracking of silicon.
54	Develop coating inside graphite crucible to prevent cracking.	1	-	.1			Silicon penetrated graphite.

APPENDIX A. TABULATION OF HEAT-EXCHANGER AND FURNACE TEMPERATURES (cont.)

RUN	PURPOSE	SEEDING		GROWTH CYCLE			REMARKS
		FURN. TEMP. ABOVE M.P.	H.E. TEMP. BELOW M.P.	RATE OF DECREASE °C/HR.	H.E. TEMP. °C	FURN. TEMP. °C	
55	Develop coating for graphite and fused silica crucibles.	12° <sup>0</sup> C	-		Terminated power.		Graphite crucible cracked due to penetration of silicon. Some cracking in fused silica crucibles.
56	Develop coating for fused silica crucibles to prevent cracking.	15° <sup>0</sup> C	-	4			Silicon penetrated behind coating causing ingots to crack.
126							
57	Develop coating for graphite and fused silica crucibles.	5° <sup>0</sup> C	-	.1			SiO coating evaporated allowing silicon to attach to surface and crack.
58	Develop coating for graphite and fused silica crucibles.	10° <sup>0</sup> C	-	2			Coating failed. Silicon contacted surface.
59	Determine maximum growth rate and prevent cracking.	8° <sup>0</sup> C	1382° <sup>0</sup> C	1081° <sup>0</sup> C-3.5 84° <sup>0</sup> C	1.43° <sup>0</sup> C/hr		Good seeding. Helium back filled at 1022° <sup>0</sup> C to break crucible. Ingot shattered.

## APPENDIX A. TABULATION OF HEAT-EXCHANGER AND FURNACE TEMPERATURES (cont.)

RUN	PURPOSE	SEEDING		GROWTH CYCLE			REMARKS
		FURN. TEMP. ABOVE M.P.	H.E. TEMP. BELOW M.P.	RATE OF DECREASE H.E. TEMP. °C/HR.	FURN. TEMP. °C	GROWTH TIME IN HOURS	
60-C 127	Determine maximum actual growth rate. Graphite plate seated on heat exchanger to extract heat across entire bottom.	< 5'	37°C (1360°)	285°C(3.5 hr.) 81°C/hr.	11°C (3.5 hr.) 3.14°C/hr.		Top froze as $\frac{1}{2}$ " thick polycrys- talline layer. Good seeding with single crystal growth from seed.
61-C	Same as 60-C. Re- duced heat loss by reducing size of view port in top cover.	< 6	21°C (1383°)	409°C(5.16 hr.) 79°C/hr.	6°C (5.16 hr.) 1.16°C/hr.		Good seeding and growth to top of ingot.
62-C	Same as #61-C. Thin wall crucible (.040")	< 5	21°C (1384°)	541°C(4.5 hr.) 141°C/hr.	1.11°C/hr.		Silicon ingot shattered. Seed melt out.
63-C	Same as #60-C			Run terminated one hour after all liquid. Possible heat exchanger failure.			Polycrystalline material.
64-C	Develop liner inside graphite crucible to prevent cracking.		Approximately 15°C (1.75 hr.)				Woven silica material failed. Second crucible-- cast liner--silicon penetrated.

APPENDIX A. TABULATION OF HEAT-EXCHANGER AND FURNACE TEMPERATURES (cont.)

RUN	PURPOSE	SEEDING		GROWTH CYCLE			REMARKS
		FURN. TEMP. ABOVE M.P.	H.E. TEMP. BELOW M.P.	H.E. TEMP. °C/HR.	RATE OF DECREASE H.E. TEMP. °C/HR.	FURN. TEMP. °C	
65-C	Grow single crystal to periphery of crucible and de- velop cooling cycle to prevent cracking.	< 5			1	3	Insufficient melt back on outer periphery of seed.
66-C	Develop crucible liner in graphite mold. Cycle quartz through high low transformation temperature.		Heat to 850°C in vacuum for two hours.				Low to high quartz trans- formation caused crucible to crack.
67-C	Grow single crystal < 3	52 (1360)		80	0	4	Insufficient melt back on outer periphery of seed.
68-C	Grow single crystal to periphery of crucible and develop cooling cycle to prevent cracking.	< 3	22	82	0	5	Insufficient melt back on outer periphery of seed.
69-C	Grow single crystal to periphery of crucible and develop cooling cycle to prevent cracking.	< 3	18	80	0	7	Insufficient melt back on periphery of seed.

## APPENDIX A. TABULATION OF HEAT-EXCHANGER AND FURNACE TEMPERATURES (cont.)

RUN	PURPOSE	SEEDING		GROWTH CYCLE			REMARKS
		FURN. TEMP. ABOVE M.P. °C	H.E. TEMP. BELOW M.P. °C	RATE OF DECREASE H.E. TEMP. °C/HR.	FURN. TEMP. °C/HR.	GROWTH TIME IN HOURS	
70-C	Achieve lateral growth	< 3	23	81	0	6.5	Insufficient melt-back of seed
71-C	Achieve lateral growth	< 3	19	59	0	8.75	Graphite ring at bottom broke
72-C	Achieve lateral growth	< 3	34	92	0	6.8	Good melt-back achieved
129	73-C	Sintering of crucible liners at approx. 840°C	-	-	-	-	No change in appearance of crucibles after the run.
74-C	Achieve lateral growth	< 3	33	85	0	5.75	Good melt-back and lateral growth achieved
75-C	Provide better heat conduction to the heat exchanger	< 3	79	96	0	7.25	A graphite plug was used at the hole in center of crucible. Seed lost.
76-C	To avoid cracking of ingot using SiO <sub>2</sub> liners	10	-	-	-	4	Silicon in high purity liner has not cracked.
77-C	Achieve lateral growth	?	57	87	0	4.25	Instrumentation malfunction. Seed melted.

APPENDIX A. TABULATION OF HEAT-EXCHANGER AND FURNACE TEMPERATURES (cont.)

RUN	PURPOSE	SEEDING		GROWTH CYCLE			REMARKS
		FURN. TEMP. ABOVE M.P. °C	H.E. TEMP. BELOW M.P. °C	H.E. TEMP. °C/HR.	RATE OF DECREASE FURN. TEMP. °C/HR.	GROWTH TIME IN HOURS	
78-C	To avoid cracking of ingot using SiO <sub>2</sub> liners	< 3	-	-	-	-	Regular grade thin crucible showed no cracking of ingot
79-C	To achieve lateral growth	< 3	44	86	0	6	Not enough melt-back of the seed achieved
80-C	To achieve lateral growth	< 3	38	58	0	8	Good growth achieved to one side of the seed
81-C	Casting in seeded free standing crucible liner	3	77	46	0	6.25	Seed melted. Silicon penetrated thru liner.
82-C	Achieve lateral growth	<3	64	90	0	9.5	Good seed melt-back. Single crystal above the seed as well as good lateral growth.
83-C	Achieve lateral growth	<3	70	88	0	8.5	Growth above the seed as well as in the lateral direction.
84-C	Testing of hot pressed and high purity crucibles. Sintering of pressure cast crucibles.	<3	137	51	2	9.0	The silicon in the hot pressed crucible did not show any cracking.

## APPENDIX A. TABULATION OF HEAT-EXCHANGER AND FURNACE TEMPERATURES (cont.)

RUN	PURPOSE	SEEDING			GROWTH CYCLE			REMARKS
		FURN. TEMP. ABOVE M.P. °C	H.E. TEMP. BELOW M.P. °C	H.E. TEMP. °C/HR.	TEMP. °C	DECREASE FURN. TEMP. °C	GROWTH TIME IN HOURS	
85-C	Achieve good growth	<3	75		79	0	6.0	Good seed melt-back and growth above the seed and sides
86-C	Testing of spray coated crucibles	<3				0		Coatings generally "crazed."
87-C	Study effect of new viewport	<3	62		67	3	12.6	Melt-back of seed near sides only.
88-C	Improve heat transfer	<3	59		-	0	-	Run aborted. Heat exchanger damaged.
89-C	Study effect of ultrasonic sensor rods	8	51		139	8	5.5	Seed melted out.
90-C	Casting in spray-coated, pressure-cast and hot-pressed crucibles.	4	137		118	6	10.75	Crackfree silicon in two pressure-cast crucibles. Silicon in the spray-coated crucibles showed fine cracks.
91-C	Prevent cracking using thin, clear crucible.	7	75		155	-	-	Run aborted due to crucible failure.
92-C	Prevent cracking using low-density, slip-cast silica crucible.	16	217		-	-	-	Run aborted due to crucible failure.

APPENDIX A. TABULATION OF HEAT-EXCHANGER AND FURNACE TEMPERATURES (cont.)

RUN	PURPOSE	SEEDING		GROWTH CYCLE			REMARKS
		FURN. TEMP. ABOVE M.P. °C	H.E. TEMP. BELOW M.P. °C	TEMP. °C/HR.	DECREASE H.E. TEMP. °C/HR.	FURN. TEMP. °C	
93-C	Prevent cracking using thin, clear crucible.	4.5	97	177	8.5	7.5	Crack-free ingot cast.
94-C	Casting in glazed slip-cast crucible.	<3	94	164	0	2.5	Crack-free ingot cast.
132	95-C Achieve good growth using thin, clear crucible	7	59	179	11	9.8	Crack-free ingot cast. Good seed melt-back and growth above the seed and sides.
96-C	Prevent cracking using graded slip-cast high purity crucible	4	187	-	-	-	Power terminated during growth. Silicon penetrated through the crucible.
97-C	Prevent cracking using graded slip-cast technical grade crucible	3	120	165	2	4.0	Crack-free silicon cast.
98-C	Study effect of grading in slip-cast technical grade crucible	3	120	164	2	6.8	Silicon cracked into pieces. Indicates that heat treatment prevents cracking.

## APPENDIX A. TABULATION OF HEAT-EXCHANGER AND FURNACE TEMPERATURES (cont.)

RUN	PURPOSE	SEEDING		GROWTH CYCLE			REMARKS
		FURN. TEMP. ABOVE M.P.	H.E. TEMP. BELOW M.P.	RATE OF DECREASE H.E. TEMP. °C/HR.	FURN. TEMP. °C	GROWTH TIME IN HOURS	
99-C	Prevent cracking using graded, spray-coated crucible.	3	120	170	0	3.3	Silicon cracked in areas where coating did not adhere to the crucible.
100-C	Prevent cracking using graded, opaque crucible	4	76	171	5	8.0	Crack-free boule cast (1.5 kg)
101-C	Seeded growth using graded, opaque crucible	3	86	174	3	8.5	Crack-free boule cast (2.6 kg)
102-C	Prevent cracking using graded, coated crucible	5	90	147	5	5.2	Silicon cracked. Coating removed up to melt level.
103-C	Prevent cracking using translucent graded crucible	4	77	171	4	7.0	Crack-free ingot with no attachment of crucible.
104-C	Prevent cracking using translucent graded crucible	5	63	159	7	9.25	Ingot cracked because of attachment to areas of crucible with non-uniform graded structure.

APPENDIX A. TABULATION OF HEAT-EXCHANGER AND FURNACE TEMPERATURES (cont.)

RUN	PURPOSE	SEEDING		GROWTH CYCLE			REMARKS
		FURN. TEMP. ABOVE M.P.	H.E. TEMP. BELOW M.P.	H.E. TEMP. °C/HR.	FURN. TEMP. °C	GROWTH TIME IN HOURS	
105-C	Improve heat transfer using a graphite plug at bottom of crucible	-	-	-	-	-	Run terminated as crucible failed before reaching melt temperature.
106-C	Confirm experimentally if graphite retainer is source of SiC	-	-	-	-	-	Only Si around graphite piece showed SiC formation.
107-C	To form a compression fit between graphite plug and crucible	12	64	172	10	1.75	Crucible warped and silicon leaked out.
108-C	To form a compression fit between graphite plug and crucible	6	79	166	0	2.25	Crucible warped around plug. The seed bonded to the graphite.
109-C	Casting large Si ingot in opaque graded crucible (3.3 Kg)	8	89	138	7	12.0	Crack-free ingot cast

## APPENDIX A. TABULATION OF HEAT-EXCHANGER AND FURNACE TEMPERATURES (cont.)

RUN	PURPOSE	SEEDING		GROWTH CYCLE			REMARKS	
		FURN. TEMP. ABOVE M.P.	H.E. TEMP. BELOW M.P.	H.E. TEMP. °C/HR.	FURN. TEMP. °C	GROWTH TIME IN HOURS		
110-C	Improve heat transfer using graphite plug	11	96	106	2	6.0	No leakage around plug. Crack-free boule cast.	
111-C	Improve heat transfer using graphite plug	-	-	-	-	-	Crucible failed when most material was molten. Run aborted. No leakage around plug.	
135	112-C	To cast a crack-free single crystal boule	12	84	-	7	8.75	H.E. thermocouple malfunction. Helium flow at maximum from one-half hour into growth cycle. Crack-free boule cast.
113-C	Casting crackfree boule in opaque graded crucible (type II)	14	54	160	14	16	Crackfree boule cast. Seed melted out.	
114-C	Casting single crystal crackfree boule	17	72	-	17	13.75	Crackfree boule cast. Seed melted out.	
115-C	Testing of ultrasonics to monitor liquid/solid interface	12	68	170	12	9.25	Most of silicon cast as single crystal but cracked on cooling due to bonding with crucible	

APPENDIX A. TABULATION OF HEAT-EXCHANGER AND FURNACE TEMPERATURES (cont.)

RUN	PURPOSE	SEEDING		GROWTH CYCLE			REMARKS
		FURN. TEMP. ABOVE M.P.	H.E. TEMP. BELOW M.P.	H.E. TEMP. °C/HR.	FURN. TEMP. °C	GROWTH TIME IN HOURS	
116-C	Casting a 4 kg boule in opaque graded crucible (type II)	-	-	-	-	-	Run aborted due to loss of vacuum.
117-C	Casting 4 kg ingot	-	-	-	-	-	Run aborted due to crucible failure
118-C	Effect of Mo retainer	37	31	120	37	17.0	Seed melted out. Crackfree boule cast. No SiC on sur- face.
136	119-C Improve growth	7	65	200	7	6.6	Good seed meltback and growth above seed. No SiC on surface.
120-C	Promote fast meltdown	22	26	146	22	21.5	Seed melted out.
121-C	Promote fast meltdown	14	39	173	14	11.25	Heat exchanger thermocouple failed; seed melted out.
122-C	Improve growth	17	104	134	17	6.0	Seed melted out.
123-C	Improve growth	8	50	184	8	9.0	Good seed meltback and growth. Large grains growth from top surface as well.
124-C	Improve growth	7	36	162	3	8.0	Good seed meltback and growth

## APPENDIX B

### B.1 SOURCE OF FORMATION OF SILICON CARBIDE - THEORETICAL

#### B.1.1 Introduction

Silicon crystals are grown in 0.1 torr vacuum by the Heat Exchanger Method (HEM). There is experimental evidence to show that silicon monoxide (SiO) and silicon carbide (SiC) are by-products of the process. Oxygen, silicon and carbon are used in this method in the form of silicon melt stock, silica crucibles and graphite furnace parts and retainers. In an effort to understand the reactions taking place in vacuum at high temperatures and to find ways to eliminate undesirable products of reactions, detailed thermodynamic calculations were initiated. Summary of thermochemical data used for analysis is shown in Table B.

#### B.1.2 Sources of Thermochemical Data Employed in the Analysis

Table B summarizes the thermochemical data required to carry out the calculations of oxygen solubility. These data are taken from several standard sources, supplemented by the ManLabs--NPL DATABANK and are believed to represent the best current description available.

TABLE B  
SUMMARY OF THERMOCHEMICAL DATA\*  
(Temperature Range 1300°K to 1800°K)

<u>Compound</u>	<u>Standard</u>
	<u>Free Energy of Formation</u> (cal/mol)
SiC (solid)	-18,200 + 3.0T, T = °K
CO (gas)	-28,300 - 20.0T
CO <sub>2</sub> (gas)	-94,700
SiO <sub>2</sub> (solid)	-218,300 + 43.0T
SiO (gas)	-27,100 - 18.0T

The free energy difference between  $1/2 O_2$  (gas) at one atmosphere and  $O$  dissolved in liquid silicon is:

$-86000 + 28.0T + RT \ln N$  cal/mole of  $O$  where  
 $T = °K$ ,  $R = 1.9873$  cal/mol°K and  $N$  is the atomic fraction of oxygen. Thus if the number of oxygen atoms per cubic cm is  $N_A$  then  $N = N_A \div (6.03 \times 10^{23} \times 2.33 \text{ gms/cm}^3 \div 28.09 \text{ gms/mole}) = N_A \div 5 \times 10^{22}$ . The solubility of oxygen in silicon (in equilibrium) with SiO<sub>2</sub> is equal to  $4 \times 10^{-6}$ ,  $8 \times 10^{-6}$  and  $18 \times 10^{-6}$  atom fractions at 1273°K, 1373°K and 1523°K respectively. These concentrations correspond to  $2 \times 10^{17}$ ,  $4 \times 10^{17}$  and  $9 \times 10^{17}$  oxygen atoms/cm<sup>3</sup> at the above noted temperatures.

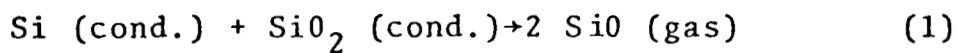
\*References: JANAF THERMOCHEMICAL TABLES.

ManLabs -NPL Data Bank.

O. Kubaschewski and T. G. Chart, J. Chem. Thermo (1974), 6 467 and "Constitution of Binary Alloys- First Supplement" R. P. Elliot McGraw Hill, New York, 1965.

### B.1.3 Consideration of the Reaction between Liquid Silicon and Silica Crucible I

The first problem which must be considered is the possible interaction between liquid silicon and the silica crucible at temperatures in the range 1685°K to 1735°K and at pressures in the 0.01 to 1.0 torr range. Figure B-1 shows the results obtained by considering the reaction



The free energy change for Equation (1),  $\Delta G$  can be calculated from the data given in Table B as

$$\Delta G = \Delta G^\circ + 2RT \ln p(\text{SiO}) \quad (2)$$

where  $T = ^\circ\text{K}$  and  $p(\text{SiO})$  is the pressure of gaseous SiO in atmospheres. Making the conversion from atmospheres to torr (760 torr is equal to one atmosphere) yields the following result:

$$\log p(\text{SiO}) \text{ torr} = 11.47 - 17900T^{-1} \quad (3)$$

Figure B-1 shows the result of Equation (3) in dividing the temperature - pressure regime into a region where the reaction shown in Equation (1) proceeds to the right (forming SiO and consuming the crucible) and a second range where the crucible containing the liquid silicon is stable. The present working range appears to lie in a range where SiO (gas) is stable thus leading to consumption of the crucible.

### B.1.4 Consideration of the Reaction between Liquid Silicon and Silica Crucible II

If the reaction between liquid silicon and the crucible is carried out in an environment where oxygen is released as in Equation (4), then the temperature - pressure regimes shown in Figure B-1 will be altered. In particular, if

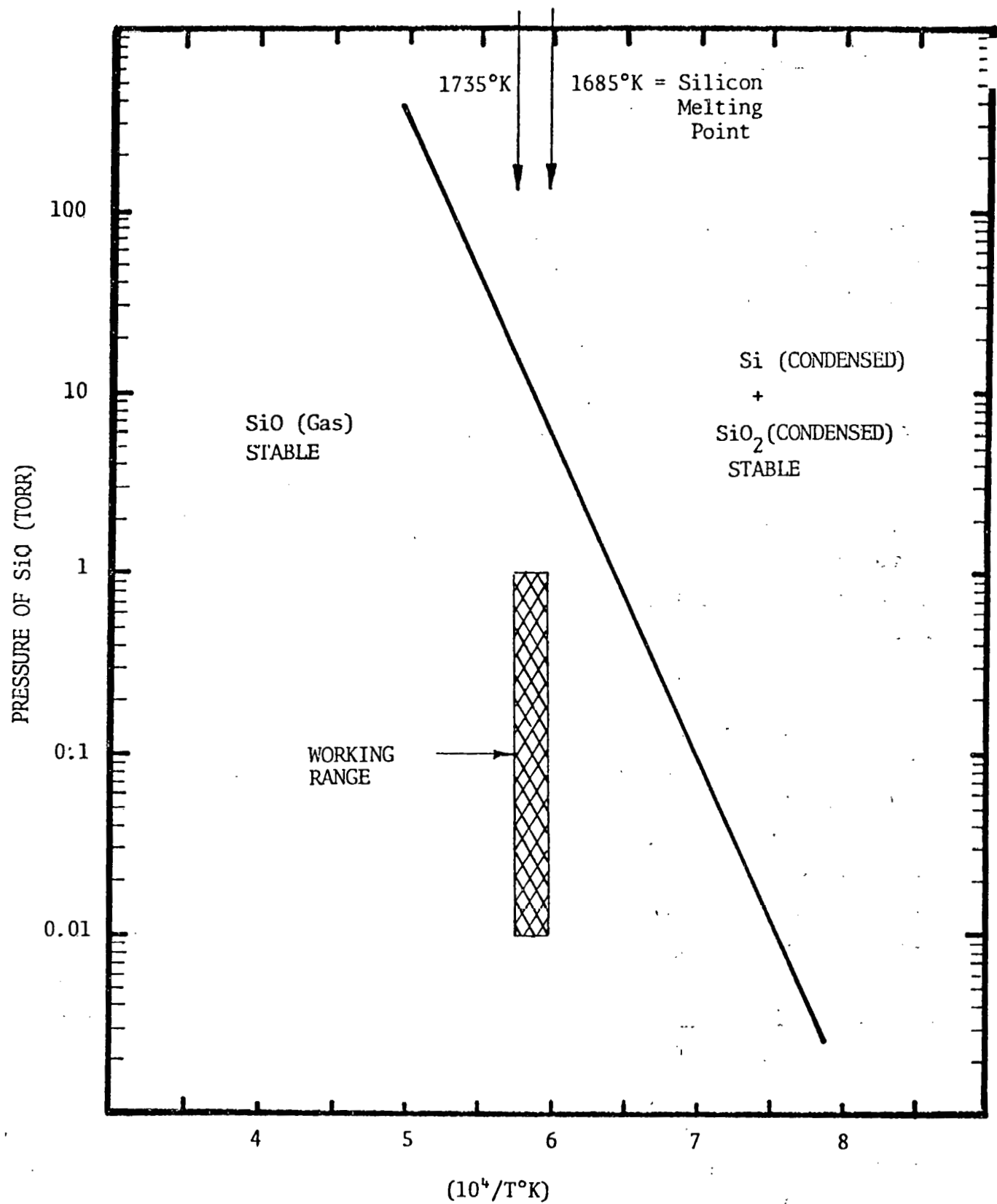
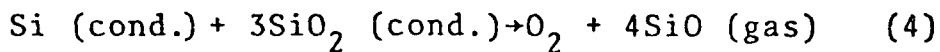


Figure B-1. Equilibrium Vapor Pressure of Gaseous SiO as a Function of Temperature for the Reaction Si (CONDENSED) + SiO<sub>2</sub> (CONDENSED)  $\rightarrow$  2SiO (gas).



then the pressure of SiO will be equal to four times the pressure of oxygen and the total pressure  $P_T$  in torr will be given by Equation (5) on the basis of data shown in Table B.

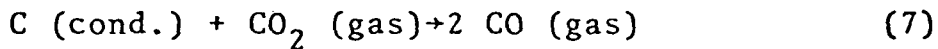
$$\log P \text{ (total) (torr)} = 11.78 - 23850T^{-1} \quad (5)$$

Equation (5) leads to the results shown in Figure B-2 which discloses that the phase boundary between the stable condensed phases and stable gaseous ranges has now shifted from above the working range to below the working range. Thus, on the basis of Figure B-2 crucible decomposition would not occur in contrast to Figure B-1 which suggests that crucible decomposition will occur on the basis of reaction (1).

Unfortunately, the environment in which the melting of silicon in silica crucibles is being carried out at present (i.e., in graphite furnaces) favors Equation (1) over Equation (4). This can readily be seen by considering the general equilibrium between CO and  $\text{CO}_2$  under the conditions characterized by the proposed working range.

#### B.1.5 Examination of the $\text{CO}/\text{CO}_2$ Equilibrium in the Working Range

The data contained in Table can be employed to examine the reaction



Since

$$\Delta G = \Delta G^\circ + RT \ln \frac{P_{\text{CO}}}{P_{\text{CO}_2}} \quad (8)$$

and  $\Delta G^\circ = 38100 - 40T$  calories, the reaction proceeds strongly to the right at  $1700^\circ\text{K}$  and pressures near 1 torr (i.e.,  $10^{-3}$  atmospheres). Thus CO will be the dominant species. This conclusion would be even stronger if graphite were to react

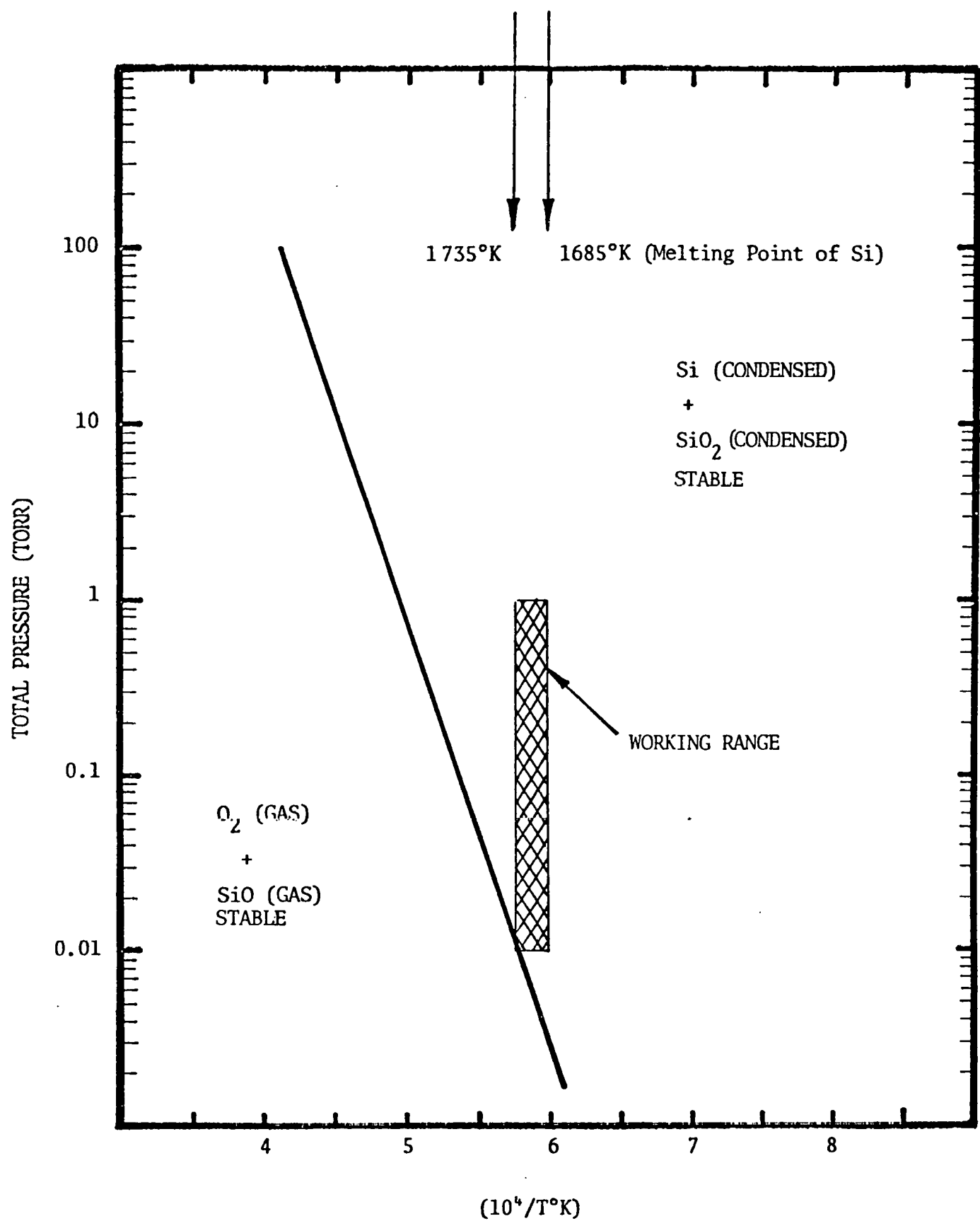


Figure B-2 TOTAL EQUILIBRIUM VAPOR PRESSURE OF  $\text{SiO}$  AND  $\text{O}_2$  FOR THE REACTION  $\text{Si (CONDENSED)} + 3 \text{SiO}_2 \text{ (CONDENSED)} \rightleftharpoons \text{O}_2 + 4 \text{SiO (GAS)}$ .

with oxygen in place of  $\text{CO}_2$  in Equation (7).

The conclusion reached on the basis of Equations (1) through (8) and Figures B-1 and B-2 is that a reaction between the silica crucible and molten silicon is likely to occur under the present working conditions on the basis of Figure B-1 which represents a better description of the environment than Figure B-2. This reaction might be suppressed by operating at a slightly higher pressure (i.e., 10 torr) and restricting the conditions to the range where the condensed gases in Figure B-1 are more stable than the gaseous phases. The remaining question is what are the resulting levels of oxygen concentration in the silicon to be expected under these conditions. This question is addressed in Sections B.1.6 and B.1.7 below.

#### B.1.6 Evaluation of the Reaction between Oxygen Dissolved in Silicon with Silicon to Form Gaseous $\text{SiO}$

Table B contains a characterization of the reaction between oxygen dissolved in liquid silicon and silicon to form  $\text{SiO}$  (gas) at one atmosphere. At lower pressures, this reaction can be characterized by means of Equation (9), where  $T = {}^\circ\text{K}$ ,  $P(\text{SiO})$  (torr) is the pressure and  $N$  is the atomic fraction of oxygen in silicon. Table B shows that if  $N = 10^{-5}$  then the number of oxygen atoms per  $\text{cm}^3$  (of silicon) is  $5 \times 10^{17}$ .

$$\log \frac{P(\text{SiO})}{N} \text{ (torr)} = 12.93 - 12870T^{-1} \quad (9)$$

The results of Equation (9) are displayed in Figure B-3 showing the phase boundaries for the formation of  $\text{SiO}$  (gas) as a function of pressure, temperature and the concentration of oxygen in silicon. Figure B-3 also displays the crucible decomposition boundary derived in Figure B-1. Reference to Figure B-3 suggests that rather low concentrations of oxygen could be attained at the low pressure end of the working range. However, this re-

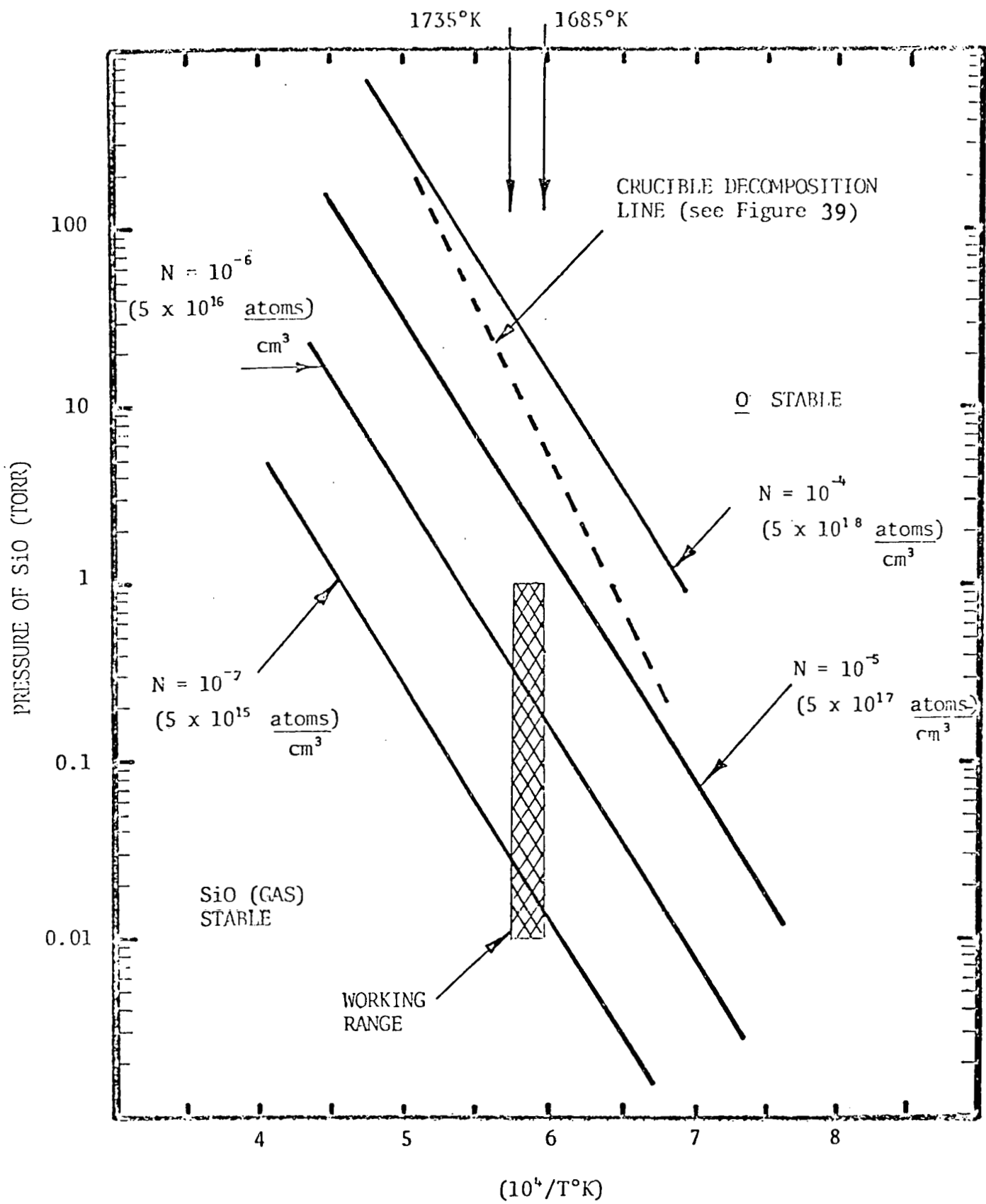


Figure B-3. EQUILIBRIUM BOUNDARY FOR THE REACTION  $\text{O}$  (DISSOLVED OXYGEN) +  $\text{Si}$  (CONDENSED)  $\rightarrow \text{SiO}$  (GAS) AS A FUNCTION OF OXYGEN CONCENTRATION (IN ATOMIC FRACTION AND ATOMS/cm<sup>3</sup>).

sult will be conditioned by the crucible decomposition line. Thus at pressures near 10 torr and temperatures near 1700°K oxygen concentrations of  $3 \times 10^{18}$  atoms/cm<sup>3</sup> could be attained. Further lowering of the pressure would lead to lower oxygen concentrations until the crucible decomposition line is intersected. Under these conditions, the crucible would start to decompose providing further oxygen and prevent additional lowering of the oxygen concentration in solution. Additional examination of the oxygen level can be effected by considering the simultaneous role of carbon in this process. This analysis is presented in Section B.1.7.

#### B.1.7 Consideration of the Simultaneous Reaction of Carbon and Oxygen in Liquid Silicon

Since the analysis of Section B.1.5 established that CO will be the dominant vapor species in the oxidation of carbon it is of interest to consider the reaction



where  $\underline{C}$  and  $\underline{O}$  refer to carbon and oxygen dissolved in silicon. In order to evaluate the free energy change for the reaction in Equation 10 between carbon as graphite at one atmosphere and  $\underline{C}$  (dissolved in silicon). This difference has been assessed as  $-12700 + 9.5T + RT \ln N$  where N is the atom fraction of carbon in solution in silicon. Utilization of the data in Table B along with the fact that the equilibrium in Equation (10) requires equal number of carbon and oxygen in solution (for equilibration with CO) leads to the following result

$$\log p(CO) \text{ (torr)} N^2 = 15.45 - 15390T^{-1} \quad (11)$$

where N is the atomic fraction of oxygen or carbon. At

$$T = 1710^{\circ} \text{ K}$$

$$P (\text{CO}) \text{ torr} = 2.8 \times 10^6 N^2 \quad (12)$$

If  $P = 0.028 \text{ torr}$  then  $N = 10^{-4}$  or  $5 \times 10^{18} \text{ atoms/cm}^3$ .

Note that this pressure lies below the crucible decomposition line in Figure B-1.

#### B.1.8      Detailed Calculation of the Rate of Evaporation of Silicon Monoxide

The previous consideration of reactions between liquid silicon and silica yielded the following equations for the equilibrium vapor pressure of silicon monoxide arising from the reaction:



$$\begin{aligned} \log p (\text{SiO}) \text{ torr} &= 11.47 - 17900T^{-1} \\ \log p (\text{SiO}) \text{ atm.} &= 8.58 - 17900T^{-1} \end{aligned} \quad (3)$$

At  $1712^{\circ}\text{K}$  (i.e.  $25^{\circ}\text{C}$  above the melting point of silicon) Equation (3) yields an equilibrium vapor pressure of  $1.31 \times 10^{-2} \text{ atm}$  or about 10 torr. In order to calculate the rate of Langmuir vaporization of silicon monoxide into a vacuum one can apply Equation (13) to compute the rate  $W$  in units of  $\text{gms/cm}^2 \text{ sec.}$

$$W (\text{gms/cm}^2 \text{ sec.}) = 44.4 p (\text{atm}) M^{\frac{1}{2}} (\text{SiO}) T^{-\frac{1}{2}} \quad (13)$$

where  $M (\text{SiO})$ , the molecular weight of silicon monoxide in grams is equal to 44, and  $T$  is the absolute temperature in Kelvins. Equation (13) yields an equilibrium rate of vaporization of  $0.092 \text{ gms/cm}^2 \text{ sec.}$  under these conditions.

B.1.9 Comparison of the Calculated Rate with the Rate  
Observed During a Crystal Growth Experiment

In an experiment conducted at Crystal Systems, a 2500 gm weight of silicon was melted in a cylindrical clear silica crucible with a six-inch (15.24 cm) diameter and a flat bottom. The melt was kept at heat for about 24 hours at a pressure of about 0.5 torr and 1712°K. After the exposure, measurement of the crucible wall disclosed a uniform corrosion of about 0.04 cm.

Allowing for the thermal expansion of silicon to the melting point and a volume contraction of  $1.4 \text{ cm}^3/\text{g. at.}$  on melting the volume of the silicon at the melting point is approximately  $938 \text{ cm}^3$ . This volume suggests that the liquid cylinder in the silica crucible was 5.12 cm high (and 15.24 cm in diameter). The surface area of contact between the silicon melt and the silica crucible is  $427 \text{ cm}^2$  composed of  $182 \text{ cm}^2$  along the bottom and  $245 \text{ cm}^2$  along the vertical walls.

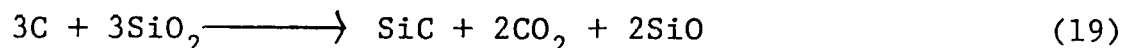
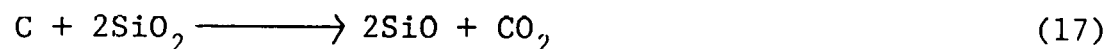
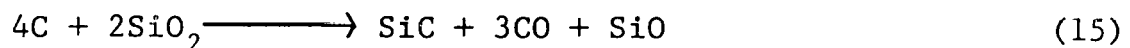
The 0.04 cm wall recession translates into a total volume recession of  $0.04 \times 427$  or  $17 \text{ cm}^3$  of silica. Since the density of silica ( $\text{SiO}_2$ ) is  $2.65 \text{ gms/cm}^3$  the mass recession is equal to 45 gms. The reaction stoichiometry of Equation (1) demands that 88 gms of  $\text{SiO}$  be liberated for every 60 gms of  $\text{SiO}_2$  consumed. Thus, the consumption of 45 gms of silica would lead to evaluation of 66 gms of  $\text{SiO}$ .

If one treats the entire surface area of the melt ( $182 \text{ cm}^2$ ) as the area through which  $\text{SiO}$  vaporizes then the vaporization

rate is  $66 \text{ gms}/182 \text{ cm}^2 \times 86400 \text{ seconds}$  or  $4.2 \times 10^{-6} \text{ gms/cm}^2 \text{ sec.}$  This estimate depends on the nucleation of  $\text{SiO}$  bubbles at the silicon/silica wall and rapid migration to the melt surface. The observed evaporation rate is thus  $0.042 \times 10^{-4} \text{ gms/cm}^2 \text{ sec.}$  which is more than 20,000 times slower than the calculated equilibrium evaporation rate.

#### B.1.10 Consideration of Reactions between Graphite and Silica Crucible

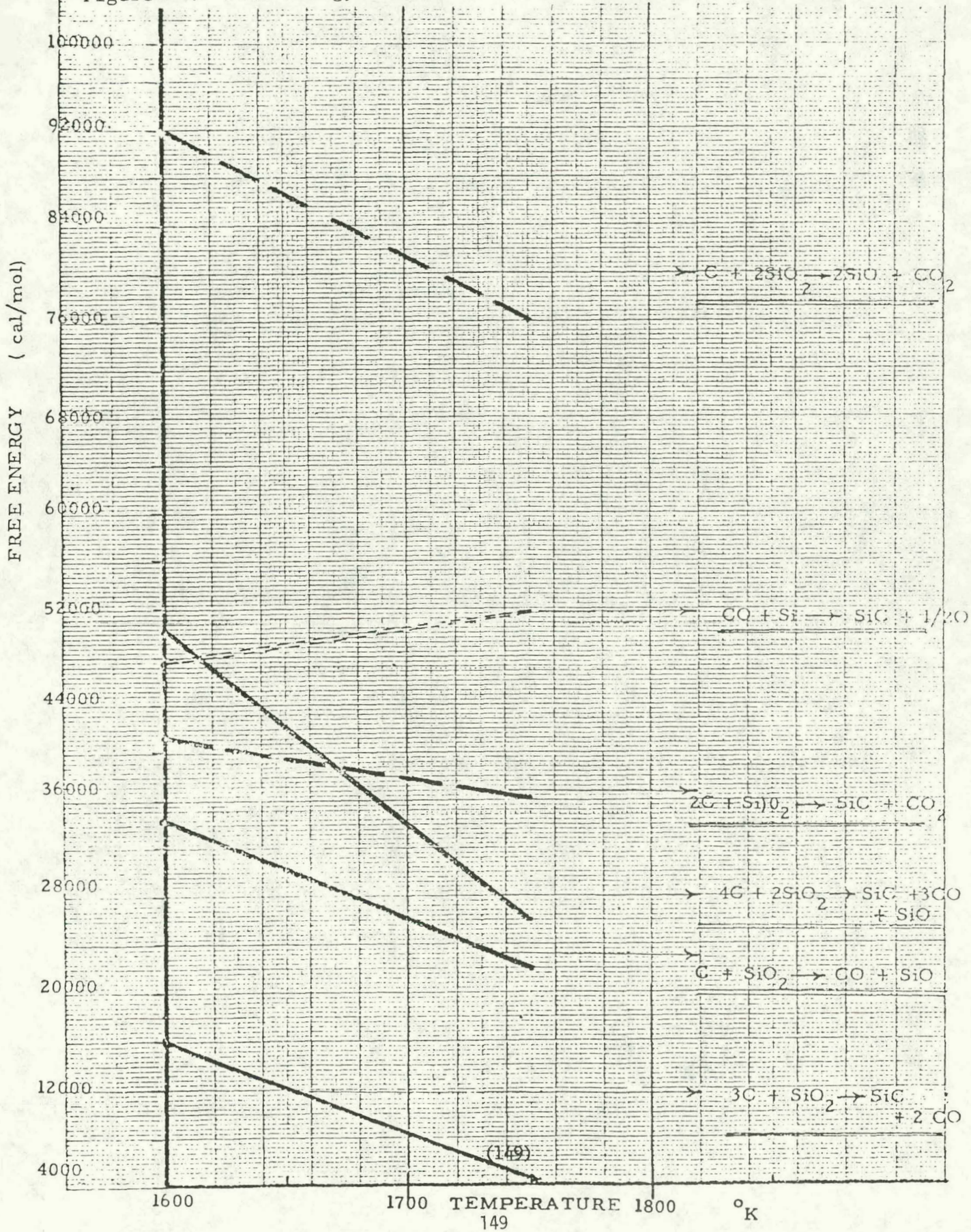
Following reactions between graphite and silica crucible were studied.

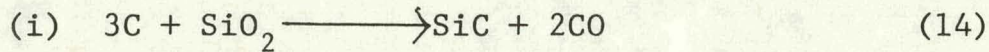


All the reactions have positive free energies at atmospheric pressure, as shown in Figure B-4 with those reactions that produce  $\text{CO}_2$  being the most positive.

Two reactions given by equations (14) and (16) gave the least positive free energies at atmospheric pressure. These were studied as a function of pressure and temperature:

Figure B-4. Free Energy of Various Reactions as a Function of Temperature





$$\Delta G = \Delta G^\circ + RT \ln p_{CO}^2$$

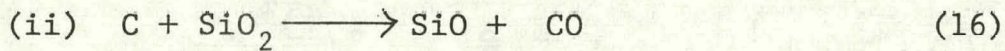
$$\Delta G^\circ = 143500 - 80T \quad (\text{Using data in Table B.})$$

Hence  $\Delta G = 143500 - 80T + (4.575) (2) \log p_{CO} \text{ (atm)}$

$$\Delta G = 0 \quad \text{so that}$$

$$\log p_{CO} \text{ (atm)} = 8.74 - 1.57 \times 10^4/T \quad (20)$$

Figure B-5 shows the regions of stability of this reaction as a function of pressure and temperature.



$$\Delta G = \Delta G^\circ + RT \ln (p_{SiO}) (p_{CO})$$

$$\Delta G^\circ = 162900 - 81T \quad (\text{using data in Table B.})$$

$$\frac{1}{2}p = p_{SiO} = p_{CO}$$

$$\Delta G = \Delta G^\circ + RT \ln (p/2)$$

$$\Delta G = 0 \quad \text{so that}$$

$$\log p \text{ (atm)} = 9.15 - 1.78 \times 10^4/T$$

$$\log p \text{ (torr)} = 12.03 - 178 \times 10^4/T \quad (21)$$

The range of stability of this reaction is also shown in Figure B-5.

Reaction (14) shows that SiC is formed by the reaction of carbon and silica but it does not explain how SiC is found in silicon. A common feature of reactions (14) and (16) is that under experimental conditions CO is the common stable species.

All data obtained from these studies of interaction of graphite with the silica crucible indicates that the SiC is not

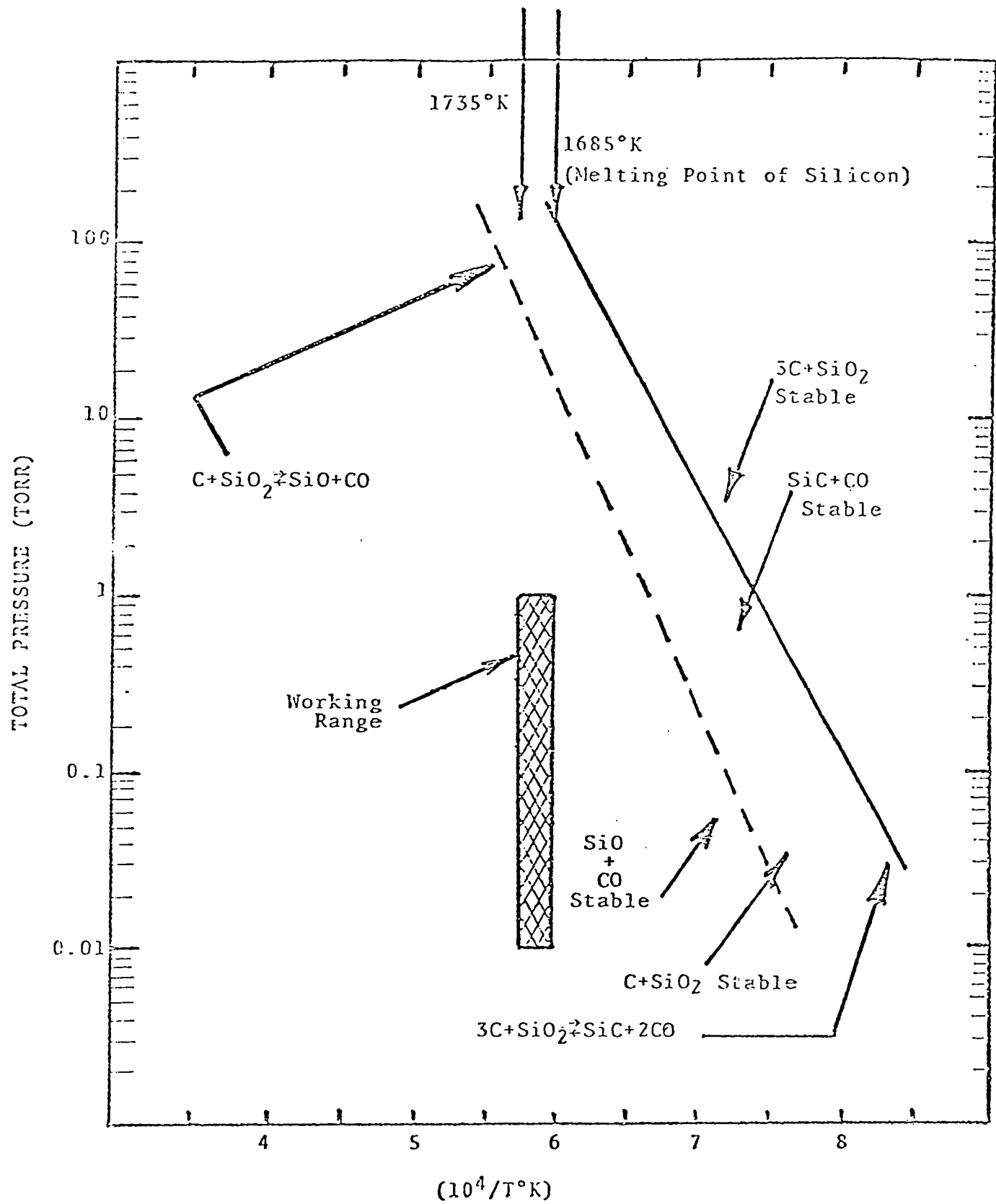
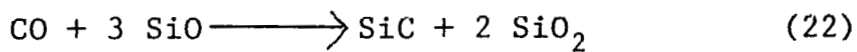


Figure B-5. Calculated Pressure-Temperature Relations for Reaction of Graphite and Silica to form Silicon Carbide, Silicon Monoxide and Carbon Monoxide.

formed in silicon because of these reactions. However, there is experimental evidence to show that silicon carbide is formed during the casting of silicon by the Heat Exchanger Method (HEM). Other possibilities could be the interaction of the by-products of the feasible reactions with themselves, or silicon. These reactions are analyzed in the following section.

B.1.11 Consideration of Reaction between CO and C with SiO

(i) The following reaction was studied:



$$\Delta G = \Delta G^\circ - RT \ln (p_{CO}) (p_{SiO})^3$$

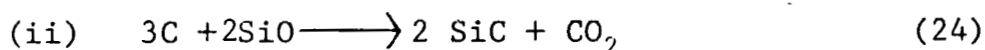
$$\Delta G^\circ = - 345,200 + 163T \text{ (using data in Table B.)}$$

$$P_t = p_{CO} + p_{SiO}; p_{CO} = (1/3) p_{SiO}$$

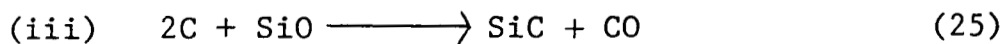
$$\log P_t \text{ (torr)} = 12.04 - 10.89 \times 10^4 / T \quad (23)$$

The regions of stability of this reaction are shown in Figure B-6.

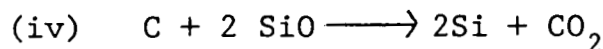
It can be seen that under the operating experimental conditions this reaction does not proceed to the right.



Reaction has a negative free energy at 1 atm, - 9818 cal/mole at 1600 K to -3720 cal/mole at 1750 K.



Reaction has a negative free energy at 1 atm -17977 cal/mole at 1600 K to -17783 cal/mole at 1750 K.



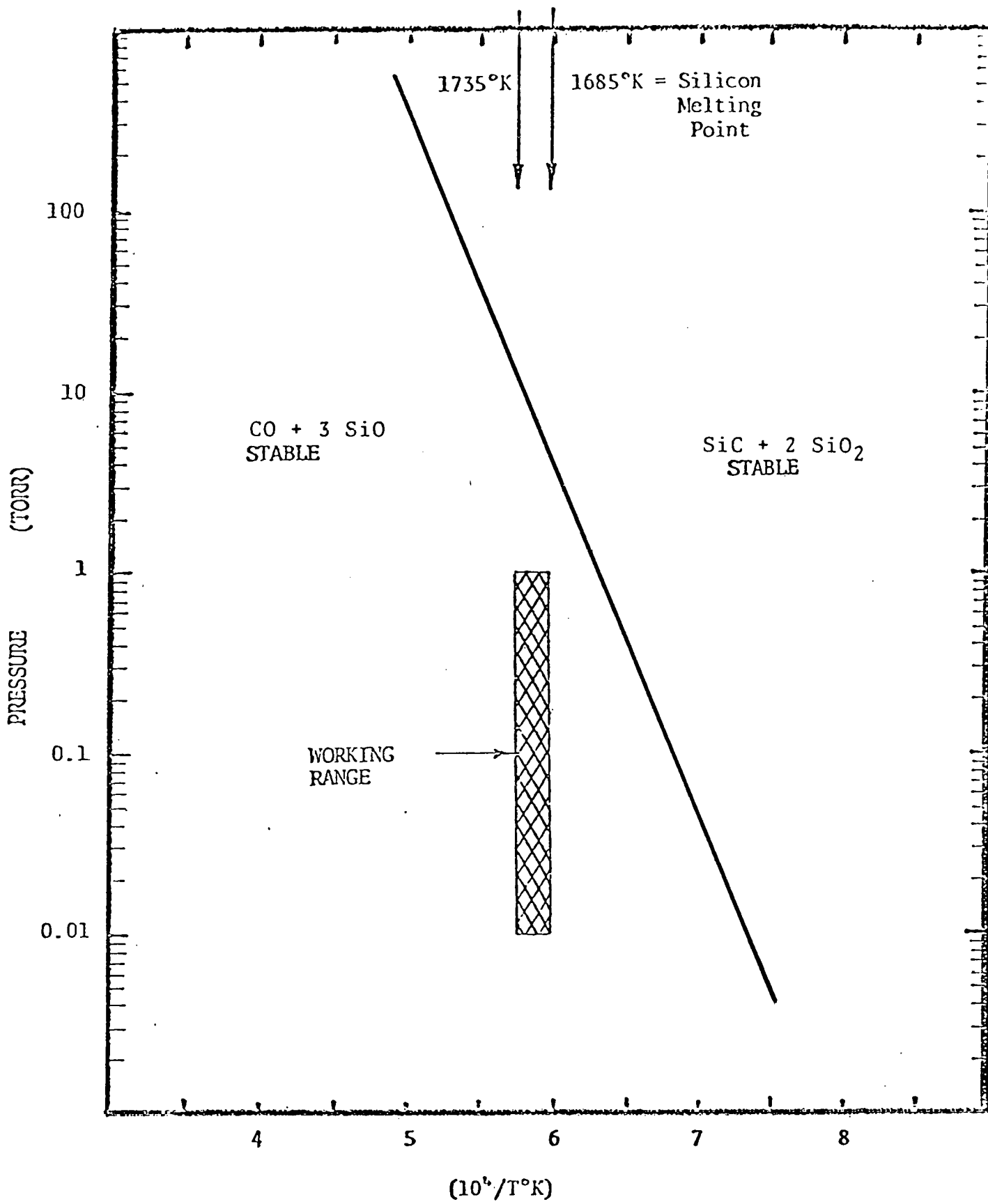


Figure B-6. Equilibrium Total Pressure of CO and SiO as a Function of Temperature for the Reaction;  
 $\text{CO} + 3 \text{SiO} \rightarrow \text{SiC} + 2 \text{SiO}_2$

Reaction has a positive free energy at 1 atm

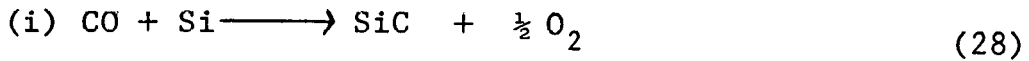
+16035 cal/mole at 1600 K to +20643 cal/mole at 1750 K



Reaction has a negative free energy - 4870 cal/mole at 1600 K to -5602 cal/mole at 1750 K.

#### B.1.12 Consideration of Reaction between CO or CO<sub>2</sub> with Silicon

A number of reactions involving CO and CO<sub>2</sub> were studied.



This reaction yields positive free energy at atmospheric pressure and is shown in Figure . It should be noted that the slope of energy vs. temperature for this reaction is positive as contrasted to the negative slopes for other reactions in Figure

Calculations were made using pressure as a variable.

$$\Delta G = \Delta G^\circ + RT \ln \frac{P_{O_2}^{1/2}}{P_{CO}}$$

$$\Delta G^\circ = 10100 + 23T \text{ (using data in Table B)}$$

$$4.575 \log \frac{P_{O_2}^{1/2}}{P_{CO}} = -10100 - 23T$$

At T ≈ 1700 K

$$\frac{P_{O_2}^{1/2}}{P_{CO}} = 4.68 \times 10^{-7}$$

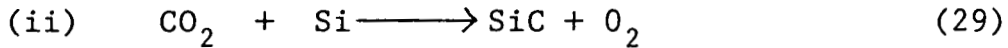
$$P_{O_2} + P_{CO} = 1$$

$$\text{let } x^2 = P_{O_2}; x = P_{O_2}^{1/2} \text{ and } P_{CO} = 1 - x^2$$

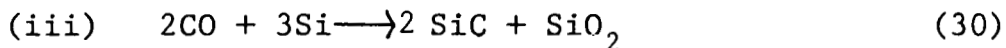
$$\frac{x}{1 - x^2} = 4.68 \times 10^{-7}$$

$$P_{O_2}^{1/2} \sim 4.68 \times 10^{-7}$$

Even if the total pressure is reduced to  $10^{-4}$  atm = 0.076 torr, this reaction will not proceed at 1700 K.



Reaction has positive free energy of 81875 cal/mole at 1600° K to 82633 cal/mole at 1750 K.

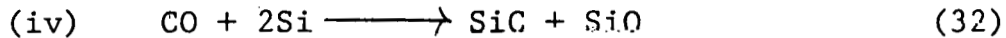


$\Delta G^\circ = -198100 + 89T$  (reaction proceeds to the right at 1 atm and 1700 K)

$$\Delta G = \Delta G^\circ - RT \log p_{\text{CO}}$$

$$\log p_{\text{CO}} \text{ (torr)} = 12.6 - 2.17 \times 10^4 / T \quad (31)$$

The stability range of this reaction is shown in Figure B-7. Under the working range the reactants are stable.



$\Delta G^\circ = -17000 + 5.0 T$  (reaction proceeds to the right at 1700 K)

$$\Delta G = -17000 + 5.0 T + 4.575 T \log \frac{p_{\text{SiO}}}{p_{\text{CO}}}$$

$$P_{\text{total}} = p_t = p_{\text{SiO}} + p_{\text{CO}}; p_{\text{CO}} = (1-x)p_t;$$

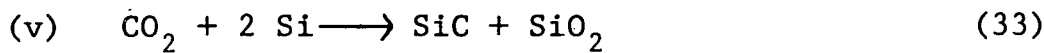
$$p_{\text{SiO}} = x p_t.$$

$$\Delta G = -17000 + 5.0 T + 4.575 T \log (x/1-x)$$

Reaction does not depend on pressure. The equilibrium fraction of SiO (i.e., x) is given by:

$$\exp \left\{ \frac{17000 - 5T}{1.987 T} \right\} \left\{ 1 + \exp \left\{ \frac{17000 - 5T}{1.987 T} \right\} \right\}^{-1} = x$$

T K	$x = p_{SiO}/p_t$	%CO	%SiO
1650	0.935	6.5	93.5
1687	0.928	7.2	92.8
1700	0.925	7.5	92.5
1750	0.915	8.5	91.5



$\Delta G^\circ = -47100 + 46.0T$  (reaction does not go to the right.  $\Delta G^\circ = 31100$  at 1700 K and 1 atm)

$$\Delta G = \Delta G^\circ - 4.575 T \log p_{CO_2}$$

$$\log p_{CO_2} \text{ (torr)} = 12.94 - 1.03 (10^4/T) \quad (34)$$

at  $T = 1687$ ;  $(10^4/T) = 5.92$

$$\log p_{CO_2} \text{ (torr)} = 6.84$$

$$\log p_{CO_2} \text{ (atm)} = 4; p_{CO_2} = 10 \text{ kilobars.}$$

Reaction does not go to the right and there is practically no pressure effect.

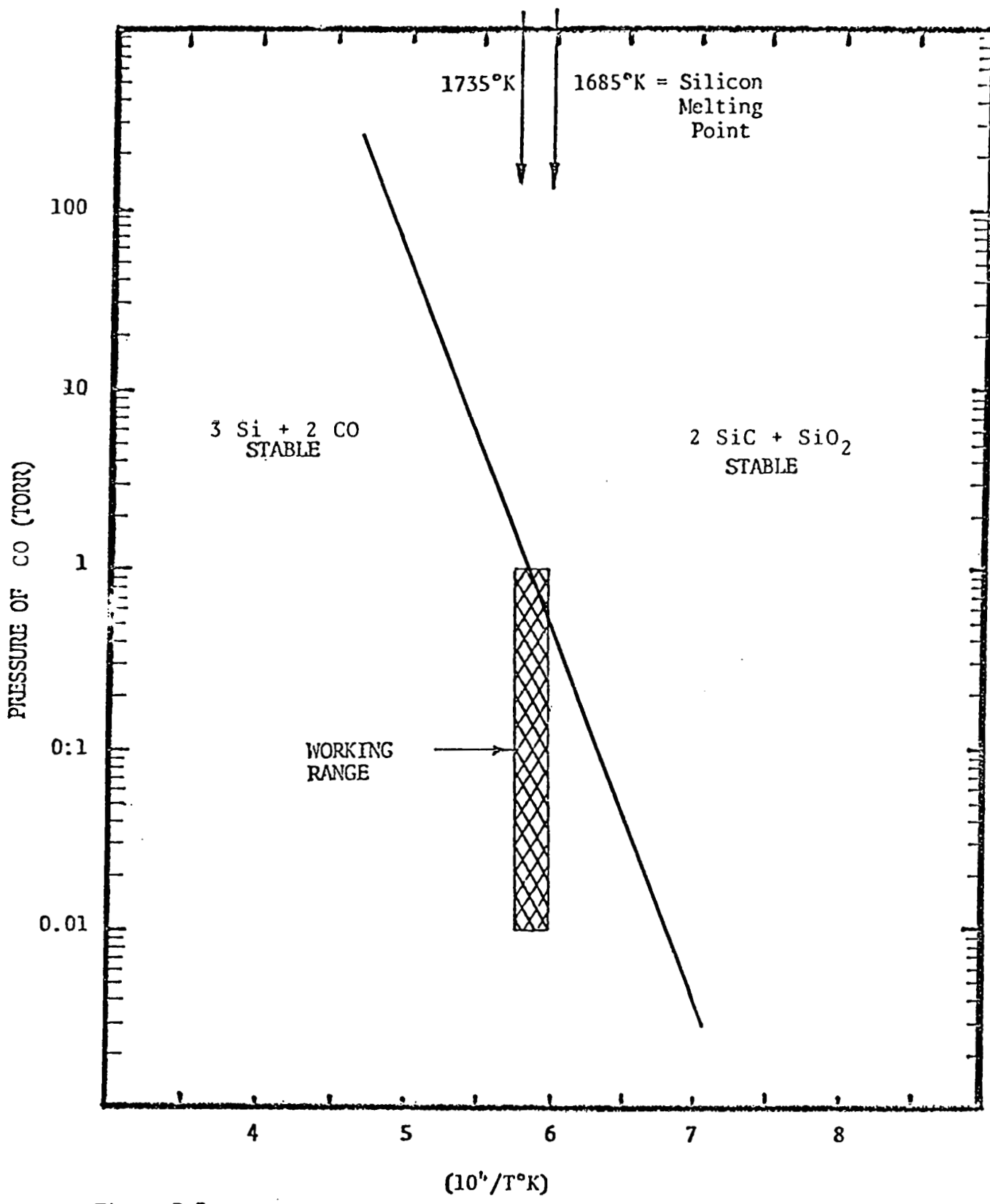
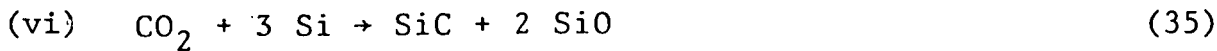


Figure B-7. Equilibrium Pressure of CO as a Function of Temperature for the reaction;  
 $2 \text{ CO} + 3 \text{ Si} \rightarrow 2 \text{ SiC} + \text{SiO}_2$



$\Delta G^\circ = +22300 - 3.3 T$  (reaction goes to the right at one atm and 1700K)

$$\Delta G = \Delta G^\circ + RT \ln \frac{p_{\text{SiO}}^2}{p_{\text{CO}_2}}$$

$$p_{\text{SiO}} = x p_t ; \quad p_{\text{CO}_2} = (1-x)p_t$$

$$\Delta G = 22300 - 46.2T + 4.575 T \log p(\text{torr}) + 4.575 T \log (x^2/(1-x))$$

at equilibrium  $\Delta G = 0$

$$\frac{\ln (x^2/(1-x)) = -22300 + 46.2 T - 4.575 T \log p(\text{torr})}{1.9873 T}$$

at  $T = 1700$  and  $-2 \leq \log p \leq 3$

$x^2 \rightarrow 1$ . Thus,

$$\frac{\ln (1-x) = 22300 + 4.575 T \log p_t(\text{torr}) - 46.2T}{1.9873 T}$$

$$x = \text{fraction SiO} = 1 - \exp \left[ \frac{22300 + 4.575 T \log p_t(\text{torr}) - 46.2T}{1.9873 T} \right]$$

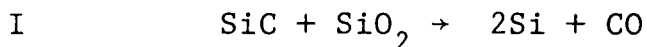
at 1687K

$$= 1 - \exp \left[ \frac{-55639 + 7718 \log p}{3353} \right]$$

<u>p(torr)</u>	<u>x</u>	<u>%SiO</u>
1	1.0	100%
10	-	-
100	-	-
1000	0.99994	99.994%

The reaction goes to the right and there is virtually no pressure effect.

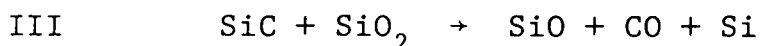
In order to avoid reaction between graphite crucible retainers and silica crucibles used in the melting of large ingots of silicon, efforts are being made to reduce the tendency to form CO or CO<sub>2</sub> gas which can contaminate the silicon at high temperatures. One method of attacking this problem is to coat the retainer with silicon carbide in order to form a barrier between silica and graphite and limit the reaction. This study examined the possible ranges of temperature and pressure on which a reaction between the silica and silicon carbide coating can occur. Five following reactions were studied:



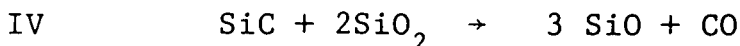
Result: Reaction will not go to the right  
in the working range.  
(See Figure B-8)



Result: Reaction will go to the right  
in the working range.  
(See Figure B-9)



Result: Reaction will go to the right  
in the working range.  
(See Figure B-10)



Result: Reaction will go to the right  
in the working range.  
(See Figure B-11)



Result: Reaction will go to the right  
in the working range.  
(See Figure B-12)

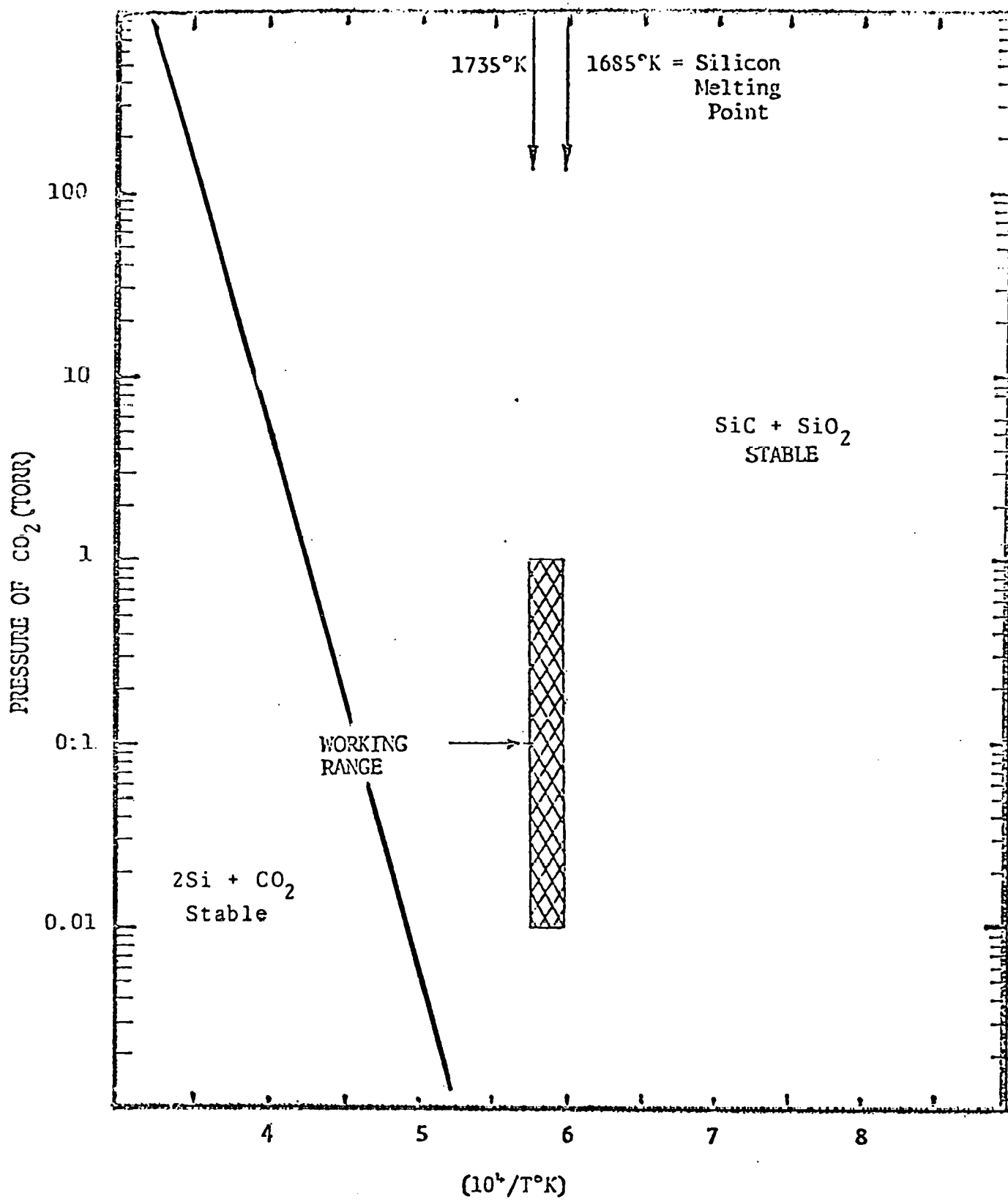


Figure B-8. Equilibrium Pressure of  $\text{CO}_2$  as a Function of Temperature for Reaction I;  
 $\text{SiC} + \text{SiO}_2 \rightarrow 2\text{Si} + \text{CO}_2$

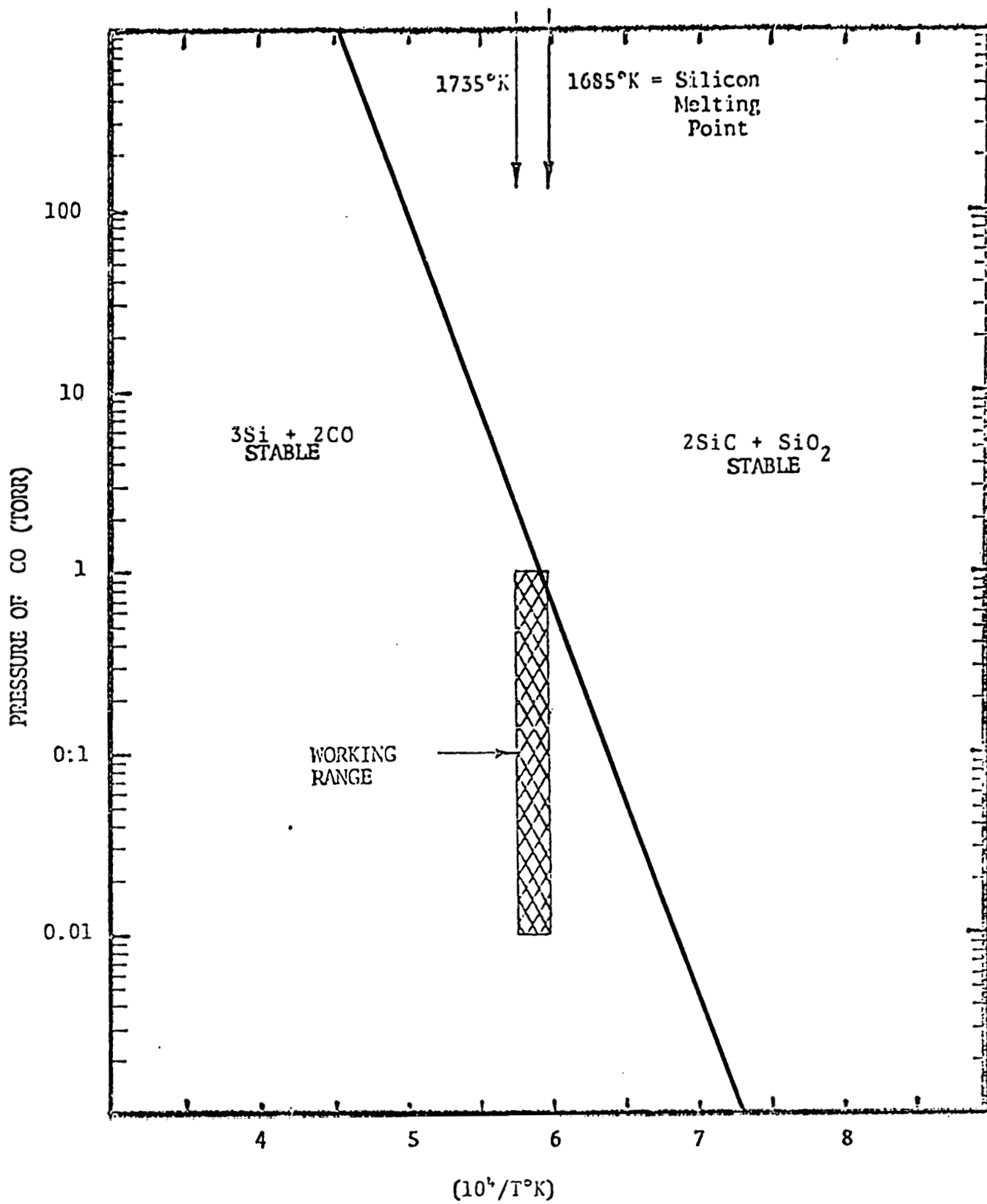
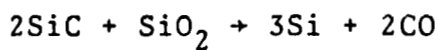


Figure B-9. Equilibrium Pressure of CO as a Function of Temperature for Reaction II;



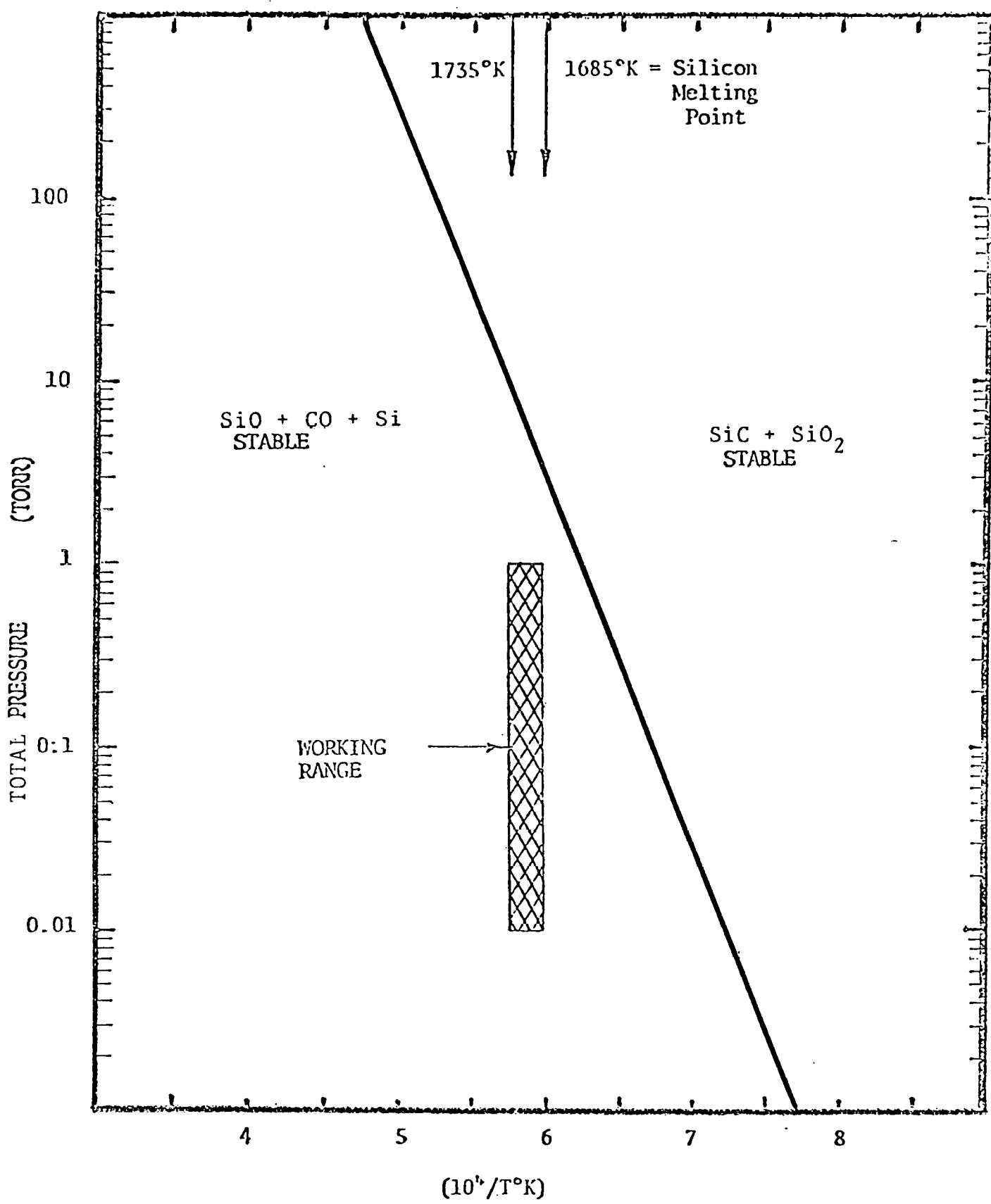
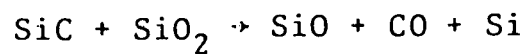


Figure B-10. Total Pressure of SiO and CO as a Function of Temperature for Reaction III;



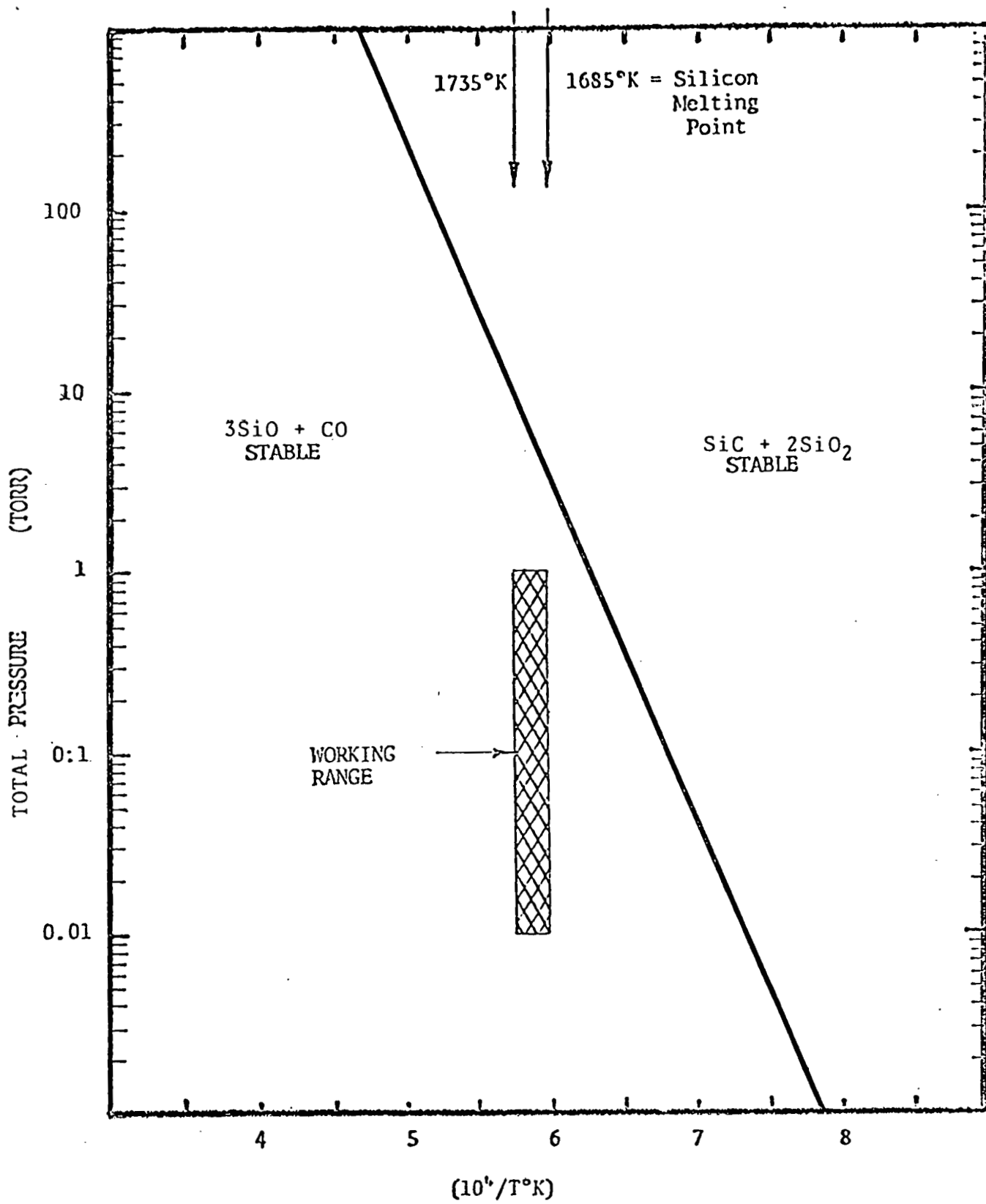


Figure B-11. Total Pressure of SiO and CO as a Function of Temperature for Reaction IV;  
 $\text{SiC} + 2\text{SiO}_2 \rightarrow 3\text{SiO} + \text{CO}$

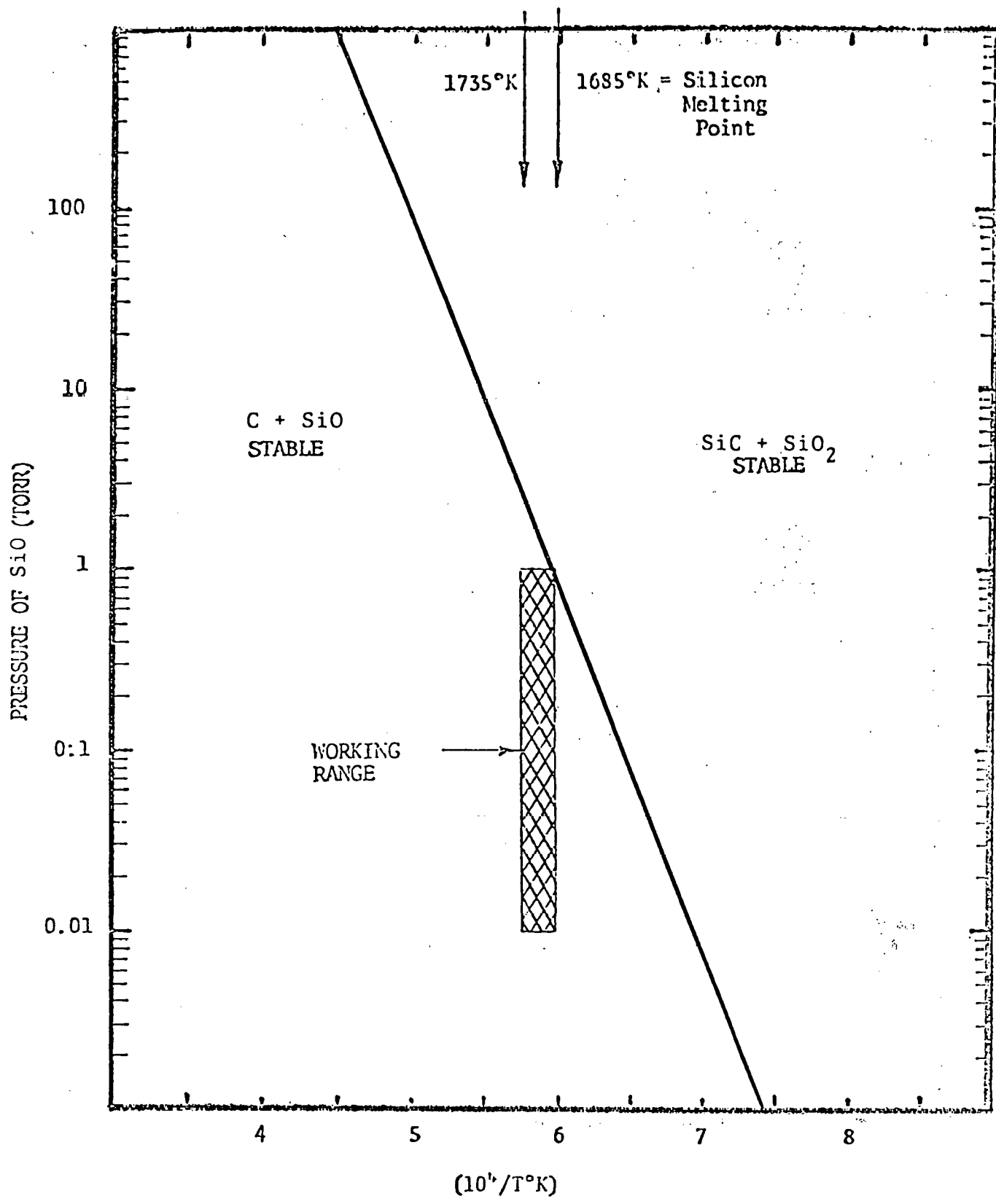
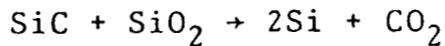


Figure B-12. Equilibrium Pressure of  $\text{SiO}$  as a Function of Temperature for Reaction V;  
 $\text{SiC} + \text{SiO}_2 + \text{C} + 2\text{SiO}$

### REACTION I



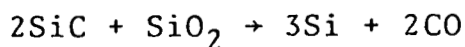
$$\Delta G^\circ = 141600 - 47.0T = 61700 \text{ (calories) at 1 atm., 1700K.}$$

(reaction does not proceed to the right  
at one atmosphere)

$$\Delta G = \Delta G^\circ + 4.575 T \log p_{\text{CO}_2} \text{ [atm]}$$

$$\log p_{\text{CO}_2} \text{ (torr)} = 13.15 - 3.09 (10^4/T) \text{ (Figure B-8)}$$

### REACTION II



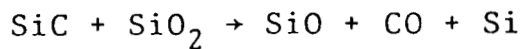
$$\Delta G^\circ = 199700 - 92.0T = 43300 \text{ (calories) at 1 atm., 1700K.}$$

(reaction does not proceed to the right  
at one atmosphere)

$$\Delta G = \Delta G^\circ + 4.575 T \log p_{\text{CO}}^2 \text{ [atm]}$$

$$\log p_{\text{CO}} \text{ (torr)} = 12.94 - 2.18 (10^4/T) \text{ (Figure B-9)}$$

### REACTION III



$$\Delta G^\circ = 181600 - 84.1T = 38630 \text{ (calories) at 1 atm., 1700K}$$

(reaction does not proceed to the right  
at one atmosphere).

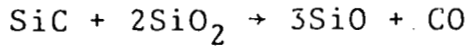
$$\Delta G = \Delta G^\circ + 4.575 T \log (p_{\text{SiO}}) (p_{\text{CO}})$$

$$p_{\text{SiO}} = p_{\text{CO}} = 1/2p_t \text{ (total pressure)}$$

$$\Delta G = \Delta G^\circ + 9.15 \log p_t \text{ [atm]} + 4.575 T \log 0.250$$

$$\log p_t \text{ (torr)} = 12.38 - 1.98 (10^4/T) \text{ (Figure B-10)}$$

#### REACTION IV



$\Delta G^\circ = 345100 - 160.3T = 72590$  (calories) at 1 atm., 1700K  
(reaction does not proceed to the right  
at one atmosphere).

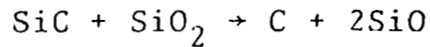
$$\Delta G = \Delta G^\circ + 4.575T \log (p_{\text{SiO}})^3 (p_{\text{CO}})$$

$$p_{\text{SiO}} = 3 p_{\text{CO}} ; p_t \text{ (total pressure)} = \frac{4}{3} p_{\text{SiO}}$$

$$\Delta G = \Delta G^\circ + 18.3T \log p_t + 4.575T \log n (27/256)$$

$$\log p_t \text{ (torr)} = 11.84 - 1.89 (10^4/T) \quad (\text{Figure B-11})$$

#### REACTION V



$\Delta G = 181500 - 80.2T = 45160$  (calories) at 1 atm., 1700K  
(reaction does not proceed to  
the right at one atmosphere)

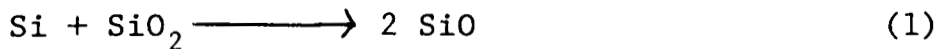
$$\Delta G = \Delta G^\circ + 4.575T \log p_{\text{SiO}}^2$$

$$\log p_t \text{ (torr)} = 11.64 - 1.98 (10^4/T) \quad (\text{Figure B-12})$$

Reactions I - V shown above have been examined. Figures B-8 through B-12 and the analysis above shows that for four of the five reactions examined (i.e., II - V) a reaction between the silicon carbide coating and the silica crucible will occur in the present working range. However, this reaction can be suppressed by operating at slightly higher pressures. This will introduce complications in heat transfer and will introduce extra costs. Another solution to the above problem is to develop a free-standing crucible. The sintered graded crucibles developed are quite thick and can be eventually made free standing. In the absence of the graphite retainers, the silicon carbide impurities will not be formed in silicon.

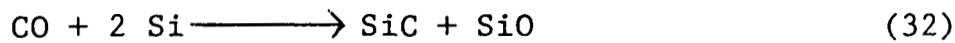
### B.3 Conclusions

1. Silicon monoxide is formed by the silicon-silica reaction



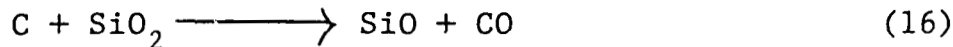
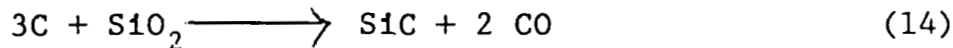
At the melting point of silicon SiO is volatile. This reaction could result in decomposition of the crucible; however, experimental evidence indicates that the reaction rate is about 20,000 times slower than the calculated equilibrium evaporation rate.

2. Silicon carbide is probably formed predominately by the reaction of carbon monoxide and silicon:



The source of CO is from the graphite retainers used to support the crucible.

3. The CO is due to the reaction of the crucible and the graphite retainers; viz.,



The furnace parts although made of graphite have been coated with silicon carbide and do not contribute to the formation of silicon carbide in the melt.

4. Even silicon carbide coated graphite retainers in contact with silica crucibles will not prevent the evolution of CO.

APPENDIX C  
THE EFFECTS OF WIRE TENSION AND MODULUS  
OF ELASTICITY ON DEFLECTION

Case 1. Tungsten Core Wire

Young's Modulus,  $E = 50 \times 10^6$  psi <sup>(32)</sup> (Table VIII)

Yield stress =  $3.125 \times 10^5$  psi

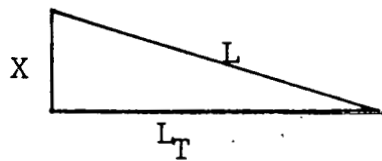
The blade pack is tensioned to 80% of yield stress,

$$\sigma_T = 2.5 \times 10^5 \text{ psi}$$

$$F_T = 2.5 \times 10^5 \times 1.96 \times 10^{-5} = 4.9 \text{ lb}$$

$$\begin{aligned} \text{Strain due to tension, } \epsilon_T &= \frac{\sigma_T}{E} \\ &= \frac{2.5 \times 10^5}{500 \times 10^5} \\ &= 0.005 \text{ in/in} \end{aligned}$$

The wires are about 16 inches long. When feed forces are applied, there is a deflection in the wires. The support rollers, 4 inches apart, limit the deflection to the length between the rollers. The feed force can be assumed to be applied vertically between the support rollers. The exaggerated deflection is shown in the strain diagram.



Strain Diagram

$L_T$  = Tensioned length from support roller to center of workpiece

$$\begin{aligned} &= L_i + L_i \epsilon_T \\ &= 2 + 2 \times 0.005 \\ &= 2.010 \text{ in.} \end{aligned}$$

If 0.1 lb feed force is applied per wire ( $F_F$ )  
the total force on the wire (from force diagram),

$$\begin{aligned} F &= \sqrt{F_T^2 + F_F^2} \\ &= \sqrt{(4.9)^2 + (0.1)^2} \\ &= 4.901 \end{aligned}$$

$$\begin{aligned} \text{Final strain, } \epsilon_f &= \frac{\rightarrow}{AE} = \frac{4.901}{1.96 \times 10^{-5} \times 500 \times 10^5} \\ &= 5.001 \times 10^{-3} \text{ in/in} \\ L &= 2 + 5.001 \times 10^{-3} \times 2 \\ &= 2.010002 \text{ in.} \end{aligned}$$

$$\begin{aligned} \text{Deflection of wire, } x &= \sqrt{L^2 - L_T^2} \\ &= 0.0028 \text{ in.} \end{aligned}$$

Case 2. Piano Wire

Stainless steel wire,  $E = 30 \times 10^6$  psi<sup>(33)</sup>

Y.S. =  $4.25 \times 10^5$  psi (Table VIII)

$$\sigma_T = 0.8 \times 4.25 \times 10^5 = 3.4 \times 10^5 \text{ psi}$$

$$F_T = \sigma_T \times A = 6.664 \text{ lb}$$

$$\epsilon_T = \frac{\sigma_T}{E} = 0.01133 \text{ in/in}$$

$$L_T = 2 + 2 \times 0.01133 \\ = 2.022667 \text{ in.}$$

$$F_F = 0.1 \text{ lb.}$$

$$\vec{F} = (6.664)^2 + (0.1)^2$$

$$= 6.6648$$

$$\epsilon_f = \frac{\vec{F}}{AE}$$

$$= 11.335 \times 10^{-3} \times 2 \\ = 2.02267 \text{ in}$$

$$\text{Deflection, } x = \sqrt{L^2 - L_T^2} \\ = 0.0035 \text{ in.}$$

## APPENDIX D. MECHANICAL PROPERTY TEST DATA FOR TUNGSTEN, STAINLESS STEEL, AND STEEL WIRE

Wire Number	Diameter		Material	x10-5 Area	Elastic Limit psi	0.2% Yield psi	Ultimate psi	Comments
	Mil	mm						
172	1	5	0.125	Tungsten	1.96	255,102	336,734	-
	2	5	0.125	Tungsten	1.96	239,795	336,734	-
	3	5	0.125	Tungsten	1.96	255,102	340,306	6" Gage Length
	4	5	0.125	Tungsten	1.96	260,200	341,326	384,183
	5	5	0.125	Tungsten	1.95	219,387	340,306	383,673
	6	5	0.125	Tungsten	1.95	214,285	319,897	334,200
	7	5	0.125	Tungsten	1.95	239,795	341,180	386,224
	8	5	0.125	Tungsten	1.95	229,590	341,840	-
	9	5	0.125	Tungsten	1.95	219,390	341,840	385,200
	10	5	0.125	Tungsten	1.96	232,140	341,840	364,806
	11	5	0.125	Tungsten	1.96	331,630	395,460	-
	12	6.5	0.162	Copper Plated on Tungsten	1.96	295,900	340,800	385,000

## APPENDIX D. MECHANICAL PROPERTY TEST DATA FOR TUNGSTEN, STAINLESS STEEL, AND STEEL WIRE (cont.)

Wire Number	Diameter		Material	x10-5 Area	Elastic Limit psi	0.2% Yield psi	Ultimate psi	Comments	
	Mil	mm							
173	13	6.5	0.162	Copper Plated on Tungsten	1.96	295,900	340,300	383,000	0.75 mil Nickel Plated on 5 mil Tungsten
	14	6.5	0.162	Copper Plated on Tungsten	1.96	306,100	346,900	384,000	0.75 mil Nickel Plated on 5 mil Tungsten
	15	6.5	0.162	Nickel Plate on Tungsten	1.96		333,333	400,933	0.75 mil Nickel Plated on 5 mil Tungsten
	16	6.5	0.162	Nickel Plate on Tungsten	1.96		351,954	426,851	0.75 mil Nickel Plated on 5 mil Tungsten
	17	6.5	0.125	Nickel Plated Tungsten	1.96		290,116	348,377	Annealed at 500°C to Soften 0.75 mil Nickel Plated on 5 mil Tungsten
	18	6.5	0.125	Nickel Plated Tungsten	1.96		297,250	356,700	Annealed at 500°C to Soften 0.75 mil Nickel Plated on 5 mil Tungsten
	19	3.0	0.125	Tungsten	1.96		375,000	509,000	Plain 3 mil Tungsten
	20	3.0	0.075	Tungsten	1.96		326,000	417,000	Plain 3 mil Tungsten
	21	3.0	0.075	Tungsten	1.96		339,000	419,000	Plain 3 mil Tungsten

APPENDIX D. MECHANICAL PROPERTY TEST DATA FOR TUNGSTEN, STAINLESS STEEL, AND STEEL WIRE (cont.)

Wire Number	Diameter		Material	x10-5 Area	Elastic Limit psi	0.2% Yield psi	Ultimate psi	Comments
	Mil	mm						
22	3.0	0.075	Tungsten	1.96		381,000	512,000	Plain 3 mil Tungsten
23	4.0	0.1	Nickel Plated Tungsten	1.96		460,000	574,000	0.5 mil Nickel Plated on 3 mil Tungsten Wire
24	4.0	0.1	Nickel Plated Tungsten	1.96			569,000	0.5 mil Nickel Plated on 3 mil Tungsten Wire
25	8.0	0.2	Copper Plated Stainless Steel	1.96		428,000	483,000	1.5 mil Copper Plated on 5 mil Stainless Steel Diamond Impregnated
26	8.0	0.2	Copper Plated Stainless Steel	1.96		460,000	480,000	1.5 mil Copper Plated on 5 mil Stainless Steel Diamond Impregnated
27	0.5	0.125	Copper Plated Stainless Steel	1.96	512,000	563,000	572,000	0.5 mil Copper Plated on 4 mil Stainless Steel Wire
28	0.5	0.125	Copper Plated Stainless Steel	1.96	530,000	552,000	567,000	0.5 mil Copper Plated on 4 mil Stainless Steel Wire
29	0.5	0.125	Copper Plated Stainless Steel	1.96	503,000	554,000	567,000	0.5 mil Copper Plated on 4 mil Stainless Steel Wire

## APPENDIX D. MECHANICAL PROPERTY TEST DATA FOR TUNGSTEN, STAINLESS STEEL, AND STEEL WIRE (cont.)

Wire Number	Diameter		Material	x10-5 Area	Elastic Limit psi	0.2% Yield psi	Ultimate psi	Comments
	Mil	mm						
30	5.6	0.14	Steel	1.96		430,500	515,800	Music Wire Used by GEOS
31	5.6	0.14	Steel	1.96		426,500	515,800	Music Wire Used by GEOS
32	5.6	0.14	Steel	1.96		422,400	515,800	Music Wire Used by GEOS
33	5.6	0.14	Steel	1.96		426,500	515,800	Music Wire Used by GEOS

APPENDIX E. SILICON SLICING SUMMARY

RUN	PURPOSE	FEED FORCE/BLADE		AVERAGE CUTTING RATE		WIRE TYPE	REMARKS
		lb.	gm	mil/min	mm/min		
1	First test of machine and blade	0.1 to 0.15	45 to 70	N/A		45 $\mu$ m diamond impregnated into 1.5 mil copper sheath on 5 mil stainless steel core	Cutting terminated due to wander.
2	Cutting rate	0.1 to 0.2	45 to 90	2 to 5	0.05 to 0.13	Same wire.	Good cutting, severe wander.
3	Life test	0.15	68	1.5	0.0375	Same wire.	Poor cutting after run 2.
4	Life test	0.15	68	1.0	0.01	Same wire.	Low diamond concentration.
5	Cutting effectiveness rate and wander	0.15	65	N/A	N/A	45 $\mu$ m diamond impregnated in soft 8 mil stainless steel	Severe wander.
6	Diamond charging		N/A		N/A	45 $\mu$ m diamond impregnated into 1.5 mil copper coating on 5 mil stainless steel wire	Non-uniform charging.
7	Cutting effectiveness of higher concentration of impregnated diamond	0.15	68	1.5	0.0375	45 $\mu$ m diamond double impregnated into 1.5 mil copper coating on 5 mil stainless steel wire	Much slower degradation in cutting rate.

APPENDIX E. SILICON SLICING SUMMARY (cont.)

RUN	PURPOSE	FEED FORCE/BLADE		AVERAGE CUTTING RATE		WIRE TYPE	REMARKS
		1b.	gm	mil/min	mm/min		
8	Reduce wander by using wire restraints			2	0.05	Same as for run 7.	No reduction in wander by using restraints at end of wire.
9	Abrasive life			0.5	0.0125	Same as for run 8.	Cutting rate decreased to 20% of run #8. Run terminated.
10	Determine if blade loading causing poor cutting.			0.5	0.0125	Same wire.	Cutting rate could not be restored by cleaning and soaking wires.
11	Charging			N/A		Same wire.	Non-uniform impregnation led to poor cutting rates.
12	Measure effects of blade wander with support rollers in position.	.15	68	1.5	.038	Double impregnated 45 $\mu$ m diamond in copper plated .2 mm $\varnothing$ wire	Run aborted midway due to low cutting rates.
13	Continuation of run 12 with new wires.	.15 .20	68 90	1.5 2-3	.038 .07	Double impregnated 45 $\mu$ m diamond in copper plated .2 mm $\varnothing$ wire	Rollers show significant improvement in blade wander. Damage at wire pack change.
14	Test Nickel-Diamond plated stainless steel wires.	.15	68	2.0	.05	400-mesh diamond nickel plated on .2 mm $\varnothing$ stainless steel wire	Wire breakage due to hydrogen embrittlement.

## APPENDIX E. SILICON SLICING SUMMARY (cont.)

RUN	PURPOSE	FEED		AVERAGE		WIRE TYPE	REMARKS
		FORCE/BLADE lb.	gm	CUTTING RATE mil/min	mm/min		
15	Test cutting dry.					Double impregnated 45 $\mu$ m diamond in copper plated .2 mm $\emptyset$ wire	Loading observed. Further testing necessary.
16	Test run without rocking workpiece.	.3	136	2-2.5	.05	Double impregnated 45 $\mu$ m diamond in copper plated .2 mm $\emptyset$ wire	Twice normal feed forces were required to achieve usual cutting rates. Wafer surface quality poor.
17	Test effects of slow non-synchronous rocking of workpiece $\frac{1}{2}$ cycle/minute.	.2	90	2-3	.06	Double impregnated 45 $\mu$ m diamond in copper plated .2 mm $\emptyset$ wire.	Very good surface quality and good cutting rates maintained throughout run.
18-S	First run using DiNi plated tungsten.	.2	90	6.6	.17	400 mesh diamond nickel plated on .127 mm tungsten wire.	Cutting rates dropped to 2.5 mils/min at the end of this run.
19-S	Determine cause of cutting rate decrease.	.2	90	2.5	.06	Same wire.	This run was aborted midway through due to low cutting rates.
20-S	Wires used in runs 18-S and 19-S turned upside down.	.2	90	5.9	.15	Same wire.	Good cutting rates until contact was made with glass mounting block, again dropping to 2.0 mil/min.

APPENDIX E. SILICON SLICING SUMMARY (cont.)

RUN	PURPOSE	FEED FORCE/BLADE		AVERAGE CUTTING RATE		WIRE TYPE	REMARKS
		lb.	gm	mil/min	mm/min		
21-S	Isolate cause of cutting rate decrease at completion of runs. Change mounting block to graphite.	.2	90	2.75	.07	Same wire.	Wire dressing with an aluminum oxide dressing stick. Cutting rates increased and also increased with contact in graphite.
22-S	Life test of wires and effects of dressing.	.2	90	3.9	.10	Same wire.	Good cutting rates and wafer quality.
23-S	Life test.	.2	90	4.1	.10	Same wire.	Light dressing prior to run.
24-S	Life test.	.2	90	3.5	.09	Same wire.	Slight decrease in cutting rates.
25-S	Life test.	.2	90	3.7	.09	Same wire.	Cutting rate seems to be stabilizing.
26-S	Life test.	.2	90	3.6	.09	Same wire.	Amount of dressing and feed force are critical.
27-S	Life test.	.2	90	3.7	.09	Same wire.	Wafer thickness may be changing due to support roller degradation.
28-S	Life test.	.2	90	3.6	.09	Same wire.	Very good wafer surface quality. No dressing prior to this run.

## APPENDIX E. SILICON SLICING SUMMARY (cont.)

RUN	PURPOSE	FEED FORCE/BLADE		AVERAGE CUTTING RATE		WIRE TYPE	REMARKS
		lb.	gm	mil/min	mm/min		
29-S	Life test.	.2	90	3.7	.09	Same wire.	Same as run 28-S.
30-S	Life test and test effects of machine modifica- tions.	.2	90	3.0	.08	Same wire.	Stiffening feed mechanism has improved wafer quality. Final feed calibration not complete at this time which may account for decreased cutting rates.
31-S 180	Life test; in- crease rate of rocking.					Same wire.	Calibration problem. Changed gear motor on rocking drive to 3.0 cycles/min.
32-S	Test effects of rocking 6 cycles/ min	.2	90	4.2	.1	Same wire.	No pressure change during run. Improved surface quality.
33-S	Test effects of changing blade- head speeds at ten minute intervals	.2	90	3.76	.094	Same wire.	Steady increase in cutting rates with speed increases and steady increase in machine noise 80-100 cycles/minute test range.
34-S	Test effects of slow bladehead half usual speed 10 cycles/minute	.2	90	2.2	.06	Same wire.	No significant improvement in wafer surface quality.

## APPENDIX E. SILICON SLICING SUMMARY (cont.)

RUN	PURPOSE	FEED FORCE/BLADE		AVERAGE CUTTING RATE		WIRE TYPE	REMARKS
		lb.	gm	mil/min	mm/min		
35-S	Determine optimum rocking speed	.2	90	3.2	.08	Same wire.	Small hydraulic lines on rocking slave changed to accommodate faster speeds which changed calibration leaving feed force unknown
36-S	Test effects of dry cutting	.2	90	3.76	.1	Same wire.	Dry cutting was aborted due to a loading condition. Run continued wet with good cutting rates. No damage to wires from cutting dry.
37-S	Life test .125 Ø impregnated wire	.088	40	N/A	N/A	Single impregnated 20 $\mu$ m diamond in copper plated wire .125 mm diameter	Good cutting rates were achieved at low feed force indicating that 20 $\mu$ m will cut well if concentration can be maintained. No hard data due to excess wire breakage.
38-S	Life test of .2mm Ø diamond impregnated wire	.15	68	2.1	.053	Single impregnated 45 $\mu$ m diamond in copper plated wire .2mm diameter	Good wafer quality.
39-S	Continuation of life test from run 38-C	.15	68			Same wire.	Aborted due to low cutting rate and wire breakage.

## APPENDIX E. SILICON SLICING SUMMARY (cont.)

RUN	PURPOSE	FEED		AVERAGE		WIRE TYPE	REMARKS
		FORCE/BLADE 1b.	gm	CUTTING RATE mil/min	mm/min		
40-S	Close .375mm, 15 mil spacing to produce 66 wafers per inch	.1	45			Single impregnated 20 $\mu$ m diamond in copper-plated wire .125mm diameter	Aborted due to loss of wafer and problems in support system.
41-S	Demonstrate close spacing .015 inch, .375mm spacing to produce 66 wafers per inch	.08		.6	.015	Single impregnated 45 $\mu$ m diamond in copper-plated wire .2mm diameter	Very low forces and low cutting rates used to slice 66 wafers, average wafer thickness 5 mil - .125mm.
182							
42-S	Close spacing same as run 41-S	N/A		N/A		Same wire.	Good data not available due to loss of wires. Cut completed in approx. 30 hrs., approx. 50% good 5 mil thin wafers.
43-S	Test CSI impregnated wire			N/A		0.005 copper coated stainless steel impregnated with #15 diamond (12-22 $\mu$ )	Run aborted after 0.600" due to poor cutting rates.
44-S	Test CSI impregnated wire			N/A		0.008 copper coated stainless steel 45 $\mu$ m diamond	Run aborted due to poor cutting rates.
45-S	Life test	0.15	67.5	1.13	0.03	0.008 nickel diamond plated wire used in runs 18-36	Good wafer quality.

## APPENDIX E. SILICON SLICING SUMMARY (cont.)

RUN	PURPOSE	FEED FORCE/BLADE		AVERAGE CUTTING RATE		WIRE TYPE	REMARKS
		lb.	gm	mil/min	mm/min		
46-S	Life test	0.15	67.5	1.04	0.025	0.008 nickel diamond plated wire used in runs 18-36	Good wafer quality. Poor support rollers.
47-S	Life test	0.2	90.0	2.5	0.06	0.008 nickel diamond plated wire used in runs 18-36	0.2 lb. required for good cutting rates.
48-S	Test new plated wire	N/A		N/A		5mil, 0.125mm stainless steel core, 45 $\mu$ m diamond nickel plated. 8.5mil total kerf.	Run aborted due to wire wander and wafer breakage.
49-S	Test plated wire	N/A		N/A		Same as 48-S	Failure due to wire breakage because of embrittlement during plating.
50-S	Test CSI impregnated wire	N/A		N/A		8mil, 0.2mm copper coated stainless steel wire.	Run aborted due to poor cutting rates in the middle of blade pack. Wires have uneven tension.
51-S	Life test	0.084	38	3.0	0.076	45 $\mu$ m diamond, Nickel plated, 5 mil, 0.125 mm tungsten core wire	Good wafer quality and cutting rates. 97% yield.
52-S	Life test	0.084	38	2.85	0.072	Same wire.	Good wafer quality and cutting rates. 97% yield.
53-S	Life test	0.084	38	2.36	0.060	Same wire.	Good wafer quality and cutting rates. 97% yield.

## APPENDIX E. SILICON SLICING SUMMARY (cont.)

RUN	PURPOSE	FEED		AVERAGE		WIRE TYPE	REMARKS
		FORCE/BLADE lb.	gm	CUTTING RATE mil/min	mm/min		
54-S	Life test	0.057	26	1.24	0.031	Same wire.	Run terminated after 1.3 in. cutting to leave workpiece intact. 90% yield.
55-S	Life test	0.070	32	1.70	0.043	Same wire.	Good wafer quality. 87% yield.
56-S	Life test	0.070	32	1.46	0.037	Same wire.	Good wafer quality. 85% yield.
57-S	Life test	0.084	38	2.26	0.057	Same wire.	Good wafer quality. 85% yield.
58-S	Life test and effect of shorter stroke --4.5"	0.070	32	1.31	0.033	Same wire.	Good wafer quality. 85% yield.
59-S	Life test and effect of change in stroke--6"	0.070	32	1.45	0.037	Same wire.	Good wafer quality. 85% yield.
60-S	Life test--stroke change midrun. To study effect on wafer surface.	0.056	25	1.13	0.029	Same wire.	Low feed forces used. Wafer characterization in progress.
61-S	Test CSI impreg- nated wire	N/A		N/A	Copper coated, stainless steel core, diamond impregnated wire.		Run aborted due to binding of wires in cuts.

## APPENDIX E. SILICON SLICING SUMMARY (cont.)

RUN	PURPOSE	FEED		AVERAGE		WIRE TYPE	REMARKS
		FORCE/BLADE lb.	gm	CUTTING RATE mil/min	mm/min		
62-S	Life test	0.074	34	1.64	0.042	45 $\mu\text{m}$ diamond, nickel plated, 80% yield. Good 5 mil, 0.125 mm tungsten core quality wafers.	
63-S	Life test	0.075	35	1.93	0.049	Same wire.	78% yield. Poor yield due to roller degradation.
64-S	Life test; new rollers in place	0.075	34	2.04	0.052	Same wire.	Dressing wires and new rollers increased yield to 97%.
65-S	Life test and roller degradation	0.075	34	1.66	0.042	Same wire.	Yield 83%. Rollers were used in run 64-S and show degradation.
66-S	Test new wires 30 $\mu\text{m}$	0.078	35	2.02	0.051	30 $\mu\text{m}$ diamond, nickel plated, 94% yield. Good 5 mil, 0.125 mm tungsten core wafer quality.	
67-S	Life test	0.078	35	1.81	0.046	Same wire.	89% yield. New rollers in place. Lower yield due to wire degradation.
68-S	Life test	0.078	35	1.70	0.043	Same wire	78% yield. Good wafer quality. Poor yield due to roller and wire degradation.

## APPENDIX E. SILICON SLICING SUMMARY (cont.)

RUN	PURPOSE	FEED FORCE/BLADE		AVERAGE CUTTING RATE		WIRE TYPE	REMARKS
		lb.	gm	mil/min	mm/min		
69-S	Life test	N/A	-	N/A	-	Same wire	Run aborted for machine modification
70-S	Slice 7.6 cm Ø workpiece	0.066	30	N/A	-	Same wire	Run aborted due to wafer breakage
71-S	Life test	0.066	30	1.90	0.048	Same wire	84% yield. Good quality wafers.
72-S	Test results of stiffening feed mechanism*	N/A	N/A	N/A	N/A	Same wire	Run was aborted at 1.6" due to excess breakage.
73-S	Test new rocking motion, new blades; stiffened feed* mechanism	0.080	36.6	0.877	-	0.005 tungsten core nickel plated 45 $\mu$ m diamond	Linear rocking motion broke down mid-run. Finished with crank motion, approximately 36% yield.
74-S	Rocking motion balanced and repaired.*	0.070	32.0	0.7936		Same as run 73-S.	Approximately 50% yield, good quality wafers.
75-S	Test new blades.*	N/A	N/A	N/A	N/A	0.005 hardened stainless steel core, nickel diamond plated 400-mesh	Approximately 30% yield; lost several wires due to wander and separation of plating from core. Poor wafer quality.

\* 7.6 cm diameter workpiece.

## APPENDIX E. SILICON SLICING SUMMARY (cont.)

RUN	PURPOSE	FEED		AVERAGE		WIRE TYPE	REMARKS	
		FORCE/BLADE 1b.	gm	CUTTING RATE mil/min	mm/min			
76-S	Test CSI impregnated blades	0.079	36	1.04	0.026	0.005 tungsten with 0.0007 copper coating, 30 $\mu$ m diamond	54% yield good wafer quality. 6.4 mil kerf. Severe diamond pullout.	
77-S	Life test, plated impregnated blades.	0.090	40.89	3.5	0.0889	Lastec 0.008 super, .0003 electroless nickel	94% yield, good quality wafers	
78-S	Life test plated impregnated blades	0.090	40.89	2.61	0.066	Lastec 0.008 super, 0.0003 electroless nickel	96% yield, very good quality wafers	
187	79-S	Life test plated impregnated blades	0.091	40.89	1.75	0.044	Same wire.	81% yield, good quality wafers